arXiv:1107.5060v2 [astro-ph.CO] 21 Aug 2011

Physical Properties of Galaxies from $z = 2 - 4$

Alice E. Shapley

Department of Physics and Astronomy, University of California, Los Angeles, CA 90095-1547; aes@astro.ucla.edu

Key Words Galaxy Evolution, Galaxy Formation, Galaxy Observations, Galaxy Structure, Interstellar Medium, Stellar Populations

Abstract The epoch of galaxy assembly from $2 \leq z \leq 4$ marks a critical stage during the evolution of today's galaxy population. During this period the star-formation activity in the Universe was at its peak level, and the structural patterns observed among galaxies in the local Universe were not yet in place. A variety of novel techniques have been employed over the past decade to assemble multiwavelength observations of galaxies during this important epoch. In this primarily observational review, I present a census of the methods used to find distant galaxies and the empirical constraints on their multiwavelength luminosities and colors. I then discuss what is known about the stellar content and past histories of star formation in high-redshift galaxies; their interstellar contents including dust, gas, and heavy elements; and their structural and dynamical properties. I conclude by considering some of the most pressing and open questions regarding the physics of high-redshift galaxies, which are to be addressed with future facilities.

CONTENTS

INTRODUCTION 3

HIGH-REDSHIFT GALAXY SELECTION TECHNIQUES 7

Historical Context 7

Rest-frame Ultra-Violet Selection 8

Rest-frame Optical/Infrared Selection 9

Submillimeter / Mid-Infrared Selection 11

Narrowband Selection 13

EMPIRICAL PROBES OF THE HIGH-REDSHIFT GALAXY POPULATION . . 13

Luminosity Functions 14

Color-Magnitude Diagrams 21

THE STAR-FORMATION RATES AND STELLAR CONTENT OF HIGH-REDSHIFT GALAXIES 23

Star-formation Rate Indicators 24

Evolution of the Star-formation Rate Density 27

Stellar Population Synthesis Models 29

The Diversity of High-Redshift Stellar Populations 36

Evolution of the Stellar Mass Density 38

$SFR - M_{star}$ Scaling Relations 41

THE INTERSTELLAR CONTENT OF HIGH-REDSHIFT GALAXIES 43

Dust Extinction 44

Dust Emission 51

Molecular Gas Content 55

Metal Content 60

STRUCTURAL AND DYNAMICAL PROPERTIES 66

Structural Properties 67

Dynamical Properties 74

CONCLUDING REMARKS 80

1 INTRODUCTION

Understanding the detailed formation and evolution of the galaxies we observe today remains one of the great challenges of modern cosmology. An exceedingly rich variety of galaxy properties exists in terms of luminosity, mass, color, structure, gas content, heavy-element enrichment, and environment, many of which, in turn, are strongly correlated with each other. As reviewed by Blanton & Moustakas (2009), based on the latest generation of wide-field surveys of the local Universe, astronomers have constructed an exquisitely detailed and statistically robust description of the galaxy population *today*. These results are crucial in terms of providing a boundary condition, or endpoint, for our description of the formation and evolution of galaxies. Ultimately, we strive to tell that story from beginning to end. To do so, we must assemble additional observations and theories.

Multiple complementary approaches can be used to construct the history of galaxy formation. These include ab initio analytic models or numerical simulations; examinations of the fossil record contained in the ages, metallicities, and phase-space distributions of stars in nearby galaxies; and direct observations of distant galaxies, for which the cosmologically significant lookback time allows a probe of the Universe at an earlier time. In order to test theoretical models of galaxy formation at every time step, observations of galaxies over a wide range of lookback times are required. Furthermore, a robust translation must be performed between the observer's empirical quantities of luminosity, color, and velocity dispersion, and the theorist's physical quantities of stellar and dynamical mass, current star-formation rate and past star-formation history.

In the comparison between observations and theoretical models of galaxy evolution, an important recent development is the establishment of a precision cosmo-

logical framework. Observations of the cosmic microwave background radiation, large-scale structure, Type Ia supernova, the abundance of galaxy clusters, and the expansion rate of the Universe, all appear to be well described by a cosmological model in which the Universe is spatially flat, with the dominant component of the mass-energy density in the form of dark energy, and the remainder consisting mostly of cold dark matter with a small fraction of baryons. The initial spectrum of density fluctuations in this model is adiabatic, Gaussian, and nearly scale invariant. The most recent determination of cosmological parameters from the *Wilkinson Microwave Anisotropy Probe* (WMAP) (Spergel et al. 2003) is presented in Komatsu et al. (2011), and highlights the fact that most parameters are determined with better than $5-10\%$ precision.

Constraining the background cosmological parameters is a crucial part of understanding galaxy formation not only for converting apparent quantities such as flux and angular size, respectively, into intrinsic ones such as luminosity, star-formation rate, stellar mass, and physical size. Cosmological parameters are also required for precise theoretical calculations whose predictions can be compared with observations, because, according to leading models, the underlying set of cosmological parameters determine how tiny primordial dark matter density fluctuations evolve under the influence of gravity into the large-scale spatial distribution of matter in the current Universe. In this framework, the collapsed perturbations of dark matter – dark matter halos – serve as the very sites of galaxy formation. Based on recent determinations of cosmological parameters, massive numerical simulations of the growth of dark matter structure have been performed (Boylan-Kolchin et al. 2009, Springel et al. 2005). In order to compare more directly with observations of galaxy formation, models

(either numerical hydrodynamic or semi-analytic) describing the baryonic processes of gas cooling, star formation, and metal enrichment are also required, and these, too, are advancing with increased spatial resolution and complexity (e.g., Ceverino, Dekel & Bournaud 2010; Somerville et al. 2008).

In order to probe the origin of the global patterns observed in the current galaxy population, we must look back to a time before these trends were already in place. Furthermore, the old stellar populations of nearby early-type galaxies in dense environments suggest that the bulk of their stars formed at $z \geq 2$ (Thomas et al. 2005). Therefore, catching the formation of spheroids "in the act" requires observations at such early times. Given the strong correlation between the properties of the spheroidal components of galaxies and their central black holes, the epoch when the spheroids are forming holds special interest for explaining this connection. As described in more detail during the course of this review, the redshift range, $2 \leq z \leq 4$, corresponding to a lookback time of $\sim 10 - 12$ Gyr, is ideal for directly observing the progenitors of today's fairly luminous spheroidal and disk galaxies while in the very process of attaining the properties that come to define them over the next 10 Gyr up to the present day. Towards the end of this redshift range, the overall level of "activity" in the Universe – both in terms of star formation and black hole accretion - was at its peak value. In contrast to what is observed in the present-day Universe, a significant fraction of the most massive galaxies still sustained active star formation. Furthermore, the Hubble Sequence of disk and elliptical galaxies was not yet in place, and the abundance of rich clusters was vanishingly small. The early Universe looked drastically different from its current state. Therefore, studying this epoch can yield important clues about the evolution of galaxies.

Within the past decade, there has been incredible progress in the study of galaxies in this important redshift range of galaxy assembly. A variety of novel techniques have been used to identify distant galaxies, and the sample of galaxies with spectroscopic redshifts at $2 \leq z \leq 4$ now numbers well into the thousands. Although we are far from approaching the overwhelming statistical power of the giant local redshift surveys such as the Sloan Digital Sky Survey (SDSS; Abazajian et al. 2009, Blanton & Moustakas 2009) and 2dF Galaxy Redshift Survey (2dFGRS; Colless et al. 2001), in terms of number of galaxies surveyed spectroscopically, volume probed, and data quality, key features of the galaxy population at these early times are emerging. The physical properties inferred for distant galaxies have provided important inputs and daunting challenges to state of the art theoretical models of galaxy formation. As we look forward to the next generation of instrumentation on current and future large ground-based telescopes, as well as the James Webb Space Telescope (*JWST*) in space, and ever more sophisticated galaxy formation models, it is worth reviewing what is known about the physical properties of high-redshift galaxies at $2 \leq z \leq 4$.

This primarily observational review is constructed as follows. In Section 2, we provide an overview of the many different techniques that have recently been employed for identifying high-redshift galaxies. We continue in Section 3 by reviewing the global multiwavelength distributions in luminosity and color for galaxies in this redshift range. In Section 4, we delve into the techniques used to transform empirical quantities such as luminosity and color into physical ones relating to galaxy stellar populations. In particular, we focus here on stellar content and the history of star-formation activity, as well as the relationship between these quantities. Sections 5 and 6 in turn consider what is known about the inter-

stellar medium (ISM) of distant galaxies – where the interstellar contents include gas, dust, and metals – and their structural properties and dynamics. Although many gaps remain in our knowledge of these fundamental physical properties, as described in Section 7, future facilities and instrumentation will guide us in our quest to assemble a comprehensive picture of the galaxy population during this distant yet intriguing epoch in the history of galaxy formation.

2 HIGH-REDSHIFT GALAXY SELECTION TECHNIQUES

In this section, we provide a brief historical context for the recent dramatic developments in the study of high-redshift galaxies, as well as reviewing several of the most common and complementary techniques for identifying distant objects.

2.1 Historical Context

Over the past 10–15 years, the study of high-redshift galaxies has truly exploded, with an increasing number of surveys for systems at lookback times of order 10 Gyr. The number of galaxies with spectroscopic redshifts at $z > 2$ is now well into the thousands, and the number whose multiwavelength photometric properties identify them as such is more than an order of magnitude larger. Due to the difficulties of obtaining optical and near-infrared (near-IR) spectra of faint objects, photometric redshifts have played an increasingly common role in describing the properties of distant galaxies – bringing with them both the advantages of much larger samples, and also the drawbacks of larger uncertainties in derived galaxy properties. Also, with some exceptions like the VIRMOS VLT Deep Survey (VVDS; Le Fèvre et al. 2005), which targets galaxies for spectroscopy down to a given optical magnitude limit, these new results for the most part utilize several

novel techniques for efficiently identifying distant galaxies with minimal contamination by systems at lower redshift. Although effective at isolating high-redshift galaxies, all of these selection methods suffer from incompleteness with respect to a sample defined in terms of physical quantities such as stellar or dynamical mass, or star-formation rate. In this section, we describe the landscape of galaxy surveys that have contributed thus far to our picture of the high-redshift galaxy population.

2.2 Rest-frame Ultra-Violet Selection

One method for selecting distant galaxies is based on their rest-frame UV colors. This method was first applied at $z \sim 3$, and specifically exploits the combined effects of neutral hydrogen opacity within a star-forming galaxy and along the line of sight through the intergalactic medium (IGM). Accordingly, $z \sim 3$ star-forming galaxies with moderate amounts of dust extinction (less than a factor of 100 in the rest-frame UV) will have distinctive colors in a $UG\mathcal{R}$ filter system, with fairly flat $G-\mathcal{R}$ and extremely red $U-G$ colors. The "Lyman Break Technique" has been used to identify thousands of galaxies (so-called Lyman Break Galaxies, or LBGs) at $z \sim 3$ (Steidel et al. 2003, 1996), and, using different filter sets, at $z \sim 4$ and 5 (Ouchi et al. 2004). At $z \sim 6$ and beyond, even redder sets of three filters have been used to identify star-forming galaxies (Bouwens et al. 2007, 2010, Oesch et al. 2010). In these latter cases, however, the main spectral break between the bluest and middle filter arises due to hydrogen Lyα opacity in the IGM, as opposed to opacity at the Lyman limit. Rest-frame UV selection using the initial set of $UG\mathcal{R}$ filters has also been extended down to lower redshift (Adelberger et al. 2004, Steidel et al. 2004), where galaxies at $1.4 \leq z \leq 2.5$ are

isolated due to a *lack* of significant spectral break. Their fairly flat rest-frame UV colors, modulated at $2 \leq z \leq 2.5$ only by Lyα forest line blanketing in the U-band, also prove distinctive. Figure 1, from Steidel et al. (2004), provides an illustration of the rest-frame UV selection criteria in $UG\mathcal{R}$ color space, tuned to find galaxies at $1.5 \leq z \leq 3.5$.

Given the criterion of detection in the rest-frame UV, the techniques described above necessarily select galaxies with ongoing star formation and are not sensitive to passive galaxies. Furthermore, the windows in color-color selection space exclude galaxies whose rest-frame UV continuum shape is indicative of significant dust reddening. Ground-based rest-frame UV surveys are also typically characterized by a rest-frame UV (observed optical) flux limit. Detection in rest-frame UV (observed optical) bands results in objects well suited to optical spectroscopic follow-up. Accordingly, successful spectroscopic follow-up of high-redshift galaxies has been weighted towards rest-frame-UV-selected samples, probing galaxies with active ongoing star formation.

2.3 Rest-frame Optical/Infrared Selection

Other techniques are tuned to select galaxies on the basis of their rest-frame optical colors and are based on a detection at observed near- or mid-infrared (mid-IR) wavelengths. For these techniques, the relevant spectral break is either the Balmer break at ~ 3650Å, which arises when the integrated stellar spectrum from a galaxy at these wavelengths indicates the overall spectral shape of A-stars, or else the 4000 Å break, which reflects the absorption from ionized metals in the atmospheres of late-type stars. Although both breaks are indications of maturity in stellar populations, they are by no means equivalent in terms of the underlying

stellar populations that cause them. The Balmer break appears in stellar populations featuring ongoing star-formation over sustained timescales (> 100 Myr), or post-starburst populations $0.3 - 1$ Gyr since the cessation of star formation. The 4000 Å break is strongest in passive stellar populations in which the current level of star formation has been negligible for more than 1 Gyr. Isolating $z \geq 2$ galaxies on the basis of their rest-frame optical breaks requires deep, near-IR photometry. As described in Franx et al. (2003) and van Dokkum et al. (2003), a threshold of $J_{Vega} - K_{Vega} > 2.3$ is effective at identifying objects that dominate the high-mass regime of the $z > 2$ stellar mass function (Kriek et al. 2008b). Figure 2 (left, from Franx et al. 2003) demonstrates the sensitivity of the $J_{Vega} - K_{Vega}$ color to mature stellar populations at $z > 2$. These Distant Red Galaxies (DRGs) in fact typically have significant dust obscuration ($A_V > 1$) and active star-formation rates ($\geq 100 M_{\odot}$ yr^{-1}) (Papovich et al. 2006), although some show little evidence for ongoing star formation (van Dokkum et al. 2008). Regardless, the red rest-frame UV to optical colors of DRGs down to current near-IR limits indicate typical stellar masses in excess of $10^{11} M_{\odot}$. The main limitation of such studies is the limited amount of spectroscopic follow up, due to the optical faintness (typically $R \geq 25$) of DRGs and the difficulty of obtaining large samples of near-IR spectra (but see, e.g., Kriek et al. 2008b).

Another common technique for isolating galaxies at $1.4 \leq z \leq 2.5$ consists of the so-called "BzK" method (Daddi et al. 2004). As shown in Figure 2 (right), BzK galaxies are identified in K-selected samples of galaxies on the basis of their colors in the $z - K$ versus $B - z$ plane. Galaxies with fairly blue $B - z$ colors and red $z - K$ colors are selected as star-forming $z \sim 2$ systems ("$sBzK$"), due to the presence of a Balmer break. At the same time, quiescent systems ("$pBzK$") at the

same redshift are identified on the basis of red colors in both $B-z$ and $z-K$. Although fairly general in terms of selecting both star-forming and quiescent galaxies, this method misses the youngest star-forming galaxies at $z \sim 2$, which lack a significant Balmer or 4000 Å break (Reddy et al. 2005). While the star-forming $sBzK$ galaxies have rest-frame UV colors that are redder on average than the corresponding UV-selected galaxies at $z \sim 2$, there is significant overlap between these two photometric selection technique down to a fixed K-band magnitude limit – much more than between the UV-selected and DRG samples, which overlap at only the 10% level (Reddy et al. 2005). Other surveys tuned to find high-redshift galaxies based on their rest-frame optical or near-IR properties include the Gemini Deep Deep Survey (GDDS; Abraham et al. 2004) and the Galaxy Mass Assembly ultra-deep Spectroscopic Survey (GMASS; Cimatti et al. 2008).

2.4 Submillimeter / Mid-Infrared Selection

The overall increase in the level of star-formation activity in the Universe at earlier times results in an increased abundance of extreme, bolometrically ultra-luminous systems. These systems emit the bulk of their radiation at rest-frame far-IR wavelengths, because of copious amounts of dust obscuring their star-formation and AGN activity. Systems with bolometric luminosities greater than $L = 10^{12} L_{\odot}$ are commonly referred to as Ultra-luminous Infrared Galaxies (ULIRGs). Submillimeter and mid-IR instrumentation sensitive to cool and hot dust, respectively, have enabled the identification of these extreme high-redshift ULIRGs on the basis of their reprocessed emission, while multiwavelength imaging and spectroscopic follow-up has elucidated the range of their properties. The Submillimetre Common-user Bolometer Array (SCUBA) has been used to identify

bolometrically-luminous submillimeter galaxies (SMGs; Smail, Ivison & Blain 1997), and the largest set of spectroscopically-confirmed such objects was obtained by following up the subset of sources with both $F_{850\mu m} \geq 5$ mJy and *Very Large Array* (VLA) 1.4 GHz fluxes greater than $F_{1.4\ \mathrm{GHz}} \sim 30\mu$Jy (Chapman et al. 2003, 2005). The radio fluxes were used to obtain the precise (1"$-$2") positions required for spectroscopic observations, which were not achievable with the coarse (15") SCUBA beam. These luminous SMGs with radio counterparts have a median redshift of $z = 2.2$, although, given that the requirement of a radio flux detection recovers $\sim$ 50% of the $F_{850\mu m} \geq 5$ mJy population, their redshift distribution may not be fully representative of the luminous SMG population as a whole.

The Multiband Imaging Photometer for Spitzer (MIPS) onboard the *Spitzer Space Telescope* has been used to identify high-redshift dusty sources on the basis of their brightness at 24μm and faintness at optical wavelengths. Yan et al. (2007) and Dey et al. (2008) present such samples, identified using slightly different criteria, but both based on similar criteria of detection at 24μm, with a large ratio of mid-IR to optical flux. The majority of these objects are at $1.5 \leq z \leq 3$, with comparable space densities ($\sim 10^{-5}$ Mpc^{-3}) to those of SMGs. On the other hand, the 24μm-selected sources are characterized by warmer dust temperatures and a higher frequency of AGN signatures at mid-IR wavelengths than SMGs selected at longer wavelengths (see Section 5.2). Quantifying the relative contributions of star-formation and AGN activity in powering the extreme luminosities of both mid-IR and submillimeter-selected ULIRGs will enable us to isolate the underlying nature of these sources. Another key goal consists of constraining the relative importance of major mergers and smooth mass accretion as triggers for the ULIRG phase.

2.5 Narrowband Selection

In contrast to the identification of high-redshift objects on the basis of broadband spectral shape, the use of a narrowband filter tuned to the redshifted wavelength of a specific emission line is effective at isolating objects with large emission-line equivalent widths. The most common emission line for which narrowband filters are designed is hydrogen Lyα. As shown in Figure 3 (from Gronwall et al. 2007), based on images through both the narrowband filter and a broadband filter close in wavelength, objects with red broadband minus narrowband colors are flagged as Lyα line emitters (LAEs). More than 2000 LAEs have been identified with ground-based facilities at $2 \leq z \leq 8$ (e.g., Cowie & Hu 1998, Gronwall et al. 2007, Nilsson et al. 2011, Ouchi et al. 2008, Rhoads et al. 2000). The star-forming LAEs tend to be significantly fainter on average than the UV-continuum-selected objects described in Section 2.2, and therefore offer a probe of the faint end of the luminosity function. On the other hand, the faint nature of these objects leads to a challenge in assembling high signal-to-noise (S/N) multiwavelength imaging and spectra for individual LAEs (with information other than a measurement of Lyα emission), hindering the determination of their relationship to other galaxy populations at similar redshifts.

3 EMPIRICAL PROBES OF THE HIGH-REDSHIFT GALAXY POPULATION

Before reviewing what is known about the stellar and interstellar content of distant galaxies, we must consider the empirical measurements from which these physical properties are inferred. The observables here are distributions in luminosity and color, which offer some of the most basic and fundamental probes

of a galaxy population. In addition to traditional optical photometry tracing the rest-frame ultraviolet, our view of the global photometric properties of galaxies at $z \geq 2$ is now based on deep, near-IR surveys from the ground using wide-field imagers on 4-meter-class telescopes (e.g., KPNO/NEWFIRM, UKIRT/WFCAM, CTIO/ISPI, Palomar/WIRC) and narrow- and wide-field imagers on $8-10$-meter class telescopes (e.g., Keck/NIRC, VLT/ISAAC, Subaru/MOIRCS, VLT/HAWK-I), and mid- and far-IR surveys using *Spitzer* and *Herschel* in space. Multiwavelength observations have, therefore, granted us a window into the luminosity and color distributions of high-redshift galaxies spanning from the rest-frame UV through the rest-frame far-IR.

3.1 Luminosity Functions

The galaxy luminosity function offers constraints on the overall abundance of objects, as well as the integrated luminosity density at a given wavelength. As such, the luminosity function provides a key observational baseline for each redshift at which it is measured.

3.1.1 REST-FRAME UV LUMINOSITY FUNCTIONS Some of the first luminosity functions to be measured for high-redshift galaxies were based on optical observations of rest-frame UV-selected $z \sim 3$ and $z \sim 4$ LBGs (Steidel et al. 1999), probing rest-frame wavelengths of $\lambda \sim 1700$Å. This work highlighted the importance of dust extinction for converting the rest-frame UV luminosities of star-forming galaxies into unobscured values, in order to obtain dust-corrected star-formation rates. We will return to this point in Sections 4 and 5.1, when we consider the star-formation rates and dust content of high-redshift galaxies. Rest-frame UV luminosity functions for large samples of distant galaxies have now

been estimated by several different groups, from $z \sim 2$ all the way out to $z \sim 8$ (Bouwens et al. 2010). As in the local Universe, the galaxy luminosity function at high redshift is typically parameterized using the Schechter form of a power law multiplying an exponential function (Schechter 1976). The associated free parameters to constrain are the characteristic luminosity, L^* (or M^* in the space of absolute magnitude), the faint-end slope, α, and the overall normalization, Φ^*.

At $z \sim 2 - 3$, the work of Reddy et al. (2008) and Reddy & Steidel (2009) is based on the largest set of spectroscopic redshifts in the literature, and, including a consideration of the systematic variation of dust reddening with UV luminosity, is accordingly the most robust. Specifically, Reddy & Steidel (2009) utilizes > 2000 spectroscopic redshifts, and $\sim 31,000$ $z \sim 2 - 3$ photometric candidates in 31 independent fields over 0.9 deg^2. In this paper, the standard LBG selection limit of $\mathcal{R} = 25.5$ was extended to fainter magnitudes ($\sim 0.1L^*$) to obtain tighter constraints on the faint-end slope, α. Recent luminosity function determinations at $z \sim 4$ include those by Bouwens et al. (2007), using 4671 B-dropout galaxies selected over 580 arcmin^2 with deep *Hubble Space Telescope* (*HST*) Advanced Camera for Surveys (ACS) imaging, down to $M_{UV,\mathrm{AB}} = -16$, and by van der Burg, Hildebrandt & Erben (2010), based on $\sim 36,000$ $g-$dropout galaxies selected in the CFHT Legacy Survey in four independent 1 deg^2 fields down to $M_{UV,\mathrm{AB}} = -18.7$. Both of these $z \sim 4$ surveys, however, are solely based on photometric selection, without spectroscopic confirmation. Figure 4 reviews recent determinations of the rest-frame UV luminosity function at $2 \leq z \leq 4$.

The rest-frame UV luminosity functions of star-forming galaxies at $z \sim 2 - 4$ are characterized by steep faint-end slopes ($\alpha \sim -1.6 - -1.7$) and characteristic luminosities of $M^*_{\mathrm{AB}} = -21$. These steep faint-end slopes are in contrast to

the flatter one ($\alpha = -1.22$) determined from the local far-UV (FUV) luminosity function using *Galaxy Evolution Explorer* (GALEX) data (Wyder et al. 2005). Also, the characteristic luminosities at $z \sim 2-4$ are roughly three magnitudes brighter than those determined from the local GALEX FUV luminosity function. Reddy & Steidel (2009) review other recent luminosity function determinations at $z \sim 2-3$, highlighting some of the discrepancies in the literature, including those determinations with significantly flatter faint-end slopes (Gabasch et al. 2004, Sawicki & Thompson 2006), and/or larger counts at the brightest luminosities (Paltani et al. 2007). To address some of these differences, Reddy & Steidel (2009) point out the pitfalls associated with attempting to measure the luminosity function over small areas (< 50 arcmin^2), making incorrect assumptions about the nature of the intrinsic mean and dispersion in colors of the faintest galaxies, and insufficiently accounting for contamination by low-redshift interlopers. Again, we emphasize the importance of spectroscopy for understanding the redshift selection function of the objects for which the luminosity function is being constructed, and the proper characterization of systematic effects modulating the volume probed by a given galaxy survey.

3.1.2 REST-FRAME OPTICAL AND NEAR-INFRARED LUMINOSITY FUNCTIONS While the rest-frame UV luminosity of distant galaxies reflects the emission from massive stars, longer wavelengths probe different aspects of galaxy stellar populations and dust content. Specifically, the rest-frame optical luminosity function is more reflective of older stars, although the extent to which emission at these wavelengths reflects the integrated stellar mass depends in detail on the star-formation history of the galaxy (Shapley et al. 2001, 2005). The rest-frame optical (V-band) luminosity function was first determined

at $z \sim 3$ by Shapley et al. (2001), based on the LBG $\mathcal{R}$-band luminosity function and the distribution of $\mathcal{R} - K_s$ colors for a sample of 118 LBGs, 81 of which had spectroscopic redshifts. These measurements yielded a steep faint-end slope of $\alpha = -1.85$, which is significantly different from the local determinations with $\alpha \sim -1$, and a characteristic luminosity of $M_V^* = -22.98$, which is 1.5 magnitudes brighter than the local value (Blanton et al. 2003).

Most recently, based on a much larger set of ~ 1000 K-band measurements at $2 \leq z \leq 3.5$, selected over a total area of 378 arcmin^2 from multiple near-IR surveys of varying depths, Marchesini et al. (2007) constructed B, V, and R-band luminosity functions. Using mainly photometric redshifts, Marchesini et al. (2007) find that the faint-end slopes of these luminosity functions are, within the errors, consistent with the fairly shallow slope determined for the local optical luminosity function, whereas the characteristic magnitudes are significantly brighter ($\gtrsim 1$ magnitude). In contrast to Shapley et al. (2001), Marchesini et al. (2007) find values of α ranging from $-1.0 - -1.4$. However, it is worth pointing out that, in the region of overlap, the Marchesini et al. rest-frame V-band luminosity function for "blue" ($J - K \leq 2.3$) galaxies and the Shapley et al. rest-frame V-band LBG luminosity function are entirely consistent. Both total and "blue" V-band luminosity functions from Marchesini et al. (2007) are shown along with the luminosity function from Shapley et al. (2001) in Figure 5, reproduced from Marchesini et al. (2007). Potential limitations of the Marchesini et al. (2007) analysis are in the small fraction of spectroscopic redshifts ($\sim 4\%$) and corresponding reliance on photometric redshifts, and the small area over which the photometry is deep enough to robustly probe the faint end (~ 25 arcmin^2). With ultra-deep K-band [$K_{limit} \sim 23$(Vega)] surveys over significantly larger

areas ($\sim$ 1000s of arcmin^2), such as the UKIDSS Ultra-Deep Survey (UDS), the much-needed robust constraints on the faint-end slope of the rest-frame optical luminosity function will be within reach. Extensive spectroscopic follow-up is also necessary to avoid some of the biases related to photometric redshifts that are described in Reddy et al. (2008) and Reddy & Steidel (2009).

In principle, the rest-frame near-IR luminosity is even more closely tied to stellar mass than the rest-frame optical (despite some of the uncertainties we will discuss in Section 4.3). The largest study to date of the evolving rest-frame K-band luminosity function is based on the UKIDSS UDS First Data release, presented by Cirasuolo et al. (2010), updating their earlier work (Cirasuolo et al. 2007). This study features a $K+z$-band-selected catalog of $\sim 50,000$ galaxies over 0.7 deg^2 ($\sim 10,000$ of which are at $z > 1.5$), which is complete down to $K = 23$ (AB). Given the location of the UKIDSS UDS in the Subaru/XMM-Newton Deep Survey field, this survey also benefits from extensive multiwavelength coverage spanning from FUV (GALEX) to mid-IR (*Spitzer*) wavelengths. Cirasuolo et al. (2010) estimate photometric redshifts and rest-frame K-band luminosities based on spectral-energy distribution (SED) fits to the multiwavelength photometry of their sources. The depth of the Cirasuolo et al. (2010) sample is not sufficient to trace the faint-end slope and its evolution past $z \sim 1$, so the evolution to high redshift is simply quantified in terms of the luminosity function normalization and characteristic luminosity. From $z \sim 0$ to $z \sim 2$, Cirasuolo et al. (2010) report a brightening in M^* by ~ 1 magnitude and a decrease by a factor of ~ 3.5 in normalization, Φ^*. Again, deeper near-IR photometry and extensive spectroscopic follow-up for near-IR-selected catalogs will be required to probe the full evolution of the rest-frame near-IR luminosity function at high redshift.

3.1.3 REST-FRAME MID-INFRARED AND BOLOMETRIC LUMINOSITY FUNCTIONS At even longer rest-frame wavelengths, we begin to probe the direct emission from dust. Building on the work of earlier missions such as the *Infrared Astronomical Satellite* (IRAS) and the *Infrared Space Observatory* (ISO), which traced the evolution of infrared-luminous (IR-luminous) sources out to $z \sim 1$, *Spitzer* has played a crucial role in tracing the global dust emission properties for large samples of $z > 1$ star-forming galaxies. The most widely-used tool in this endeavor is the 24μm channel of the MIPS instrument, which probes a rest-frame wavelength of $\lambda \sim 8\mu$m at $z \sim 2$, sensitive to the emission from polycyclic aromatic hydrocarbon (PAH) emission. Ground-based submillimeter observatories such as SCUBA have also played a key role in understanding the evolution of most IR-luminous sources, but for much smaller galaxy samples. Overall, out to $z \sim 1$, the evolution of the mid-IR and total IR luminosity function is characterized by both significant luminosity and density evolution (Le Floc'h et al. 2005). IR-luminous galaxies were more numerous in the past, and the IR luminosity density at $z \sim 1$ is dominated by luminous infrared galaxies (LIRGs), with $L_{IR} > 10^{11} L_{\odot}$.

Recent work by Pérez-González et al. (2005), Caputi et al. (2007), and Rodighiero et al. (2010) have characterized the luminosity functions of MIPS 24μm-selected galaxies at $z > 1$. We focus here on the results of Caputi et al. (2007) and Rodighiero et al. (2010), who used more conservative criteria for excluding AGNs from their samples, and adopted conversions between rest-frame 8μm and total IR luminosities that are most consistent with observed constraints (and agree well with each other). These studies select galaxies down to a flux limit of $S(24\mu\text{m}) = 80\mu$Jy in the 0.08 deg^2 of the Great Observatories Origins Deep Survey (GOODS) North and South fields,

while Rodighiero et al. (2010) additionally include a shallower catalog down to a limit of $S(24\mu\text{m}) = 400\mu\text{Jy}$ in the 0.85 deg^2 of the VVDS-SWIRE area. As shown in Figure 6, Caputi et al. (2007) determine mid- and total IR luminosity functions at $z \sim 1$ and $z \sim 2$, while Rodighiero et al. (2010) construct the corresponding luminosity functions in nine redshift bins from $z \sim 0$ to $z \sim 2.5$.

Both of these works echo the previously determined increase of an order of magnitude in the bolometric IR luminosity density from $z \sim 0$ to $z \sim 1$, and the heightened abundance of both LIRGs and ULIRGs. Rodighiero et al. (2010) find that the IR luminosity density is roughly constant from $z \sim 1$ to $z \sim 2.5$, while Caputi et al. (2007) find evidence for a slight decline. For both of these studies, it is worth pointing out that their completeness limits at $z \sim 2$ in 8μm luminosity translate into bolometric IR luminosities of $\sim 10^{12} L_{\odot}$. Therefore, these luminosity functions only directly probe the ULIRG regime. Furthermore, neither study can place constraints on the faint-end slope of the luminosity function, and instead adopt a fixed parameter of $\alpha = -1.2$ based on local observations. Using indirect estimates of the rest-frame 8μm and bolometric IR luminosity functions at $z \sim 2$, inferred from the extinction-corrected luminosities of UV-selected star-forming galaxies, Reddy et al. (2008) extend the determination of the IR luminosity function into the LIRG regime, and suggest that a significantly steeper faint-end slope may be required. Accordingly, ULIRGs make a sub-dominant ($\sim 25\%$) contribution to the far-IR luminosity density at $z \sim 2$. Future direct observations of this fainter IR regime with *Herschel*, and even more sensitive planned facilities such as the *Single Aperture Far-Infrared* (SAFIR) observatory, will be crucial in untangling the evolution of the IR luminosity density and the history of obscured star formation in the Universe.

3.2 Color-Magnitude Diagrams

A standard tool for describing the galaxy population in the local Universe is the optical "color-magnitude" diagram, in which rest-frame optical colors are plotted as a function of rest-frame optical absolute magnitude. The added dimension of color proves very useful for separating different types of galaxies. Indeed, while the division of the galaxy population into different types (e.g., late-type spirals and irregulars, and early-type ellipticals and lenticulars), and the correlation between galaxy structure and color have been well-known for a long time, the advent of large spectroscopic surveys such as SDSS have allowed for a quantitative description of the bimodality in galaxy photometric properties, based on incredibly robust statistics. Both Strateva et al. (2001) and Baldry et al. (2004) have presented striking evidence that local galaxies occupy a bimodal distribution in the space of $u - r$ colors, and that the fraction of bluer galaxies increases at fainter optical absolute magnitudes. Galaxies occupying the so-called "red-sequence" part of the bimodal distribution primarily consist of morphologically early-type galaxies and follow a very tight relationship between color and magnitude in which more luminous galaxies have redder colors. At the same time, objects residing in the "blue cloud" are predominantly late-type galaxies, and show a looser, though still systematic, variation of color and luminosity in the same sense. The bimodal distribution of galaxy colors as a function of luminosity, along with the correlation of color and other galaxy properties, suggests two distinct types of formation histories. It is therefore of critical interest to trace the galaxy color-magnitude diagram to earlier times, and to determine how far back the bimodality in the galaxy distribution persists.

Based on the COMBO-17 survey, Bell et al. (2004) demonstrate that bimodal-

ity is detected in the color-magnitude diagram out to $z \sim 1$. Now, using the results from recent near- and mid-IR-selected surveys, other groups have considered the question of galaxy bimodality at even higher redshifts. As shown in Figure 7, with a sample of 1021 *Spitzer*/IRAC 4.5μm-selected objects from the GMASS survey with optical through mid-IR SEDs, 190 of which have spectroscopic redshifts above $z = 1.4$, Cassata et al. (2008) demonstrate that a bimodality in galaxy rest-frame $U - B$ colors persists up to $z = 2$. Brammer et al. (2009) uses $\sim 25,000$ objects with $K < 22.8$ (AB) selected from the NEWFIRM Medium-Band Survey (NMBS), and detect a bimodality in rest-frame $U - V$ colors out to $z \sim 2.5$. The increasing importance of obscured star formation at higher redshifts tends to cause contamination of the red sequence by dusty, star-forming galaxies, and Brammer et al. (2009) show a much cleaner division in dust-corrected colors, or when considering only galaxies whose mid-IR flux limits of $S(24\mu\mathrm{m}) < 20\mu\mathrm{Jy}$ indicate the presence of little or no dust. Based on a smaller sample of 28 K-selected galaxies with spectroscopic redshifts $2 < z < 3$, Kriek et al. (2008a) detect a red sequence in rest-frame $U - B$ colors, quantified in terms of a significant overdensity of galaxies within a narrow bin of red rest-frame $U - B$ color. These high-redshift red-sequence galaxies are characterized by little or no ongoing star formation, with strong Balmer breaks indicating that they are likely in a post-starburst phase. While suggestive of the existence of a red sequence, the sample in Kriek et al. (2008a) is too small to test for the presence of bimodality in galaxy colors.

Both Kriek et al. (2008a) and Cassata et al. (2008) stress the need for precise (and ideally spectroscopic) redshift information when attempting to detect features in the galaxy rest-frame color distribution such as bimodality or the presence

of a red sequence. While they lack actual spectroscopic confirmation, galaxies in the NMBS presented by Brammer et al. (2009) have extremely accurate photometric redshifts, with $\Delta z/(1+z) < 0.02$ at $z > 1.7$. Photometric redshifts typical of other studies, with errors of $\Delta z/(1+z) \sim 0.1$ or worse, will lead to random and systematic errors in inferred rest-frame UV and optical colors that will wash out these trends when a single color is considered. However, using only photometric redshifts but considering *two* rest-frame colors together, Williams et al. (2009) discern a bimodal behavior in the space of rest-frame $U - V$ versus $V - J$ color-color space out to $z \sim 2.5$. The rest-frame colors for this study are inferred from optical, near-IR, and *Spitzer*/IRAC photometry drawn from the UKIDSS UDS, the Subaru-*XMM* Deep Survey (SXDS), and the *Spitzer* Wide-Area Infrared Extragalactic Survey (SWIRE), and effectively separate quiescent, non-star-forming galaxies from their actively star-forming counterparts. The evolving locations in color space and very existence of the "red sequence" and "blue cloud" provide important constraints on models of galaxy formation.

4 THE STAR-FORMATION RATES AND STELLAR CONTENT OF HIGH-REDSHIFT GALAXIES

While the luminosities and colors of galaxies represent basic and fundamental observables, we seek to translate these measurements into physical quantities. Specifically, the SEDs of galaxies are commonly interpreted in terms of the current rate of star formation and its past history, as well as the integrated stellar content of galaxies. In this section, we summarize both the simple methods used to infer star-formation rates from specific luminosities, as well as the techniques used to model the stellar populations of high-redshift galaxies based on mul-

tiwavelength SEDs. Along the way, we highlight the results of applying these methods to determine the global history of star formation, the build-up of stellar mass density, and the relationship between star-formation rate and stellar mass in distant galaxies.

4.1 Star-formation Rate Indicators

As reviewed by Kennicutt (1998), there are several diagnostics of star-formation activity in external galaxies. In the study of distant galaxies at $z > 2$, integrated light measurements tracing young stellar populations are used to infer the rate at which stars are being produced. These measurements include rest-frame UV and IR luminosities, hydrogen recombination emission-line luminosities, and stacked X-ray and radio luminosities (due to the sensitivity limits of current X-ray and radio facilities, $z > 2$ star-forming galaxies are typically only detected in a statistical sense). In general, these diagnostics are only sensitive to the presence of massive stars. Therefore, an estimate of the total star-formation rate requires the assumption of a particular form for the stellar initial mass function (IMF), which is then used to extrapolate down to the low stellar masses that dominate the integrated stellar mass.

The most commonly used star-formation diagnostic for high-redshift galaxies is the ultraviolet continuum luminosity over the wavelength range $1500 - 2800$ Å, which is dominated by O and B stars and directly related to the star-formation rate in galaxies where star formation has been proceeding at a roughly constant rate on $\sim 10^8$-year timescales. The rest-frame UV luminosity at $2 \leq z \leq 4$ is based on observed-frame optical photometry. As described in Section 5.1, the colors of star-forming galaxies at high redshift suggest that dust extinction leads

to a significant attenuation of the rest-frame UV luminosity. Therefore, the rest-frame UV luminosities based on optical apparent fluxes must be corrected for dust when calculating intrinsic star-formation rates.

Dust absorbing the radiation from massive stars is heated and re-radiates this absorbed energy in the far-IR region of the spectrum. Therefore, the far-IR luminosity from dust also provides a tracer of the rate of massive star formation. The range "far-IR" is commonly defined as $8 - 1000\mu$m (Kennicutt 1998), and the luminosity spanning this wavelength range is adopted as a tracer of star formation for systems in which star formation has proceeded continuously for at least $10^7 - 10^8$-year timescales. For galaxies with bolometric IR luminosities large enough ($L_{IR} \gtrsim 10^{12} L_{\odot}$) to be detected with ground-based submillimeter telescopes such as SCUBA, the observed 850μm flux can be converted into a far-IR luminosity with an assumption of dust temperature (see Section 5.2). For $z \sim 2$ galaxies with smaller bolometric luminosities (down to $L_{IR} \sim 10^{11} L_{\odot}$), deep *Spitzer*/MIPS 24μm observations have provided a proxy for far-IR luminosity. At $z \sim 2$, the 24μm channel probes a rest wavelength of 8μm, the location of strong PAH emission. Local galaxy templates from Dale & Helou (2002), Chary & Elbaz (2001), Elbaz et al. (2002), and Rieke et al. (2009) are used to convert from the mid-IR to total IR luminosity, which corresponds to an increase by an order of magnitude. Recent *Herschel* Photodetector Array Camera and Spectrometer (PACS) 160μm measurements of the far-IR luminosities of star-forming galaxies at $z \sim 2$ suggest that MIPS 24μm proxies for far-IR luminosities tend to yield overestimates by factors of $\sim 4 - 7.5$ (Nordon et al. 2010). This apparent discrepancy will require additional study. *Spitzer*/MIPS 70μm data probing rest-frame $20 - 25\mu$m at $z \sim 2$ have not been used as widely because of

the limit of the depth of the existing *Spitzer* data, in which very few individual $z \geq 2$ galaxies are detected.

As photons from massive stars ionize nearby interstellar gas, the emission from recombining hydrogen gas in these star-forming regions serves as a proxy for the rate of production of ionizing photons, and, by extension, the formation rate of massive stars. The ionizing flux is dominated by emission from the most massive ($> 10M_{\odot}$) stars and provides an estimate of the instantaneous rate of star formation. With ground-based observations, Hα emission lines have been measured for star-forming galaxies up to $z \sim 2.6$ (at which redshift the thermal background begins to dominate the noise) and used to estimate star formation rates (Erb et al. 2006b, Förster Schreiber et al. 2009). The weaker Hβ feature has also been used to estimate star-formation rates at redshifts beyond $z = 2.6$ (Mannucci et al. 2009, Pettini et al. 2001). In addition to Balmer lines, the Lyα feature has been used as a proxy for star-formation rate. However, due to the resonant nature of the Lyα transition, this line is especially sensitive to the effects of dust extinction and scattering, which can both lead to the preferential destruction of Lyα photons and their diffusion over a large area with reduced surface brightness. Accordingly, there is evidence that even dust-corrected observations of Lyα from individual galaxies tend to underpredict the star formation rate, when compared with other indicators such as rest-frame UV luminosity or Hα emission (Hayes et al. 2011).

Additional star-formation rate diagnostics are based on X-ray and radio luminosities. High-mass X-ray binaries, young supernova remnants, and hot interstellar gas contribute to the X-ray luminosity in star-forming galaxies. Ranalli, Comastri & Sett
calibrate the relation between rest-frame $2 - 10$ keV and far-IR luminosities for

such systems, leading to a relation between hard X-ray luminosity and star-formation rate. Based on the tight linear correlation between far-IR and 1.4 GHz radio luminosity among nearby star-forming galaxies, Yun, Reddy & Condon (2001) derive the relation between star-formation rate and radio luminosity. The deepest current *Chandra* $0.25-2.0$ keV (observed) and VLA 1.4 GHz radio data (e.g., in the GOODS-N region) are still not sufficient for detecting all but the most luminous star-forming galaxies and AGNs at $z \geq 2$. Therefore, most studies that make use of X-ray or radio estimates of star-formation rates use stacking techniques (e.g., Daddi et al. 2007, Pannella et al. 2009, Reddy & Steidel 2004), yielding only sample-averaged properties.

4.2 Evolution of the Star-formation Rate Density

The evolution of the star-formation-rate density is considered one of the most fundamental observational descriptions of the galaxy population as a whole. Matching and explaining this observed evolution is often used as a benchmark of success for theoretical models of galaxy formation. The evolution of the star-formation-rate density is constructed by integrating the luminosity function at a specific wavelength sensitive to star formation (e.g., rest-frame UV, Hα, far-IR, or radio), in order to obtain the associated luminosity density. Then, a conversion between luminosity and star-formation rate (as described in Section 4.1) is used to obtain the associated star-formation-rate density. In such studies, it is crucial to specify the limits down to which the luminosity function is integrated at each redshift (e.g., Bouwens et al. 2007). Also, at shorter wavelengths, such as rest-frame UV and Hα, corrections for dust extinction must be applied in order to obtain the unobscured star-formation rate density (see Section 5.1; Calzetti et al. 2000).

These corrections are sometimes applied in an average sense to the integrated luminosity density, or else in a luminosity-dependent fashion, taking into account the relationship between luminosity and dust obscuration (Hopkins 2004).

The first attempts to chart the star-formation history of the Universe were presented by Madau et al. (1996) and Lilly et al. (1996). At the present, an extensive set of measurements has been compiled by Hopkins (2004) and Hopkins & Beacom (2006) from $z \sim 0$ to $z \sim 6$, using a variety of star-formation rate indicators including rest-frame UV, far-IR, radio, and X-ray continuum luminosities, and both Balmer and forbidden [OII] emission lines. These measurements were all converted to a common cosmology ($\Omega_m = 0.3$, $\Omega_\Lambda = 0.7$, $H_0 = 70$ km s^{-1} Mpc^{-1}), and rest-frame UV and optical measurements were corrected for dust extinction. In Bouwens et al. (2007, 2010), rest-frame UV luminosity functions, both corrected and uncorrected for dust extinction, are used to map the evolution of the star-formation-rate density to $z \sim 8$. As shown in Figure 8, in both of these compilations, the evolution of the star-formation-rate density is characterized by an order-of-magnitude increase from $z \sim 0$ to $z \sim 2$. In more detail, the compilations by Hopkins (2004) and Hopkins & Beacom (2006) show the dust-corrected star-formation-rate density increasing by an order of magnitude from its local value already by $z \sim 1$ and remaining roughly flat to $z \sim 2$. The evolution in Bouwens et al. (2007, 2010) is characterized by a smooth rise all the way from $z \sim 0$ to $z \sim 2$, due to a different extinction correction adopted for the rest-frame UV data at $z < 2$. In both versions of the cosmic star-formation history, the global star-formation-rate density remains roughly constant between $z \sim 2$ and $z \sim 4$, and then declines towards higher redshift. Hopkins & Beacom (2006) propose that the star-formation history is constrained to within $\sim 30 - 50\%$ up

to $z \sim 1$ and within a factor of ~ 3 at higher redshifts. Additionally, recent results from Reddy et al. (2008) suggest that $\sim 70 - 80\%$ of the star-formation-rate density at $z \sim 2 - 3$ is produced by galaxies with bolometric luminosities $L_{bol} \leq 10^{12} L_{\odot}$, and that the highly-obscured ULIRGs selected by submillimeter surveys (e.g., Chapman et al. 2005), although individually luminous, do not dominate the star-formation-rate density.

4.3 Stellar Population Synthesis Models

While luminosities tied to individual specific wavelength ranges are commonly used to infer the current rate of star formation, the multiwavelength SED of a galaxy can be interpreted in terms of its integrated stellar, dust and metal content, and its past history of star formation. This technique is referred to as stellar population synthesis modeling, and was first employed by Tinsley (1968). In the intervening decades, stellar population synthesis models have become increasingly sophisticated, and have played a crucial role in inferring the physical properties of galaxies both near and far based on their photometric and spectroscopic properties. Population synthesis models are also used to estimate photometric redshifts, in so far as the observed multiwavelength photometry of a galaxy is fit in terms of not only best-fitting stellar population parameters, but also redshift.

The basic ingredients of stellar population synthesis models consist of a theoretical prescription for all stages of stellar evolution as a function of mass and metallicity, as well as a stellar spectral library of the observed properties of stars at different positions in the Hertzsprung-Russell diagram. The time evolution of the integrated spectrum from a coeval population of stars described by a specific stellar IMF and metallicity can then be predicted. For a given star-formation

history, the evolution of the integrated spectrum of stars is computed by summing the contributions of simple stellar populations formed at successive time steps, with the normalization at each time step determined by the corresponding star-formation rate. Thus, stellar population synthesis models can predict the evolution of the integrated spectrum of a stellar population for an arbitrary star-formation history, IMF, and stellar metallicity. Stellar population synthesis models are often coupled with theoretical models (Charlot & Fall 2000) or empirical parameterizations (Calzetti et al. 2000) of dust extinction to explain the observed properties of galaxies in terms of both stellar and dust content. The resulting model galaxy spectrum can be passed through photometric filters in order to predict the evolution of luminosities, colors, and mass-to-light ratios in specific photometric bands. Additional properties of the stellar population can also be calculated, including the rate of Type Ia and Type II supernovae explosions, the mass in stellar remnants and recycled gas, and the ionizing photon luminosity.

Currently, there are several different stellar population synthesis models employed for fitting the SEDs of distant galaxies. Perhaps most widely used are the models of Bruzual & Charlot (2003) and their current version (Charlot & Bruzual 2011, in preparation), though other significant theoretical efforts include the PEGASE and Starburst99 models (Fioc & Rocca-Volmerange 1997, Leitherer et al. 1999), and, more recently, the models of Maraston (2005) and Conroy, Gunn & White (2009). There is much ongoing discussion in the literature regarding the systematic uncertainties and differences among these different stellar population synthesis codes, in terms of their descriptions of various stages of stellar evolution off of the main sequence.

There has been a particular focus on the treatment of the thermally-pulsating

asymptotic giant branch (TP-AGB). TP-AGB stars are red giants with low- to intermediate-mass main sequence progenitors, which make a significant contribution to the near-IR luminosity of a simple stellar population at ages between 0.5 and 2.0 Gyr. As emphasized by Maraston (2005), derived properties such as the age and near-IR mass-to-light ratio, and, correspondingly, the inferred stellar mass, will be very sensitive to the treatment of TP-AGB stars in systems in an evolutionary state that prominently features these stars. As a result, the stellar populations in which the correct treatment of the TP-AGB matters the most are post-starburst systems, as opposed to those in which star formation is proceeding at a roughly constant rate (Daddi et al. 2007). As shown in Figure 9, in the models of Maraston (2005), TP-AGB stars make a much more significant contribution to the integrated galaxy luminosity at ~ 1 Gyr than in the models of Bruzual & Charlot (2003), resulting in systematically lower derived stellar masses and ages, in particular for post-starburst systems (Maraston et al. 2006). Rather than adopting a specific prescription for the contribution of the TP-AGB phase, Conroy, Gunn & White (2009) parameterize the luminosities and effective temperatures of TP-AGB stars as variables to be constrained by the actual data. Systematic uncertainties in TP-AGB parameters therefore translate into systematic errors in other derived properties such as stellar mass and past star-formation history. Recently, Kriek et al. (2010) constructed a composite SED over the rest-frame range $1200 - 40000$ Å for a sample of 62 post-starburst galaxies at $0.7 \leq z \leq 2.0$ drawn from the NEWFIRM Medium-Band Survey. In contrast to the results of Maraston et al. (2006), this entire SED is fit well by the Bruzual & Charlot (2003) models, whereas the rest-frame optical and near-IR regions of the spectrum are not simultaneously fit by the models of Maraston. The

SED-fitting results of Kriek et al. (2010) suggest that the Maraston models give too much weight to the TP-AGB phase. Clearly, consensus has yet to be reached about the influence of TP-AGB stars in the integrated spectra of galaxies.

Uncertainties in the detailed nature of the stellar IMF also translate into systematic uncertainties in the conversion between luminosity and stellar mass. For the range of stellar populations typically observed at high redshift (i.e., when the Universe was less than a few Gyr old), and over the rest-frame UV to near-IR wavelength range where current observations probe, models with the same star-formation history and the assumption of either a Chabrier (2003) or Salpeter (1955) IMF over the mass range $0.1 - 100 M_{\odot}$ produce virtually identical colors. However, the model assuming a Chabrier (2003) IMF corresponds to a stellar mass a factor of ~ 1.8 lower. Although both IMFs are described by power-law functions at $M \geq 1 M_{\odot}$, the Chabrier (2003) IMF follows a log-normal distribution below $1 M_{\odot}$, turning over at the so-called "characteristic mass," whereas the Salpeter (1955) IMF continues to increase as a power-law all the way down to $0.1 M_{\odot}$.

Evidence in the local and low-redshift Universe suggests that the Chabrier (2003) IMF yields stellar M/L ratios for lower-mass elliptical galaxies (with velocity dispersions of $\sigma \sim 200$ km s^{-1}) in agreement with their luminosities and dynamical mass estimates. On the other hand, elliptical galaxies with larger dynamical masses appear to be characterized by either steeper (i.e., more Salpeter-like) IMFs or higher dark-matter fractions (Graves & Faber 2010, Treu et al. 2010). There are also extreme environments such as the Galactic Center and surrounding starburst clusters such as the Arches, in which direct evidence for IMF variations has been reported (Stolte et al. 2002). At higher redshift, based on more indirect

methods such as measuring the simultaneous $U-V$ color and stellar B-band M/L ratio evolution for elliptical galaxies at $z \sim 0$ to $z \sim 0.8$ (with the latter estimated from the observed evolution in the fundamental plane), van Dokkum (2008) infers that the stellar IMF for elliptical galaxy progenitors had a flatter slope at $z \sim 4$ in the regime near $1M_{\odot}$. Furthermore, the characteristic mass at which the log-normal portion of the IMF turns over is inferred to shift to $\sim 2M_{\odot}$. Adopting a completely independent approach based on a comparison of the star-formation rates and stellar masses of vigorously star-forming galaxies at $z \sim 2$, Davé (2008) also infers a higher characteristic mass at this redshift. An upward shift in characteristic mass results in an IMF that is more "bottom light" than the present-day Chabrier (2003) function, and a lower conversion factor from light to stellar mass. In contrast, recently van Dokkum & Conroy (2010) analyzed the spectra of four elliptical galaxies in the Virgo cluster and, based on the strength of stellar absorption features tracing $M < 0.3M_{\odot}$ stars, concluded that the IMF in the massive star-forming progenitors of these systems had a "bottom heavy" IMF *steeper* than Salpeter between 0.1 and $1.0M_{\odot}$.

Bastian, Covey & Meyer (2010) review evidence for IMF variations both in the local Universe and at significant cosmological distances for the most part with skepticism. Clearly additional study is required to quantify or rule out the evidence for IMF variations as a function of environment. Stellar population synthesis models featuring explicit parameterizations of the most unconstrained phases of stellar evolution, as well as the form of the stellar IMF, will yield confidence intervals for derived stellar population parameters that more accurately reflect the systematic uncertainties associated with stellar population modeling (Conroy, Gunn & White 2009).

In spite of the significant uncertainties associated with stellar population synthesis modeling, it is now standard practice to use such models to infer basic physical properties of galaxies over a wide range of redshifts. In the local Universe for a sample of $> 10^5$ SDSS galaxies, a combination of optical broadband photometric properties and spectral indices (the 4000 Å spectral break and the strength of Balmer absorption lines) have been modeled using the population synthesis code of Bruzual & Charlot (2003) to infer galaxy properties such as star-formation history, dust attenuation, and stellar mass (Kauffmann et al. 2003a). At higher redshifts, stellar population modeling is typically tuned to broadband photometry alone, as rest-frame optical spectra are not of sufficient quality to measure stellar absorption features or detailed continuum shape at high S/N. At $z \geq 2$, stellar population synthesis modeling is only possible if the rest-frame SED is probed at wavelengths both above and below age-sensitive spectral discontinuities such as the Balmer or 4000 Å break. Therefore, optical photometry probing the rest-frame UV must be, at the very least, combined with data probing the rest-frame optical regime (i.e. near-IR observed wavelengths), and, preferably, with additional *Spitzer*/IRAC photometry probing the rest-frame near-IR. Early models of $z > 2$ stellar populations were featured in Sawicki & Yee (1998), Shapley et al. (2001), and Papovich, Dickinson & Ferguson (2001) (LBGs) and Förster Schreiber et al. (2004) (DRGs). A fairly recent example of $z \sim 2$ stellar population modeling from Muzzin et al. (2009) is shown in Figure 10. This analysis is based on extremely well-sampled SEDs for spectroscopically-confirmed galaxies including optical, near-IR, and *Spitzer*/IRAC photometry as well as binned Gemini/GNIRS near-IR spectra, and features a systematic comparison of the parameters derived from Maraston (2005), Bruzual & Charlot (2003), and

updated Charlot & Bruzual models. Stellar population synthesis models are now routinely used to derive high-redshift galaxy physical properties. Such modeling is a standard component of the derivation of global distributions such as the galaxy stellar mass function (Section 4.5).

For the modeling of high-redshift galaxy stellar populations, in addition to the adoption of a particular stellar population synthesis code, the stellar IMF and metallicity are assumed parameters. A specific, wavelength-dependent dust extinction law (e.g., starburst, SMC, Milky Way) is also assumed. The star-formation history, $SFR(t)$, is commonly parameterized in the form of an exponential decline, with $SFR(t) = SFR_0 \times \exp(-t/\tau)$. In this case, τ, the e-folding time, and t, the time since the onset of star formation, are both parameters to constrain. With such a parameterization, a continuous star-formation history corresponds to $\tau = \infty$ and $SFR(t) = SFR_0$. In addition to single episodes describing the star-formation rate as a function of time, more complex functions for the history of star formation have been considered. In particular, two-component models consisting of the linear combination of an old, high mass-to-light ratio component and a younger population with ongoing star formation, have been used to constrain how much stellar mass from the old stellar population could be "hiding" under the glare of a younger burst of star formation. In addition to τ and t, the parameters commonly derived for high-redshift galaxies are indicators of the degree of dust extinction [$E(B-V)$ or A_V], the current star-formation rate, and the integrated stellar mass. For a given stellar population synthesis code, the stellar mass has been demonstrated to be the best-constrained parameter (Papovich, Dickinson & Ferguson 2001; Shapley et al. 2001, 2005), whereas other parameters are more subject to uncertainties in the nature of the star-

formation history (i.e., τ), which is difficult to constrain in the absence of external multiwavelength information. Recently, Maraston et al. (2010) have in fact argued that so-called "inverted-τ" models [i.e. models in which the star-formation rate increases with time as $SFR(t) = SFR_0 \times \exp(+t/\tau)$] provide a better description of the extinction and star-formation rate based on rest-frame UV data alone, as well as the star-formation rates and stellar masses of mock high-redshift galaxies constructed from semi-analytic models. In addition, Papovich et al. (2011) demonstrate that the globally averaged relations between the star-formation rates and stellar masses of galaxies at high redshift (see Section 4.6) appear to favor rising star-formation histories, as opposed to ones that are constant or declining. The best parameterization of the star-formation histories of high-redshift galaxies is clearly still a matter of debate.

4.4 The Diversity of High-Redshift Stellar Populations

The methods described above have been used to investigate the stellar populations of high-redshift galaxies selected using the various techniques discussed in Section 2. Based on the results of stellar population syntehsis modeling, we can make some general comments about the range of stellar populations observed, while keeping in mind the uncertainties inherent to the modeling process, and the biases that different selection techniques impose. If the current samples of UV-selected galaxies are roughly characterized by star-formation rates of $10 - 100 M_{\odot}$ yr^{-1}, typical stellar masses of $1 - 5 \times 10^{10} M_{\odot}$ (Erb et al. 2006c, Reddy & Steidel 2004, Shapley et al. 2001), and moderate amounts of extinction in the rest-frame UV (factor of ~ 5), the very complementary sample of rest-frame optically selected DRGs are typically characterized by higher star-

formation rates ($\geq 100 M_{\odot}$ yr^{-1}), stellar masses (down to the typical survey limits of $K \sim 21$ Vega) of $\sim 10^{11} M_{\odot}$, and larger amounts of dust extinction in the rest-frame UV and optical ranges of the spectrum (Förster Schreiber et al. 2004, Papovich et al. 2006). At the same time, a minority of DRGs show little evidence for ongoing star formation (van Dokkum et al. 2008). In addition to their prodigious star-formation rates, SMGs appear to be characterized by stellar masses that are comparable to those of the typical DRGs, and several times larger on average than those of UV-selected galaxies (Borys et al. 2005; Michałowski, Hjorth & Watson 2010). However, it is worth keeping in mind that the effects of dust extinction and AGN contamination on the broadband SED lead to larger systematic uncertainties in the derived stellar populations of SMGs. At the other end of the spectrum, so to speak, the stellar populations of LAEs are characterized by less dust extinction on average even than those of the UV-selected galaxies (Gawiser et al. 2007). Due to the typically faint rest-frame UV luminosities of emission-line selected galaxies, the LAEs also tend to be faint in the rest-frame UV continuum, with lower star-formation rates than those of UV-selected galaxies, which were targeted down to a brighter continuum limit (Kornei et al. 2010).

In addition to considering the typical properties of galaxies as a function of selection method – which may not have anything other than historical value – it is also worth mentioning the range of star-formation histories observed as a function of mass. In particular, at high stellar masses ($M > 10^{11} M_{\odot}$, assuming a Salpeter IMF from $0.1 - 100 M_{\odot}$), there exist at $z \sim 2$ not only active star-forming galaxies with $SFR > 100 M_{\odot}$ yr^{-1}, but also passive, evolved galaxies with little evidence for ongoing star formation (Kriek et al. 2008a, van Dokkum et al. 2008). Quiescence and mature stellar populations constitute the physical interpretation of the

empirically-derived red sequence reported by Kriek et al. (2008a) and described in Section 3.2. These quiescent galaxies appear to consitute $\sim 40-50\%$ of the most massive galaxies ($M_{star} \geq 10^{11} M_{\odot}$ at $z \sim 2-3$). Based on these results, it is worth noting that, in contrast to the patterns observed in the local Universe, at least half of most massive galaxies at $z \sim 2$ are still actively in the process of forming (Daddi et al. 2007, Papovich et al. 2006), and that there is an incredible diversity observed among the star-formation histories of these massive galaxies. At the same time, it is a challenge to explain massive galaxies at early times with little evidence for ongoing star formation, given that theoretical models predict copious rates of mass accretion at $z \sim 2$ for such massive systems (e.g., Dekel, Sari & Ceverino 2009).

4.5 Evolution of the Stellar Mass Density

Stellar population synthesis modeling provides a powerful tool for estimating the global evolution of the stellar content in galaxies, which reflects the combined processes of star formation and mergers. This evolution is described by constructing the galaxy stellar mass function at a range of redshifts. Analogous to the galaxy luminosity function, the stellar mass function is parameterized in terms of a characteristic mass, M^*_{star}, low-mass slope, α, and overall normalization, Φ^*. At each redshift, the stellar mass function can be integrated to determine the corresponding stellar mass density. Alternatively, the growth in stellar mass as a function of galaxy mass can provide important insights into galaxy formation models. The cosmic stellar mass density should also reflect the integral of past star formation in the Universe, and therefore the integral of the star-formation-rate density described in Section 4.2 can be compared for consistency with the

independently-derived stellar-mass density.

In the local Universe, the galaxy stellar mass function has been determined from large samples of galaxies drawn from the 2dFGRS matched to the 2 Micron All-Sky Survey (2MASS), and SDSS (Baldry, Glazebrook & Driver 2008; Cole et al. 2001). Presently, stellar mass functions have been measured out to $z \sim 5$, suggesting that roughly half of the local stellar mass density appears to be in place at $z \sim 1$. Measurements of the stellar mass function at $z > 1$ are based on samples with multiwavelength (optical and IR) photometry and primarily photometric redshifts. The first determination of the stellar mass function at $z \sim 2 - 3$ was presented in Dickinson et al. (2003), based on a sample of rest-frame B-band-selected objects in the Hubble Deep Field North (HDF-N) with both optical and near-IR photometry. Subsequently, many other groups have measured stellar mass functions at $z \geq 2$, selecting galaxies at optical, near-IR and mid-IR wavelengths (e.g., Drory et al. 2005; Elsner, Feulner & Hopp 2008; Fontana et al. 2004, 2006; Pozzetti et al. 2007).

Both Pérez-González et al. (2008) and Marchesini et al. (2009) construct stellar mass functions at $z \geq 2$ based on fairly deep (near-IR and mid-IR magnitude limits of $23 - 25$ AB) and wide-area ($500 - 700$ arcmin^2) surveys, selected, respectively, with IRAC and K-band data. The larger areas of these surveys, compared to previous determinations, provide results that are less susceptible to cosmic variance. As shown in Marchesini et al. (2009), the $2 \leq z \leq 3$ stellar mass functions in the literature, when integrated over a fixed range in stellar mass ($10^8 \leq M_{star}/M_{\odot} < 10^{13}$), vary by a factor of ~ 3 in stellar mass density. Figure 11 (from Marchesini et al. 2009) features a compilation of global stellar mass density estimates as a function of redshift. At $z \sim 2$, the reported fraction

of the local stellar mass density that is in place ranges from $\sim 8-25\%$, while that number drops to $\sim 4-12\%$ at $z \sim 3.5$. Marchesini et al. (2009) also offer an in-depth analysis of the random and systematic uncertainties involved in constructing a stellar mass function from the modeling of multiwavelength photometry. These include the errors associated with photometric redshifts, cosmic variance, differences among stellar population synthesis codes (as parameterized by, e.g., Conroy, Gunn & White 2009), choice of stellar IMF, stellar metallicity, and extinction law. A proper accounting for these sources of random and systematic error significantly increases the uncertainties on derived quantities such as the evolution of the global stellar mass density, as well as the evolution of galaxies as a function of stellar mass. For example, when only taking into account random uncertainties, Marchesini et al. (2009) find that the abundance of galaxies below the characteristic mass evolves more strongly with redshift than that of the most massive galaxies ($M_{star} > 10^{11.5}$), which show a lack of strong evolution in number density. However, when the full random and systematic error budget is accounted for, more significant evolution in the abundance of massive galaxies cannot be ruled out.

Additional uncertainties in the stellar mass density at high redshift result from uncertainties in the low-mass slope of the stellar mass function. While most works adopt α in the range to -1.0 to -1.4, the stellar mass regime crucial for constraining this parameter is not well probed with current observations. For example, the dataset featured in Marchesini et al. (2009) suffers from incompleteness below $\sim 10^{10} M_{\odot}$. According to Reddy & Steidel (2009), if the stellar mass function has a steeper low-mass slope, as suggested by the steep faint-end slope of the rest-frame UV luminosity function and the relationship between UV luminosity and

stellar mass, up to $\sim 50\%$ of the stellar mass density may be contained in galaxies with stellar masses $\leq 10^{10} M_{\odot}$, as opposed to the $\sim 10-20\%$ inferred from extrapolating the Schechter fits of Marchesini et al. (2009). In fact, using a K-selected sample based on significantly deeper near-IR imaging with Subaru/MOIRCS ($K = 24.1$ Vega), Kajisawa et al. (2009) estimate a steeper low-mass slope of $\alpha = -1.5$ at $z \sim 2$ and $\alpha = -1.6$ at $z \sim 3$, as well as perhaps a trend of α steepening with redshift, also suggested by Fontana et al. (2006). This result is intriguing, but the area over which the low-mass slope is adequately probed is only 28 arcmin^2. Clearly, data of this depth must be collected over a significantly wider area to minimize the effects of cosmic variance and obtain more robust constraints on the stellar mass density at $z > 2$. In particular, constraining the abundance and dust-extinction properties of faint, low-mass galaxies at high redshift will prove very important for comparisons of the past integral of the star-formation-rate density with the stellar mass density at each redshift (Reddy & Steidel 2009). Careful comparisons of this sort are crucial for determining whether or not the integral of global past star formation indicates a discrepancy with the global stellar mass density (Wilkins, Trentham & Hopkins 2008).

4.6 $SFR - M_{star}$ Scaling Relations

In addition to considering the evolution of star-formation rates and stellar masses in galaxies separately, the evolution of the relationship between these quantities provides important clues as to how stellar mass builds up in galaxies as a function of redshift *and* mass. At $z \sim 2$, this relationship is highlighted by Daddi et al. (2007) in a sample of star-forming $sBzK$ galaxies (passive $pBzK$ galaxies and galaxies with no MIPS 24μm detection were excluded from this anal-

ysis). Using star-formation rates estimated from either dust-corrected UV luminosity, or the sum of mid-IR and uncorrected UV luminosities, Daddi et al. (2007) find a strong correlation between star-formation rate (SFR) and stellar mass, described by the relation, $SFR \propto M_{star}^{0.9}$, and shown in Figure 12. The ultra-luminous SMGs are outliers to the $SFR-M_{star}$ trend, with star-formation rates a factor of ~ 10 higher than expected, given their stellar masses. Pannella et al. (2009) used 1.4 GHz radio stacking observations to estimate average star-formation rates for non-AGN $sBzK$ objects in the Cosmic Evolution Survey (COSMOS) field, binned by stellar mass. The radio stacking analysis reveals the trend $SFR \propto M_{star}^{0.95}$, consistent with Daddi et al. (2007). Accordingly, the specific star-formation rate, i.e. the star-formation rate divided by stellar mass, appears to be roughly constant over an order of magnitude in stellar mass ($10^{10} - 10^{11} M_{\odot}$, assuming a Salpeter IMF from $0.1-100 M_{\odot}$). Similar trends between star-formation rate and stellar mass have been observed among star-forming galaxies at $z \sim 1$ by Elbaz et al. (2007) and Noeske et al. (2007), but with a lower overall normalization, such that, at a given fixed stellar mass, the expected star-formation rate is a factor of ~ 4 lower. A comparison with the trend observed in the local Universe (Brinchmann et al. 2004, Elbaz et al. 2007) indicates an evolution by a factor of $\sim 30 - 40$ (Daddi et al. 2007, Pannella et al. 2009).

On the other hand, perhaps the tightness of the $SFR - M_{star}$ correlation has been overemphasized, as a result of selection effects. Using the same ultra-deep, K-selected sample described in Section 4.5, Kajisawa et al. (2010) investigate the $SFR - M_{star}$ relation from $0.5 \leq z \leq 3.5$. At $z \sim 2$, these authors find significantly more scatter at the high-stellar-mass end of the relation. In this study, UV dust-corrected and mid-IR+UV star-formation rates are estimated

using the same techniques as in Daddi et al. (2007), but there is no requirement for galaxies to be detected at 24μm. At $M_{star} = 10^{11} M_{\odot}$, for example, UV dust-corrected star-formation rates range from $1 - 1000 M_{\odot}$ yr^{-1}. Furthermore, the power-law slope between star-formation rate and mass, and therefore, the specific star-formation rate, tend to decrease at $M_{star} > 10^{10.5} M_{\odot}$. Given that the slope and small scatter of the $SFR - M_{star}$ relation has been interpreted in terms of lending support to galaxy formation models in which smooth gas accretion dominates the growth of galaxies at high redshift (Davé 2008), it is crucial to characterize these quantities accurately and in an unbiased manner. The above studies are largely based on photometric redshifts, which tend to increase the uncertainties in all derived physical properties. Therefore, larger spectroscopic samples are needed. Based on such spectroscopic studies, a description of the distribution of star-formation rates as a function of stellar mass for a *stellar-mass selected* sample will provide the ideal observational probe of this potentially meaningful trend.

5 THE INTERSTELLAR CONTENT OF HIGH-REDSHIFT GALAXIES

The stellar content of galaxies offers an incomplete version of the story of their formation and evolution, which must be filled in by a characterization of their interstellar environments. Indeed, the multiwavelength study of the current and past history of star formation in galaxies cannot be constructed without understanding the nature of dust. In addition to attenuating and reddening the radiation from stars, dust also reradiates the absorbed emission in the IR with a characteristic overall spectral shape that depends on temperature. The detailed

emission spectrum in the mid-IR offers a further probe of the energy sources heating dust grains (i.e., radiation from star formation or an AGN). While dust reprocesses the light from stars, it is the cool gas content of galaxies that forms the very fuel for star formation. The elevated rate of star formation in galaxies in the early Universe is a direct result of the large cool gas fractions in these systems. As stars evolve and die, they return gas and heavy elements to the ISM. The patterns of chemical enrichment in both gas and stars therefore reflect the past history of star formation, and of gas inflows and outflows in galaxies. In this section, we review what is known about the interstellar contents of high-redshift galaxies. We begin by discussing both dust extinction and reprocessed emission, and then turn to observations of the molecular gas and metals, all of which provide important insights into the nature of distant galaxies.

5.1 Dust Extinction

Starburst galaxies in the local Universe follow a correlation between attenuation and reddening. As these galaxies become more attenuated in the rest-frame UV (as probed by the ratio of far-IR to UV luminosities), their rest-frame UV continua become redder. Based on multiwavelength observations spanning from the UV to far-IR, this correlation has been quantified as a relationship between the rest-frame UV slope, β (where $f_\lambda \propto \lambda^\beta$), and A_{1600} (the attenuation at 1600 Å), such that $A_{1600} = 4.43 + 1.99\beta$ (Meurer, Heckman & Calzetti 1999). The starburst obscuration curve of Calzetti et al. (2000) describes the wavelength dependence of effective attenuation when dust is distributed in a patchy foreground screen, relative to young stars. For reference, the Calzetti et al. (2000) curve lacks the 2175 Å bump characteristic of the Milky Way extinction curve, and has a

different ratio of total to selective extinction, with $R_V = A_V/E(B-V) = 4.05$, as opposed to the average Milky Way value of 3.1 (Cardelli, Clayton & Mathis 1989). The Calzetti et al. (2000) law is also "grayer" than the SMC law (Prevot et al. 1984), rising less steeply in the near-UV, and therefore implying more attenuation for a given reddening in the rest-frame UV. This "grayness" likely stems from a geometrical configuration between gas and stars in which the dust is distributed in a patchy foreground-like screen, and some stars suffer little or no extinction (Calzetti 2001). This starburst attenuation curve predicts an almost identical relation between A_{1600} and β to that of Meurer, Heckman & Calzetti (1999), with the assumption of fairly uniform intrinsic rest-frame UV colors for starburst galaxies.

Soon after the discovery of LBGs at $z \sim 3$, their observed range of rest-frame UV colors was interpreted in terms of a range of dust reddening (Calzetti et al. 2000; Meurer, Heckman & Calzetti 1999; Steidel et al. 1999), in analogy with the description of local starbursts. The Calzetti et al. obscuration curve was used to translate between rest-frame UV color and $E(B-V)$, and, by extension, A_{1600}, with the average value of $E(B-V) = 0.15$ corresponding to an attenuation factor of ~ 4.7 at 1500 Å. In Steidel et al. (1999), this factor was used to correct the observed UV-luminosity densities at $z \sim 3$ and $z \sim 4$ and show that only a small fraction of the intrinsic UV radiation typically escapes from even UV-selected galaxies at high redshift. Furthermore, consistent with the trend observed among starbursts in the local Universe, Adelberger & Steidel (2000) find that objects with greater bolometric luminosities suffer more extinction in the rest-frame UV. However, the trend at $z \sim 3$ is offset from the local one in the sense that, for a given bolometric luminosity (i.e. star-formation rate), the ex-

tinction is significantly smaller at higher redshift. Bouwens et al. (2009) have investigated the average reddening as a function of rest-frame UV luminosity (uncorrected for dust), demonstrating that, at $z \sim 2.5$ and $z \sim 4.0$, β becomes bluer for fainter objects. Furthermore, the average β value of the most UV-luminous galaxies is redder at $z \sim 2.5$ than at $z \sim 4.0$. The trend between β and UV luminosity was not apparent in the datasets of Adelberger & Steidel (2000) and Reddy et al. (2008), most likely due to the smaller dynamic range of UV luminosities probed.

At this point, the Calzetti et al. (2000) law is the most commonly adopted extinction law for modeling the stellar populations of high-redshift galaxies (Section 4). Therefore, it is important to consider the empirical support for this choice, based on comparisons between UV-extinction-corrected and extinction-free estimates of star-formation rates. While individual star-forming galaxies are not detected in deep *Chandra* X-ray and and VLA 1.4 GHz radio imaging observations, stacking methods have proven very powerful for comparing different multiwavelength star-formation rate indicators. Reddy & Steidel (2004) measure the stacked X-ray and radio fluxes for spectroscopically-confirmed, UV-selected star-forming galaxies at $1.5 \leq z \leq 3.0$ in the GOODS-N field. On average, the inferred X-ray and radio-derived star-formation rates are, respectively, 42 and 56 $M_{\odot}$ yr^{-1}. The UV star-formation rate, extinction corrected based on rest-frame UV colors and assuming the validity of the Calzetti et al. law, is 50 $M_{\odot}$ yr^{-1} – consistent with the radio and X-ray estimates. Furthermore, the ratio of star-formation rates derived from X-ray and uncorrected UV fluxes implies a factor of $\sim 4.5 - 5.0$ attenuation in the UV, consistent with the attenuation inferred from the UV colors. Pannella et al. (2009) perform a

similar radio stacking analysis for star-forming $sBzK$ galaxies with photometric redshifts at $z \sim 2$ in the COSMOS field, finding that the UV attenuation, A_{1500}, derived from the ratio between the extinction-free radio-derived star-formation rate and the UV-uncorrected star-formation rate, agrees well with that inferred on the basis of rest-frame UV colors alone, assuming the Calzetti et al. (2000) law applies.

Spitzer/MIPS 24μm observations have allowed for a test of extinction on a per object basis at $z \sim 2$. Reddy et al. (2010, 2006) compute mid-IR luminosities from observed 24μm fluxes for spectroscopically-confirmed UV-selected galaxies, and extrapolate these to total IR luminosities using local templates (Elbaz et al. 2002). The relation between extinction (L_{FIR}/L_{1600}) and reddening (β) for these UV-selected galaxies is compared with the relation among local starbursts, revealing that the majority of objects (though not all – see below) follow the local trend. Furthermore, Reddy et al. (2006) confirm the result of Adelberger & Steidel (2000) of the positive correlation between bolometric luminosity and extinction, but now based on a *Spitzer*/MIPS estimate of the IR luminosity. The evolution in extinction with redshift is also reproduced using *Spitzer*, which suggests that extinction in the rest-frame UV is a factor of ~ 10 smaller at $z \sim 2$ than at $z \sim 0$, at fixed bolometric luminosity. Daddi et al. (2007) perform an analogous test of UV extinction laws, using star-formation rates for star-forming $sBzK$ galaxies derived from both rest-frame UV and *Spitzer* 24μm fluxes. Daddi et al. (2007) also conclude that the Calzetti et al. law is valid for the the majority of systems at $z \sim 2$.

While the success of the Calzetti et al. (2000) law is impressive, in terms of correcting UV luminosities and matching various extinction-free tracers of star-

formation rates for large samples of high-redshift galaxies, it is also important to highlight the cases in which it appears to fail. For example, in ultraluminous SMGs at $z \sim 2$, the dust-corrected UV luminosities (assuming the Calzetti et al. law) underpredict the bolometric luminosities suggested by submillimeter and radio luminosities by as much as a factor of $\sim 10 - 100$ (Chapman et al. 2005, Daddi et al. 2007, Reddy et al. 2006). A related yet rather non-intuitive fact is that $\geq 50\%$ of the SMGs in the Chapman et al. (2005) sample have rest-frame UV colors that actually satisfy the UV-selection criteria of Steidel et al. (2003, 2004). The mismatch between predicted (based on rest-UV color) and observed IR luminosities, shown in Figure 13 (left), may arise in systems where regions of massive star formation are completely opaque to UV radiation, and the UV radiation that does escape is from regions that are disjoint from the dusty ones dominating the bolometric output (Daddi et al. 2007). Reddy et al. (2006) find that the Calzetti et al. (2000) law appears to break down at $z \sim 2$ for systems more luminous than $\sim 2 \times 10^{12} L_{\odot}$. On the other hand, Magdis et al. (2010a) demonstrate that, at $z \sim 3$, the starburst attenuation curve yields consistent results for galaxies with bolometric luminosities as large as $10^{13} L_{\odot}$. In general, however, the Calzetti et al. (2000) law does not appear valid for describing dust extinction in the most luminous sources at $z \geq 2$.

While the local starburst relation appears to underpredict the UV attenuation for the most bolometrically luminous systems, there is a discrepancy in the opposite sense for objects that, based on their stellar population modeling, appear "young," with best-fit ages (assuming constant star-formation histories) less than 100 Myr. This second discrepancy was highlighted most dramatically in the case of the strongly gravitationally-lensed objects MS1512-cB58 (or "cB58")

(Pettini et al. 2000) and the Cosmic Eye (Smail et al. 2007). Both of these objects have rest-frame UV colors and continuum slopes that suggest dust-corrected star-formation rates several times larger than what is actually measured using *Spitzer*/MIPS mid-IR photometry and InfraRed Spectrograph (IRS) spectroscopy (a factor of $\sim 3 - 5$ for cB58, and ~ 8 for the Cosmic Eye) (Siana et al. 2009, 2008). This discrepancy, shown in Figure 13 (right), was previously noted for cB58 on the basis of millimeter and submillimeter observations (Baker et al. 2001, Sawicki 2001).

A similar discrepancy is observed by Reddy et al. (2010, 2006) among UV-selected galaxies with best-fit stellar population ages of $t \leq 100$ Myr. As shown in Figure 13 (left), the measured ratio of L_{FIR}/L_{UV} for these young systems falls significantly below the local starburst relation, given their observed rest-frame UV slopes, β. Both cB58 and the Cosmic Eye are described by similarly young ages as well. Therefore, it appears that these young systems are described by a different extinction law, one that is steeper (as in the case of the SMC curve), such that a given observed amount of reddening corresponds to less attenuation in the rest-frame UV. More work is needed to develop a self-consistent evolutionary scenario to explain the reddening and attenuation properties of star-forming galaxies as a function of the maturity of their stellar populations. Finally, we call attention to recent results based on *Herschel* PACS 160μm measurements of star-forming galaxies at $z \sim 2$ (Nordon et al. 2010). A comparison of PACS and UV, dust-corrected star-formation rates indicates that the UV-corrected values are, on average, 0.3 dex higher (with a scatter of 0.35 dex). More extensive comparisons with upcoming PACS far-IR measurements will be vital for further testing of the Calzetti et al. law.

Related to the overall reliability of the Calzetti et al. law, we must also consider the question of differential extinction of the radiation from stars and ionized gas. In local starbursts, emission-line tracers of ionized gas appear to be systematically more attenuated than the stellar continuum at similar wavelengths. The relationship derived between the stellar and nebular extinction is $E(B-V)_{stars} = 0.44E(B-V)_{nebular}$ (Calzetti et al. 2000). Currently, there is conflicting evidence about the relative extinction of stars and gas at $z \sim 2$. Comparing star-formation rates inferred from rest-frame UV and Hα luminosities for a sample of $z \sim 2$ UV-selected galaxies (see Section 5.4), Erb et al. (2006b) conclude that $E(B-V)_{stars} \approx E(B-V)_{nebular}$, and that a Calzetti et al. law applied to correct both UV-continuum and Hα measurements gives rise to the best agreement between star-formation rate indicators. On the other hand, Förster Schreiber et al. (2009) find for a set of star-forming galaxies with VLT/SINFONI integral-field unit (IFU) maps of Hα emission at roughly the same redshift as the Erb et al. sample (see Section 6.2.1) that the best agreement between Hα and UV-derived star-formation rates results when Hα luminosities are corrected by an additional factor of ~ 2, and with the assumption $E(B-V)_{stars} = 0.44E(B-V)_{nebular}$. To settle the question of differential extinction, much larger samples of objects are required with both measurements of multiple Balmer emission lines and rest-frame UV estimates of star-formation rates. Assembling these measurements will be possible with the next generation of multi-object near-IR spectrographs presently coming on-line on $8-10$-meter class telescopes.

5.2 Dust Emission

In addition to absorbing ultraviolet and optical radiation from stars, dust re-emits at IR and submillimeter wavelengths. Direct observations of this re-radiated emission at long wavelengths have opened a window into the nature of dust in distant galaxies, in terms of its temperature, composition, and the sources heating it. At far-IR and submillimeter wavelengths, direct observations of dust emission are restricted to the most luminous sources, with $L_{bol} > 10^{12} L_{\odot}$. While mid-IR imaging observations have been obtained for lower-luminosity systems using *Spitzer*/MIPS, spectroscopy has been limited to the most luminous sources, selected on the very basis of their bright submillimeter or mid-IR emission [except in cases of strongly gravitationally-lensed systems (Siana et al. 2009)].

Until recently, direct measurements of dust temperatures in $z > 2$ ULIRGs only existed for small samples. Indirect estimates of the dust temperature, T_d, in SMGs were obtained by measuring the flux at individual rest-frame far-IR (i.e., observed 850 μm) and radio (i.e., 1.4 GHz) wavelengths, and assuming that the local correlation between far-IR and radio luminosities applies (Condon 1992). Based on the ratio between 850 μm flux and inferred total far-IR luminosity, T_d can be inferred, assuming that the dust emission follows a single-temperature modified blackbody spectrum of the form $S_\nu \propto \frac{\nu^{3+\beta}}{\exp(h\nu/kT_d)-1}$, with the emissivity, β, set to a value of 1.5. Chapman et al. (2005) use such a method to characterize their sample of 73 SMGs with spectroscopic redshifts at a median redshift of $z = 2.2$. For this sample, the median inferred dust temperature is $T_d = 36 \pm 7$ K, ~ 5 K cooler than local ULIRGs with similar IR luminosities. In order to constrain the dust temperature more directly, photometric measurements at multiple rest-frame far-IR wavelengths are required, and the observations be-

tween *Spitzer*/MIPS and SCUBA/850 μm wavelengths have until recently been limited. These include Caltech Submillimeter Observatory (CSO) Submillimeter High Angular Resolution Camera (SHARC-2) observations at 350 μm from Kovács et al. (2006) and Coppin et al. (2008) for a total of $\sim$ 30 SMGs with previous 850μm detections. In these studies the additional far-IR SED point suggests a median $T_d = 30 - 35$ K, consistent with the earlier, indirect estimate of $T_d = 36$ K for SMGs. Furthermore, the total far-IR luminosities of SMGs in these samples are better constrained and typically $L_{FIR} \sim$ few $\times 10^{12} L_{\odot}$, with dust masses $M_{dust} \sim 10^9 M_{\odot}$, significantly larger than those observed in local starburst galaxies (Coppin et al. 2008).

New *Herschel* observations at 100 and 160μm with PACS and at 250, 350, and 500μm with the Spectral and Photometric Imaging Receiver (SPIRE) have recently provided significantly more refined estimates of dust temperatures in high-redshift ULIRGs, and revealed a temperature diversity hinted at by earlier, indirect studies (Casey et al. 2009, Chapman et al. 2004). Combining data in the three SPIRE channels with 850μm SCUBA measurements, Chapman et al. (2010) find a median of $T_d = 34 \pm 5$ K for a sample of 31 SMGs and a hotter median $T_d = 41 \pm 5$ K for 37 radio-selected ULIRGs with fainter submillimeter fluxes (where the errors represent the standard deviations of the samples, not of the median values). These samples are characterized by median far-IR luminosities of $L_{IR} = 7.1 \times 10^{12} L_{\odot}$ and $3.8 \times 10^{12} L_{\odot}$, respectively. Such large luminosities were inferred previously on the basis of much more limited rest-frame far-IR data, with large uncertainties on the total luminosity due to its strong dependence on assumed dust temperature. The constraints on the far-IR SED shape now offer a much more robust indication of the dust luminosity and temperature.

Magdis et al. (2010b) focus on combined PACS and SPIRE observations for a sample of star-forming MIPS 24μm-selected ULIRGs at $z \sim 2$, finding a broad range of dust temperatures spanning from $25 \leq T_d \leq 65$ K, with a median of $T_d = 42$ K, and a range of IR luminosities of $1.7 \times 10^{12} L_{\odot} \leq L_{IR} \leq 8.7 \times 10^{12} L_{\odot}$. In particular, and as emphasized previously by Chapman et al. (2004), it is shown that ULIRGs with hotter dust temperatures and fainter submillimeter fluxes at $850 - 1200\mu$m would be missed in current ground-based surveys of SMGs, given their sensitivity limits at $\sim$ 1mm. Therefore, ground-based surveys for $z > 2$ ULIRGs selected on the basis of 850μm fluxes may be biased towards the coolest of the most luminous galaxies. The origin of the diversity in dust temperatures among these most luminous systems is an open question.

While the far-IR SED offers constraints on the thermal properties and total luminosities of the most luminous galaxies at $z > 2$, the mid-IR spectral range reveals the nature of their smaller dust grains and PAH molecules. Furthermore, a fundamental issue regarding ULIRGs at high redshift concerns the nature of the sources heating the dust that emits such copious amounts of far-IR radiation. The two basic alternatives are star-formation or AGN activity. While rest-frame UV and optical spectra (Chapman et al. 2005, Swinbank et al. 2004) and X-ray observations (Alexander et al. 2005) of SMGs indicate evidence for AGN activity in these systems, it is challenging to assess the bolometric importance of the AGNs from these data. The rest-frame mid-IR spectral region, from $\sim 5 - 15\mu$m, offers strong discriminatory power between star-formation and AGN activity, and constraints on the relative contributions of each to the bolometric luminosity of high-redshift ULIRGs. The energetics of the radiation field are determined by the prominence of PAH emission features at 6.2, 7.7, 8.6, and 11.3μm, relative

to the strength of an underlying power-law continuum from hot dust and silicate dust absorption at 9.7μm. The PAH emission is primarily tied to star formation, whereas the hot dust continuum is associated with AGN activity. The strength of silicate absorption potentially indicates the importance of a buried nuclear component (Pope et al. 2008, Sajina et al. 2007).

The IRS instrument onboard *Spitzer* has proven critical for untangling the processes powering the dust emission in ULIRGs at $z \sim 2$. Strikingly, the mid-IR spectra of the majority of SMGs exhibit strong PAH emission features (Menéndez-Delmestre et al. 2009, Pope et al. 2008), indicating the dominance of star-formation over AGN activity in these systems. While many SMGs have X-ray properties suggesting the presence of an AGN, this component does not appear to be energetically dominant in terms of the bolometric luminosity, typically contributing $\leq 30\%$ of the luminosity in the mid-IR (Menéndez-Delmestre et al. 2009, Pope et al. 2008). Only 4 out of the 24 sources presented in Menéndez-Delmestre et al. (2009 and 2 out of 13 of those described in Pope et al. (2008), have mid-IR spectra dominated by a power-law continuum, and the composite spectra for both samples exhibit pronounced PAH features. On the other hand, the $z \sim 2$ 24μm-selected ULIRGs analyzed by Sajina et al. (2007) are more heterogeneous in the mid-IR. The majority ($\sim 75\%$) of these sources have mid-IR spectra dominated by a power-law continuum and therefore AGN activity. At the same time, more than half of these power-law sources have PAH emission features as well, indicating contributions from both AGN and star-formation processes. The minority ($\sim 25\%$) of PAH-dominated sources also indicate evidence for AGN activity in the form of hot dust continuum. Furthermore, the significant strength of 9.7μm silicate absorption in $\sim 25\%$ of the sample indicates the presence of an obscured,

compact nuclear component.

Figure 14, from Pope et al. (2008), illustrates the diversity among high-redshift ULIRG mid-IR spectra, including the PAH-dominated flavor common among SMGs and in a minority of 24μm-selected ULIRGs, and the power-law dominated spectra common in 24μm-selected ULIRGs, with different amounts of silicate absorption. While SMGs and 24μm-selected ULIRGs appear to have similar bolometric luminosities, AGNs appear to play a more significant role in the 24μm-selected ULIRGs, which also have hotter dust temperatures. These differences have been interpreted in terms of an evolutionary scenario, in which SMGs and 24μm-selected ULIRGs represent, respectively, earlier and later stages of a gas-rich, major merger event (Pope et al. 2008, Yan et al. 2010). Through the progression of these stages, obscured nuclear AGN activity grows in importance as the system evolves into an unobscured QSO, and, eventually, a massive elliptical galaxy. While this proposed scenario is intriguing, additional constraints on the number densities, stellar mass and gas content of these various high-redshift samples is necessary to establish robust connections between them (Yan et al. 2010).

5.3 Molecular Gas Content

For a complete characterization of the process of star formation at high redshift, observations of the molecular phase of the ISM are critical. Stars form directly from this dense interstellar phase, which dominates the cool gas content of the most actively star-forming galaxies (Blitz & Rosolowsky 2006). In the local Universe, the star-formation rate per unit area, Σ_{SFR}, is directly related to the total gas surface density, Σ_{gas}, according to the empirical Schmidt Law, $\Sigma_{SFR} \propto \Sigma_{gas}^{N}$, with observational determinations of N ranging from $0.9 - 1.7$ (Kennicutt 1998).

Tracing this relationship at high redshift is key to understanding how gas is converted into stars during the epoch of peak star formation. Furthermore, the star-formation rate and gas content can be related to characterize the efficiency of star formation, as well as the timescale on which gas will be depleted. With short (compared to the Hubble time) gas depletion timescales, star formation can only be sustained by the ongoing accretion of gas from the IGM. The relationship between star formation and the available gas reservoir, in terms of its mass, baryonic mass fraction, and spatial extent, therefore offers crucial inputs into models of galaxy formation, which must include a proper description of the balance between gas accretion, the conversion of gas into stars, and the energetic feedback related to the process of star formation.

In the local Universe, rotational transitions of carbon monoxide (CO) serve as excellent tracers of molecular hydrogen gas (Young & Scoville 1991). These same transitions are used to trace the molecular gas content of high-redshift galaxies, using millimeter-wave and radio telescopes. The first such observations were of extreme sources with known ultraluminous far-IR luminosities, such as QSOs and SMGs, and were suggestive of large amounts of dust and gas (Genzel et al. 2003, Omont et al. 1996). Recently, however, CO detections have been achieved for less extreme systems, well into the LIRG regime and falling on the correlation between SFR and M_{star} that appears to describe more quiescently star-forming galaxies over the range $10 M_{\odot}\mathrm{yr}^{-1} \leq SFR \leq\sim$ few $\times\ 100 M_{\odot}\mathrm{yr}^{-1}$ (Daddi et al. 2007, Tacconi et al. 2008). For observations of CO at high redshift, the IRAM Plateau de Bure Interferometer (PdBI) has played a dominant role, tuned to detecting various upper-level transitions [e.g. CO(2-1), CO(3-2), CO(4-3), and so on] in the millimeter range of the spectrum. Very recently, longer-wavelength ob-

servations carried out at the Expanded Very Large Array (EVLA) and Green Bank Telescope (GBT) have been tuned to the ground-state CO(1-0) transition, which is more directly tied to the molecular gas mass (Harris et al. 2010, Ivison et al. 2011).

In order to infer the mass of molecular gas, M_{gas}, associated with detected CO emission, there are two major sources of systematic uncertainty. One is in the conversion factor between CO(1-0) emission luminosity and M_{gas}. The second results from the fact that, for the most part, high-redshift CO observations have been of upper-level J transitions, whereas the CO-to-H_2 conversion factor is calibrated for the CO(1-0) transition. The ratios between upper-level and ground-state J transitions depend on the excitation and physical conditions in the molecular gas, and incorrect assumptions about these conditions will result in a bias in the inferred CO(1-0) luminosity. In some cases, higher-J transitions, which are sensitive to warmer and denser regions, may even offer an incorrect representation of the spatial distribution of the full molecular gas reservoir (Ivison et al. 2011).

As for the CO-to-H_2 conversion factor, α, it has been calibrated in the Milky Way with a value of $\alpha_{MW} \sim 4 - 5$, in units of $M_{\odot}(K \text{ km s}^{-1} \text{ pc}^2)^{-1}$. This value is very close to the theoretical expectation based on the assumption that CO line emission is produced in discrete, virialized clouds obeying scaling relations among their masses, sizes, and linewidths (Young & Scoville 1991). On the other hand, in galactic nuclei and local starburst galaxies, different dynamical and geometrical conditions apply to the molecular gas, which may reside in a smoother, diskier configuration whose motions are additionally affected by the gravitational potential from stars. These differences result in a lower conversion factor for starbursts of $\alpha = 0.8 - 1.6$ (Tacconi et al. 2008). For observations of high-redshift SMGs,

the starburst conversion factor has been adopted (Tacconi et al. 2008, 2006). In fact, using the higher, Milky Way conversion factor would result in baryonic (gas plus stellar) masses in excess of the measured dynamical masses. On the other hand, for the lower-luminosity LIRGs (both UV-selected and BzK sources), a Milky Way type conversion factor is favored on the basis of similar dynamical arguments (Daddi et al. 2010) and the idea that CO emission in these LIRGs arises in virialized clouds with densities similar to those observed in local quiescent disk galaxies (Tacconi et al. 2008).

We now consider the excitation of the molecular gas, which will affect the conversion between higher-J transitions and CO(1-0). While the CO levels in SMGs appear to be thermally populated up to $J \geq 3$, simultaneous observations of CO(1-0) (VLA), and CO(2-1), and CO(3-2) (PdBI) transitions in a BzK LIRG at $z \sim 1.5$ suggests that the CO(3-2) level is significantly subthermally excited, similar to what is observed in the Milky Way and other local disk galaxies (Dannerbauer et al. 2009). These low-excitation physical conditions require a larger conversion factor from CO(3-2) to CO(1-0), and therefore, a larger inferred molecular gas mass for a given CO(3-2) line luminosity.

CO observations of both ULIRGs and LIRGs at $z \sim 2$ have yielded many important insights into the nature of star formation in different regimes of total galaxy luminosity. Before even considering inferred molecular gas masses, it is worth emphasizing the relationship between far-IR luminosity, L_{FIR}, and CO luminosity, L_{CO}. As shown in Figure 15, Genzel et al. (2010) have assembled measurements of local star-forming galaxies (both quiescent and merging systems), as well as $z \sim 1.5 - 2.0$ UV-selected ("BX") and BzK systems and (more IR-luminous) SMGs. Most strikingly (and also pointed out by Daddi et al. (2010)),

at a fixed L_{CO}, high-redshift SMGs appear to produce $4 - 10$ times more far-IR luminosity than their UV-selected and BzK counterparts, which cannot simply be attributed to enhanced AGN activity in SMGs. This trend mirrors the one observed between local mergers and more quiescently star-forming galaxies.

In terms of star-formation rate and molecular gas surface densities, SMGs are characterized by significantly higher Σ_{SFR} at a given Σ_{gas}. The UV-selected and BzK galaxies follow relations between Σ_{SFR} and Σ_{gas} that are similar to the one observed among quiescently star-forming galaxies in the local Universe, with a slope of $N = 1.1 - 1.2$ (Genzel et al. 2010). SMGs follow an analogous relation but with a higher overall normalization, perhaps reflective of their shorter dynamical timescales (Genzel et al. 2010), and also of processes that increase the efficiency of star formation in the turbulent, merger-driven environment that may be common in SMGs (Engel et al. 2010). More speculatively, a top-heavy IMF in SMGs may produce more far-IR luminosity for a given mass of stars formed. However, the evidence for IMF variations at high-redshift is only indirect at this point, and not specific to SMGs (Davé 2008, van Dokkum 2008). At the same time, Ivison et al. (2011) offer a potential caveat regarding the inferred bimodality of star-formation efficiencies among SMGs and other, more quiescent $z \sim 2$ systems. In so far as the L_{CO} values are based on a range of CO transitions, the conversion of these to CO(1-0) relies on a proper characterization of the gas excitation conditions. Larger samples of $z \sim 2$ star-forming galaxies with uniform CO(1-0) measurements will be crucial for characterizing the diversity (and actual bimodality) among star-formation efficiencies in high-redshift star-forming systems.

The inferred molecular gas reservoirs in UV-selected and BzK galaxies are

extended on scales of several kpc, with typical masses of $0.5 - 1.0 \times 10^{11} M_{\odot}$ (Daddi et al. 2010, Tacconi et al. 2010). These correspond to median gas fractions of 0.44 and 0.57, respectively, for the 10 UV-selected and 6 BzK galaxies, and typical gas depletion timescales of ~ 0.5 Gyr (Genzel et al. 2010). The typical size of the molecular gas distribution is smaller (half-light radii of $\sim 2-3$ kpc) in SMGs, and, while the molecular gas masses and fractions are similar on average, the apparent gas depletion scales are a factor of several shorter than for the UV-selected and BzK galaxies, due to the higher star-formation rates. With the Atacama Large Millimeter Array (ALMA) it will be possible to extend these studies down to fainter luminosities and characterize the gas reservoirs of more typical systems at $z > 2$ that make up the bulk of the star formation at those early epochs.

5.4 Metal Content

While molecular gas provides the material out of which stars form, heavy elements constitute an important product of star formation, returned to the ISM by supernova explosions and stellar winds. As such, the metal content of galaxies reflects the past integral of star formation, modified by the effects of gas inflow (i.e. gas accretion) and outflow (i.e. feedback from star formation or black-hole accretion). The relative abundances of different chemical elements also provides clues about the past history of star formation, in so far as so-called α elements (e.g., O, S, Si, Mg) are produced primarily in Type II supernovae events, on short timescales (~ 10 Myr), while Fe-peak elements (e.g., Fe, Mn, Ni) are produced primarily in Type Ia supernovae over longer timescales (~ 1 Gyr). The metal content of galaxies is especially meaningful when considered in concert with

their stellar and gas masses, since the relationships among these quantities – and deviations from "closed-box" expectations provide constraints on the nature of large-scale gas flows (in both directions).

There are many different methods for measuring the metallicities of galaxies at high redshift, probing both their stellar and gaseous components using rest-frame UV and optical spectroscopic features. Stellar metallicity is measured from absorption lines, while the metal content of the interstellar gas can be gauged from either absorption lines arising in the neutral and ionized ISM, or emission features originating in H II regions.

In general, the continuum S/N and spectral resolution obtained for the rest-frame UV and optical spectra of typical $z \geq 2$ galaxies are not sufficient for robust absorption-line metallicity measurements in individual objects (even using $8 - 10$-meter class telescopes). The rest-frame UV spectra of star-forming galaxies include a host of interstellar features arising from neutral hydrogen and both neutral and ionized metal species, but only the strongest, highly-saturated interstellar absorption lines are detected on an individual-object basis within high-redshift samples (Shapley et al. 2003). These saturated features are not useful for metallicity estimates. In exceptional cases of the spectra of strongly gravitationally-lensed objects, for which both the continuum S/N and resolution are at least an order of magnitude better than average, weak, unsaturated interstellar metal absorption features are detected and can be used for interstellar metallicity estimates. Pettini et al. (2002) measure weak features from α, Fe-peak, and intermediate elements (i.e. nitrogen) in the spectrum of the gravitationally-lensed $z = 2.73$ galaxy, cB58 (see Section 5.1), to infer an actual interstellar abundance pattern. Based on the relative enhancement of α to both

Fe-peak elements and nitrogen, Pettini et al. (2002) estimate a "young" age for cB58, of less than ~ 300 Myr, the timescale for nitrogen enrichment – an unusual case of a *chemical* constraint on the past history of star formation.

Rest-frame UV stellar absorption features from both the photospheric and wind features of hot stars can in principle be used to infer stellar metallicity. Rix et al. (2004) develop calibrations for metal-sensitive stellar photospheric absorption indices at 1370, 1425, and 1978 Å. These have been applied to a small number of individual lensed and unlensed star-forming galaxies at $z \sim 2-3$ (Dessauges-Zavadsky et al. 2010, Quider et al. 2009, Steidel et al. 2004), yielding results consistent for the most part with other metallicity indicators. On the other hand, the 1978 Å Fe III index was measured in a composite spectrum of 75 star-forming galaxies drawn from the GMASS survey (Halliday et al. 2008), in fact suggesting a systematic enhancement of α relative to Fe, when compared with the expected oxygen abundance for objects of the same stellar mass (see below). The shape of the C IVλ1549 P-Cygni wind feature from O and B stars is also sensitive to metallicity (as well as the form of the IMF), and has also been used to estimate stellar metallicity in a few (mainly gravitationally-lensed) $z \sim 2-3$ galaxies with adequate S/N and spectral resolution (Pettini et al. 2000, Quider et al. 2009, 2010). These interstellar and stellar absorption metallicities offer intriguing and detailed probes of small numbers of special high-redshift galaxies, but await the power of future 30-meter-class ground-based telescopes for application to large samples of individual, unlensed objects.

Most results about the metal content of high-redshift galaxies are based on measurements of rest-frame optical emission lines from H II regions. These include combinations of hydrogen recombination lines (Hα, Hβ), and collisionally

excited forbidden lines from heavy elements such as oxygen ([OIII], [OII]), nitrogen ([NII]), and neon ([NeIII]). At $z \geq 2$, rest-frame optical features shift out of the observed optical range and require near-IR spectroscopic observations. The study of rest-frame optical emission from H II regions at high redshift to date has relied on both long-slit and IFU spectroscopy, using instruments such as NIRSPEC and OSIRIS at the Keck Observatory, ISAAC and SINFONI at the VLT, MOIRCS on Subaru, and GNIRS on Gemini-South. Emission lines are primarily used to infer the gas-phase abundance of oxygen (expressed as $12 + \log(\mathrm{O/H})$, where the solar value in these units is 8.66; Asplund et al. 2004), and are based on the relations between particular sets of emission-line ratios and metallicity. These relations have been both empirically calibrated in the local Universe (e.g., Nagao, Maiolino & Marconi 2006; Pettini & Pagel 2004) and theoretically modelled using photoionization codes (e.g., Kewley & Dopita 2002, Tremonti et al. 2004). Two commonly-used indicators of $12 + \log(\mathrm{O/H})$ at high redshift are the so-called $N2$ index, defined as $\log([\mathrm{NII}]\lambda 6584/\mathrm{H}\alpha)$, and $R_{23} \equiv ([\mathrm{OIII}] + [\mathrm{OII}])/\mathrm{H}\beta$. From the ground, R_{23} can be measured within near-IR windows of atmospheric transmision for various redshift intervals between $z \sim 2$ and $z \sim 4$, while $N2$ is only measurable up to $z \sim 2.6$, at which point the thermal background becomes preventively high.

In addition to the significant scatter among different emission-line indicators (differences as large as 0.7 dex in metallicity for the same galaxy) (Kewley & Ellison 2008), another potential source of bias when using locally-calibrated metallicity indicators to interpret the emission-line ratios of high-redshift galaxies is the assumption that the physical conditions in high-redshift galaxy H II regions are similar to those in local galaxies. Small samples of UV-selected galaxies at $z \sim 2$ with

measurements of both [OIII]/Hβ and [NII]/Hα, and/or [OIII]/[OII] and R_{23}, indicate systematic offsets from the excitation sequence of low-redshift galaxies (Erb et al. 2006a, Hainline et al. 2009). These differences may be indicative of a systematically higher ionization parameter and/or electron density, or harder ionizing radiation spectrum, with correspondingly different translations between empirical line ratios and physical metallicities. Larger samples of objects at $z \sim 2$ with such measurements will be required to determine the origin of these apparent offsets, relative to local star-forming galaxies.

At this point, $N2$ measurements have been obtained for a wide variety of $z \sim 2$ sources, numbering ~ 200 and ranging from UV- and near-IR selected galaxies (e.g., Erb et al. 2006a, Hayashi et al. 2009, Kriek et al. 2007, Shapley et al. 2004, Yoshikawa et al. 2010) to SMGs (Swinbank et al. 2004). The sample of objects with emission-line metallicity measurements at $z \geq 3$ is much smaller (Maiolino et al. 2008, Mannucci et al. 2009, Pettini et al. 2001), with metallicities based on R_{23} or other combinations of oxygen, [NeIII], and Balmer lines for ~ 30 objects.

The measurement of galaxy metallicities along with stellar masses allows for the construction of the galaxy mass-metallicity (or M_{star}-Z) relation. This relationship has been studied in the local Universe for $> 50,000$ galaxies with SDSS (Tremonti et al. 2004), and used as a tool to constrain the importance of inflows and outflows as a function of galaxy mass. Another necessary component for this type of analysis is an estimate of the gas mass, which enables a calculation of the metallicity as a function of gas fraction, or, equivalently, the effective yield, y_{eff}. Given the small sample of galaxies with direct atomic and/or molecular gas measurements both locally and at high redshift, gas masses have typically been estimated indirectly on the basis of Σ_{SFR} values and galaxy

sizes, and an assumption that the locally-calibrated relation between Σ_{SFR} and Σ_{gas} applies (Erb et al. 2006a, Tremonti et al. 2004). We note here that the average gas fraction of $\sim 50\%$ inferred by Erb et al. (2006c) for UV-selected star-forming galaxies at $z \sim 2$ agrees well with the CO-based estimate of 44% from Tacconi et al. (2010).

The largest survey of rest-frame optical emission lines at $z \geq 2$ is presented in Erb et al. (2006a), where spectra covering the Hα region were obtained for 87 UV-selected galaxies. As shown in Figure 16, the empirically-measured $N2$ indicator increases monotonically in bins of increasing stellar mass, corresponding to an increase in $12+\log(\mathrm{O/H})$. At a given stellar mass, Erb et al. (2006a) find that $z \sim 2$ galaxies are 0.3 dex lower in metallicity than the local galaxies studied in Tremonti et al. (2004). Based on indirect estimates of gas masses and gas fractions, these authors compare their observations with simple chemical evolution models. The shallow slope of the $z \sim 2$ $M_{star} - Z$ and gas-fraction$-Z$ relations are then used to demonstrate the importance of galaxy-scale winds with mass-outflow rates roughly equal to the star-formation rate (Erb 2008). The observed $M_{star} - Z$ slope at $z \sim 2$ has been viewed as evidence in favor of a "momentum-driven" feedback recipe in the simulations of Finlator & Davé (2008), however we caution against placing too much significance on the precise observed value of this slope, given the known limitations of the $N2$ indicator (which saturates at roughly solar metallicity).

Maiolino et al. (2008) construct the $M_{star} - Z$ relation for 9 galaxies at $z \sim 3.5$, showing that, at fixed stellar mass, galaxies at $z \sim 3.5$ are 0.4 dex lower in $12 + \log(\mathrm{O/H})$ than at $z \sim 2$. Mannucci et al. (2010) explain the observed evolution of the $M_{star} - Z$ relation up to $z \sim 2.5$ in terms of galaxies populating

a more general $M_{star} - Z - SFR$ relation, with no redshift evolution. According to this "Fundamental Metallicity Relation" (FMR; Mannucci et al. 2010), galaxies at fixed stellar mass but higher star-formation rate will have lower metallicity, resulting from the interplay between infalling IGM gas and outflowing enriched material. The rapid apparent evolution in the $M_{star} - Z$ relation beyond $z \sim 2.5$ requires some evolution in the FMR, yet the sample of galaxies at these redshifts with metallicity measurements is too small to draw definitive conclusions.

In order to use the $M_{star} - Z$ relation to constrain models of gas inflow and outflow in star-forming galaxies at $z \sim 2 - 4$, significantly larger (i.e. at least an order of magnitude) samples of galaxies with metallicity measurements are required, which are complete down to a given stellar mass or star-formation rate. Furthermore, constructing the relations between metal and baryonic (stellar and gas) content for galaxies with direct estimates of molecular gas content will provide more robust estimates of the metallicity as a function of gas fraction. Spatially-resolved estimates of chemical abundance gradients will offer additional constraints on the inflow and outflow of gas, and the build-up of the galaxy stellar population. These have been now reported for a handful of objects, with conflicting results about the sign of the radial gradient (Cresci et al. 2010, Jones et al. 2010). Deeper data for larger samples will be required to settle this discrepancy. The next generation of near-IR multi-slit spectrographs and IFUs should easily enable these observations.

6 STRUCTURAL AND DYNAMICAL PROPERTIES

The diversity among galaxy structural and dynamical parameters in the local Universe reflects a range of mass assembly histories, and the relative importance

of mergers and smoother mass accretion. Furthermore, properties such as size, concentration, mass-surface density, and velocity dispersion are correlated with indicators of the nature of stellar populations, such as luminosity, stellar mass, and specific star-formation rate (Kauffmann et al. 2003b, Shen et al. 2003). Reproducing the observed connections among these galaxy structural and stellar properties and their redshift evolution within a unified framework constitutes a crucial test for models of galaxy formation. In this section we review recent results about the structural and dynamical properties of high-redshift galaxies. Due to the small apparent sizes of most $z \geq 2$ galaxies ($\lesssim 1$"), *HST* imaging and ground-based IFU maps assisted by adaptive optics (AO) are both critical for resolving overall shapes and ∼kpc-scale fine structure. Interferometric observations of CO line emission have also provided valuable insight into the dynamical properties of the most extreme sources at high-redshift, such as SMGs. While high-resolution imaging and dynamical maps are each powerful probes individually, combining these two methods of observations (Förster Schreiber et al. 2011) will provide the deepest insights into the nature of the galaxy assembly process at high redshift.

6.1 Structural Properties

In general, the morphologies of galaxies at $z \geq 2$ are characterized by two important differences with respect to those of local galaxies. First, the traditional Hubble sequence of regular spirals and elliptical galaxies has not settled into place by $z \sim 2$, and a much higher frequency of clumpy, irregular morphologies is observed among star-forming systems (Lotz et al. 2006, Ravindranath et al. 2006). Second, both star-forming and quiescent galaxies are more compact at fixed stel-

lar mass or rest-frame optical luminosity (Buitrago et al. 2008). In order to characterize the structural properties of high-redshift galaxies, both parametric and non-parametric methods have been employed. In the former, model Sérsic profiles are fit to the data, yielding best-fit values for n, the Sérsic power-law index, and r_e, the effective radius, within which half the galaxy luminosity is emitted. Sérsic profile fits work best for regular, axially-symmetric morphologies with well-defined centers, so, in order to address the clumpy, irregular structures observed among high-redshift systems non-parametric statistics such as the *Gini*, M_{20}, $Multiplicity$, and CAS coefficients have been developed (Abraham, van den Bergh & Nair 2003; Conselice, Chapman & Windhorst 2003; Law et al. 2007; Lotz et al. 2006; Lotz, Primack & Madau 2004) to characterize their concentrations, asymmetries, and clumpiness (i.e. deviations from maximally compact configurations).

The first high-redshift galaxies to be observed with *HST* were UV-selected galaxies at $z \sim 3$ (Giavalisco, Steidel & Macchetto 1996; Lowenthal et al. 1997). The irregular morphologies of these systems, often composed of multiple compact components and/or irregular nebulosity, were first attributed to the fact that the Wide Field Planetary Camera 2 (WFPC2) and ACS are optical imagers, probing rest-frame UV wavelengths at $z \sim 3$ – a so-called "morphological k-correction." In principle, measurements at these wavelengths might be sensitive to only the most active regions of star formation rather than the bulk of the stellar mass, and potentially affected by patchy dust extinction. However, in practice, rest-frame optical imaging with the Near Infrared Camera and Multi-Object Spectrometer (NICMOS), using both NIC2 and NIC3 cameras (Dickinson 2000, Förster Schreiber et al. 2011, Kriek et al. 2009, Papovich et al. 2005) and the Wide

Field Camera 3 (WFC3) (Overzier et al. 2010) has demonstrated that actively star-forming galaxies at $z \sim 2 - 3$ have very similar rest-frame UV and optical morphologies. On the other hand, among the most massive, evolved systems at $z \sim 2-3$, there is evidence for more centrally-concentrated, regular morphologies at rest-frame optical wavelengths, compared with the structure observed in the rest-frame UV (Cameron et al. 2010, Toft et al. 2005). With the recent installation of WFC3, it will now be possible to measure rest-frame optical morphologies for statistical samples of $z \sim 2 - 3$ objects at ∼kpc-scale resolution. The performance of the IR channel of WFC3 is superior to the NICMOS NIC3 camera in terms of resolution, sensitivity, and area.

While the traditional Hubble sequence of disk and elliptical is not in place by $z \sim 2$, *HST* imaging has revealed a large diversity of structural parameters among galaxies at $z \sim 2-3$, which correlate with their stellar populations in analogy with the trends observed in the local Universe. Based on NICMOS/NIC3 F160W imaging, Zirm et al. (2007) and Toft et al. (2007) show that quiescent, high-redshift $z \sim 2$ galaxies have systematically smaller sizes and higher stellar-mass surface densities than actively star-forming systems of the same stellar mass. Franx et al. (2008), Toft et al. (2009), and Williams et al. (2010) use deep, ground-based K-band images to demonstrate the same trend. Based on higher-resolution NICMOS/NIC2 F160W imaging for a sample of spectroscopically-confirmed K-selected massive galaxies at $z \sim 2$, Kriek et al. (2009) presents a comparison of the Sérsic profile fits for the quiescent and emission-line objects. As shown in Figure 17, galaxies with redder rest-frame $U - B$ colors, lower specific star-formation rates, and SEDs indicative of more evolved stellar populations, are characterized by smaller r_e and more concentrated surface-brightness

profiles (larger n). This figure also shows the clumpy rest-frame optical morphologies of the massive, blue galaxies. Objects whose emission-line ratios actually suggest AGN activity show structural properties and SEDs that are similar to those of the quiescent galaxies. Förster Schreiber et al. (2011) find even larger sizes and shallower profiles in NIC2 images of the six clumpy UV-selected galaxies in their sample, which also have higher specific star-formation rates. Also similar to the trends observed in the local Universe, Franx et al. (2008) and Förster Schreiber et al. (2011) find a correlation between stellar mass surface density and specific star-formation rate, such that galaxies with higher stellar mass densities have lower specific star-formation rates (Kauffmann et al. 2003b).

We now highlight two important observed morphological phenomena, which have sparked much interest from the theoretical community. One is the nature of the clumpy morphology and "clumps" in actively star-forming galaxies at $z \geq 2$. The other is the incredibly compact nature of massive, quiescent galaxies at high redshift, and their connection to today's massive, early-type galaxies.

6.1.1 CLUMPY MORPHOLOGIES IN STAR-FORMING SYSTEMS

While it is possible to model the rest-frame UV and optical morphologies of $z \geq 2$ galaxies using smooth Sérsic profiles, significant residuals result due to the presence of non-axisymmetric surface-brightness fluctuations. These "clumps" have been fairly ubiquitously observed among the rest-frame UV and optical morphologies of distant galaxies (Cowie, Hu & Songaila 1995; Elmegreen & Elmegreen 2005; Law et al. 2007; Lotz, Primack & Madau 2004), and are visible among the actively star-forming galaxies in Figure 17. Clumps are characterized by typical sizes of $\sim$ 1 kpc, and make up as much as $\sim$ 40% of the rest-frame UV light distribution (Elmegreen et al. 2009). While clumpy, irregular structure was first

explained as the natural outcome of the increased prevalence of major merger events at high redshift (e.g., Conselice, Chapman & Windhorst 2003), various lines of evidence suggest that other factors may contribute to this phenomenon.

First, Law et al. (2007) demonstrated a decoupling between the *Gini* coefficient (and any other rest-frame UV non-parametric morphological statistic) and star-formation rate. If clumpy morphology was connected with the incidence of a major merger, the *Gini* coefficient, sensitive to non-uniformities in the light distribution, should display some correlation with the parameters describing galaxy stellar populations. Swinbank et al. (2010) also highlight the fact that the distribution of rest-frame UV and optical morphologies of SMGs (plausibly the sites of major merger events; Engel et al. 2010, Swinbank et al. 2006) were statistically indistinguishable from those of UV-selected star-forming galaxies, which are significantly more quiescent in terms of bolometric luminosity and star-formation rate. Furthermore, the clumpy phenomenon is far too common among star-forming galaxies at $z \sim 2 - 3$ to be accounted for quantitatively by the predicted rate of major merger events in, e.g., the Millennium Simulation (Conroy et al. 2008, Genel et al. 2008). Finally, as described below in Section 6.2.1, clumpy structures are commonly observed in galaxies with ordered velocity fields indicative of rotating disks – demonstrating that a major merger is not necessarily the cause for clumps. Minor-merger interactions and instabilities in gas-rich, turbulent disks are more likely alternatives for the formation of clumps (Bournaud & Elmegreen 2009; Dekel, Sari & Ceverino 2009; Genzel et al. 2008).

6.1.2 THE COMPACTNESS OF QUIESCENT GALAXIES At fixed stellar mass, both star-forming and quiescent galaxies have smaller radii at higher redshift. The evolution in the $M_{star} - r_e$ relationship is especially dramatic

for quiescent systems. As noted by many authors (e.g., Buitrago et al. 2008, Cimatti et al. 2008, Daddi et al. 2005, Damjanov et al. 2009, Toft et al. 2007, Trujillo et al. van Dokkum et al. 2008) using rest-frame UV and optical *HST* imaging and ground-based data, $z \sim 1.5 - 2$ quiescent galaxies have radii that are $\sim 2 - 5$ times smaller than those of local early-type galaxies of the same stellar mass. For example, $z \sim 2$ quiescent galaxies with $M_{star} \sim 10^{11} M_{\odot}$ are measured to have $r_e \sim 1$ kpc (van Dokkum et al. 2008), compared with ~ 3 kpc in local early-type galaxies of the same mass (Damjanov et al. 2009). The observed differences in size correspond to factors of $\sim 10 - 100$ in physical density! Furthermore, Taylor et al. (2010) demonstrate the extreme scarcity of such compact, early-type systems in the local Universe. The resulting challenge from these discoveries consists of relating high-redshift massive, compact quiescent galaxies to their low-redshift counterparts – since structural evolution is required for the distant objects to resemble the current ones. Scenarios considered to explain the observed evolution in size include the effects of major and minor dissipationless mergers (Hopkins et al. 2010, 2009; Naab, Johansson & Ostriker 2009) as well as energetic feedback from an accreting black hole (Fan et al. 2008).

Many important caveats have been raised about the observations of apparent compactness among quiescent galaxies. These include (*a*) the possibility of not accounting for extended low-surface brightness emission which would tend to increase the inferred radius; (*b*) using in some cases rest-frame UV rather than rest-frame optical imaging; (*c*) radially-dependent stellar M/L ratios that increase outwards, causing an underestimate of the mass at larger radii; (*d*) a reliance on photometric rather than spectroscopic redshifts; and (*e*) uncertainties in stellar population models used to estimate stellar masses (van Dokkum et al. 2008,

2010). Most of these concerns have been addressed, using samples with spectroscopic redshifts and deeper surface-brightness limits. Additionally, crude dynamical information has been obtained from stacked and individual spectra of compact, quiescent galaxies, based on an estimate of velocity dispersion from stellar absorption lines (Cappellari et al. 2009; Cenarro & Trujillo 2009; van Dokkum, Kriek & Franx 2009). The estimated velocity dispersions appear to confirm the large masses inferred from stellar population modeling. Furthermore, results at $z \sim 1$ based on a comparison of radii and *dynamical* mass estimates for 50 galaxies suggest a factor of 2 evolution in size at fixed dynamical mass, consistent with the evolutionary trend observed to $z \sim 2$ based on stellar masses (van der Wel et al. 2008).

Employing a complementary technique, van Dokkum et al. (2010) stack the ground-based near-IR surface-brightness profiles for rare, massive galaxies of constant number density in five redshift bins between $z = 2.0$ and $z = 0.1$, such that the higher-redshift objects can plausibly represent the progenitors of the objects at lower redshift. The observed evolution in these stacked surface brightness profiles shows that the mass within an inner region of $r = 5$ kpc remains roughly constant, while the mass at larger radii builds up smoothly as a function of decreasing redshift. This result suggests the importance of minor merger events in the growth of massive, elliptical galaxies (Hopkins et al. 2009; Naab, Johansson & Ostriker 2009), and that the structure of elliptical galaxies is not self-similar as a function of redshift. Based on deep near-IR spectroscopy with upcoming instruments on the ground and in space, statistical samples of dynamical mass estimates for passive galaxies at $z \geq 2$ will be crucial for even more robustly distinguishing among evolutionary scenarios.

6.2 Dynamical Properties

Dynamical studies of high-redshift galaxies have mainly been limited to star-forming objects, using rest-frame optical emission lines from ionized gas or millimeter-wave emission from CO tracing molecular gas. While the sample of existing rest-frame UV spectra for high-redshift galaxies is much larger than either of these other types of dataset (Steidel et al. 2003, 2004), the emission and absorption features typically detected in the rest-frame UV range are broadened by non-virial motions from outflowing gas and radiative transfer effects, and unfortunately do not permit useful dynamical measurements (Pettini et al. 2001, Shapley et al. 2003, Steidel et al. 2010). The first dynamical probes of high-redshift star-forming galaxies consisted of long-slit near-IR spectroscopy of ~ 100 UV-selected galaxies (Erb et al. 2003, 2004, 2006c, Pettini et al. 2001) and CO maps of very small samples of SMGs (Genzel et al. 2003, Neri et al. 2003). Indeed, CO observations can be used not only for estimating molecular gas masses but also for probing the dynamical properties of a galaxy. These early observations revealed a typical Hα or [OIII] emission-line velocity dispersion of $\sigma \sim 100$ km s^{-1} for UV-selected galaxies. Measured linewidths were $\sim 2-3$ times larger in the SMG CO maps, which also showed evidence for complex, multi-component emission-line morphology. A particularly striking result from the long-slit Hα studies of Erb et al. (2006c) consists of the measurement of spatially-resolved, tilted emission-lines, indicative of velocity shear, and, perhaps, rotation – i.e., preliminary evidence for disks at high redshift. Below we summarize some of the latest results from both near-IR IFU and CO dynamical studies of high-redshift galaxies, highlighting many open questions in this rapidly evolving field.

6.2.1 INTEGRAL-FIELD UNIT OBSERVATIONS OF TURBULENT STAR-FORMING GALAXIES

With the advent of both seeing-limited and AO-assisted near-IR IFU spectrographs on Keck, the VLT and Gemini telescopes several years ago, the study of high-redshift galaxy dynamics has advanced considerably. Some striking trends have emerged from a total sample of ~ 100 objects with IFU kinematic observations, which are no longer subject to the spatial-sampling limitations of long-slit spectroscopy taken at a fixed position angle. We focus here on the VLT/SINFONI survey of Förster Schreiber et al. (2009) and the Keck/OSIRIS survey of Law et al. (2009), which represent two of the largest campaigns at $z \geq 2$ using this new observational capability. The "SINS Hα Survey" presented in Förster Schreiber et al. (2009) includes 62 star-forming galaxies at $1.3 \leq z \leq 2.6$ selected in the rest-frame UV, optical, near-IR, and submillimeter. The sample is representative of massive, $M_{star} > 10^{10} M_{\odot}$, star-forming galaxies in this redshift range, with a median stellar mass and star-formation rate of $M_{star} = 3 \times 10^{10} M_{\odot}$ and $SFR = 70\ M_{\odot}\mathrm{yr}^{-1}$, respectively. The sample of Law et al. (2009) includes 12 UV-selected star-forming galaxies at $2.0 \leq z \leq 2.5$ with a median stellar mass and star-formation rate of $M_{star} = 10^{10} M_{\odot}$ and $SFR = 40\ M_{\odot}\mathrm{yr}^{-1}$, respectively. In addition to having lower stellar masses on average, the objects in the Law et al. (2009) sample are also characterized by a smaller median Hα half-light radius than the SINS Hα sample (1.3 versus 3.1 kpc). All OSIRIS observations in Law et al. (2009) are AO-assisted, with an effective PSF of $\sim$ 0.15", corresponding to $\sim$ 1.2 kpc. The majority ($\sim$ 85%) of the SINFONI observations discussed by Förster Schreiber et al. (2009) are seeing-limited, with a typical resolution of $\sim$ 0.6", corresponding to $\sim$ 4.9 kpc; the remainder were observed using either laser- or natural-guide-star AO, with reso-

lutions ranging from $0.17" - 0.41"$, corresponding to $\sim 1.6 - 3.4$ kpc.

These IFU surveys have revealed a wealth of diversity among the dynamical properties of distant star-forming galaxies. The key observables are maps of velocity, velocity dispersion, and line-intensity, which can then be used as inputs to detailed dynamical models, or analyzed in a more empirical sense. Figure 18 demonstrates the range of velocity fields observed in the SINS Hα survey. Roughly 1/3 of these velocity maps show clear gradients and are classified as "rotation-dominated," with corresponding maps of velocity dispersion showing central maxima; roughly another 1/3 qualify as "mergers" as evidenced by kinemetric modeling (Shapiro et al. 2009) or distinct multiple components; finally, 1/3 of the sample are "dispersion-dominated", with no evidence for rotation or shear, but characterized by a significant velocity dispersion. Half of the Law et al. (2009) sample belong to this last category, with no evidence for rotation.

Another basic result consists of the high degree of turbulence observed in the ISM of high-redshift galaxies, along with a small ratio of rotational to random motions. The spatially-resolved velocity dispersion maps indicate local velocity dispersion values ranging from $\sigma_{local} = 30 - 90$ km s^{-1} in the SINS Hα sample and $\sigma_{local} = 60 - 100$ km s^{-1} in the sample of Law et al.. Even in rotation-dominated systems, the velocity dispersion is significant. The median value of v_{rot}/σ is 4.5, which is considerably lower than the values of $\sim 10 - 20$ observed in local spiral galaxies (Förster Schreiber et al. 2009). Of course, in the dispersion-dominated systems, v_{rot}/σ is even smaller (i.e., ≤ 1). The prevalence of rotation and rotation-dominated systems appears to be correlated with stellar mass, with a higher fraction of rotating systems at higher stellar masses. At the same time,

galaxies with small stellar masses and large gas fractions tend to have negligible rotation (Förster Schreiber et al. 2009, Law et al. 2009).

The star-forming galaxies with IFU observations also appear to follow scaling relations between their basic dynamical and stellar properties. Both Bouché et al. (2007) and Förster Schreiber et al. (2009) present a strong correlation between galaxy circular velocity, v_{rot}, and size for galaxies selected in the rest-frame UV, optical, and near-IR. This correlation is indistinguishable from the one describing local disk galaxies (despite the significant differences in v_{rot}/σ), and both UV-selected and BzK galaxies follow it. On the other hand, SMGs occupy a distinct region of $v_{rot}-$size parameter space, with significantly larger velocities and smaller sizes. This difference potentially reflects the lower angular momenta and higher matter densities present in SMGs relative to more quiescently star-forming UV-selected and BzK systems (Bouché et al. 2007). Limiting their analysis to 18 rotation-dominated systems from the SINS Hα sample, Cresci et al. (2009) discover a "Tully-Fisher" correlation between stellar mass and v_{rot}, which has the same slope as the correlation among local disk galaxies, but offset by ~ 0.4 dex towards lower stellar mass at fixed v_{rot}. Furthermore, a comparison of dynamical and stellar masses indicates a strong correlation, but suggests that galaxies must contain significant gas fractions to explain the differences between the two mass estimates. In particular, galaxies with young stellar ages appear to contain larger gas fractions, consistent with the previous, long-slit results of Erb et al. (2006c).

The spatially-resolved Hα maps indicate that clumpy morphologies are a feature of not only continuum surface brightness (Elmegreen & Elmegreen 2005), but also the emission from ionized gas (Förster Schreiber et al. 2009, Genzel et al. 2008). Given that star-forming clumps are present even in galaxies with ordered rota-

tion fields and no evidence of major merging, and that the clumps appear to follow the general velocity field of the larger systems in which they are embedded, it is unlikely that clumps constitute distinct, accreted systems. An alternative explanation for observed clump properties is based on predicting the size and mass-scale on which gas should fragment in a turbulent, high-surface-density disk. Specifically, the high turbulent velocities observed (as described above) lead to an expected Jeans length for fragmentation of ~ 2.5 kpc (Genzel et al. 2008). Folding in the typical observed disk surface densities ($\sim 10^2 M_\odot$ pc^{-2}), Genzel et al. (2008) estimate clump masses of $\sim 10^9 M_\odot$, similar to what is observed. Numerical simulations of turbulent gas-rich disks also appear to produce ∼kpc-scale clumps (Bournaud & Elmegreen 2009). Theoretical arguments (both analytical and numerical) suggest that these clumps may migrate inwards and coalesce to form a bulge on $\sim 0.5 - 1.0$ Gyr timescales (Dekel, Sari & Ceverino 2009; Elmegreen, Bournaud & Elmegreen 2008). On the other hand, feedback from star formation may disrupt the clumps before they reach the center, and they may simply contribute to the overall growth of the disk. The role of clumpy structures in the growth of massive galaxies is an extremely active area of research; new observational results will help to elucidate the origin and fate of the clumps.

Local velocity dispersions of $\sim 50 - 100$ km s^{-1} appear to be a generic property of high-redshift star-forming galaxies at $z \sim 2$. Determining the cause of this large apparent turbulence is an important goal for models of galaxy formation. Proposed scenarios include the conversion of the gravitational potential energy from infalling accreting matter into random kinetic energy or collisions between large clumps as they migrate inwards (see, e.g., Genzel et al. 2011, for

a review of these possibilities). On the other hand, Lehnert et al. (2009) argue that mechanical energy feedback associated with star formation – in the form of stellar winds and supernovae explosions – is the driving force behind the large observed interstellar turbulence. Various authors have compared the surface-density of star-formation Σ_{SFR} with the local velocity dispersion (presumably an indication of the connection between star-formation feedback and interstellar turbulence) and have arrived at different conclusions about what the weak observed correlation (if any) signifies (Förster Schreiber et al. 2009, Genzel et al. 2011, Lehnert et al. 2009). The cause of large turbulent velocities in high-redshift star-forming galaxies clearly remains an open question.

6.2.2 THE NATURE OF SMGS Dynamical information can also be potentially used to investigate the origin of the extreme luminosities among SMGs. Both near-IR IFU maps and CO observations of SMGs have been used in this endeavor. The observed CO profiles are broad (FWHM typically several hundred km s^{-1}) and often double-peaked (Greve et al. 2005). A broad, double-peaked profile can be indicative of either a massive, rotating disk or, alternatively, a merger event. Swinbank et al. (2006) present near-IR IFU observations of 8 SMGs at $1.3 \leq z \leq 2.6$, probing rest-frame optical line emission. At least five of these systems show evidence for two or more distinct dynamical components, suggestive of merging. Based on subarcsecond-resolution CO maps for 12 SMGs at $1.2 \leq z \leq 3.4$, Engel et al. (2010) find evidence in 5 systems for two distinct spatial components, with mass ratios (when possible to determine) closer than $1:3$ – the standard threshold for being considered a major merger. In the remaining systems, morphologies are either disturbed or compact, and Engel et al. (2010) argue that these represent later-stage, coalesced merger events. A significant frac-

tion of SMGs clearly show dynamical evidence for major merging. Whether an alternative scenario of smooth gas infall and minor mergers (e.g., Davé et al. 2010) can explain the luminosities of the remaining sources will require more robust observations of the space densities, and stellar and dynamical masses of SMGs. The extreme matter densities inferred for SMGs (Bouché et al. 2007), their high apparent star-formation efficiencies (Daddi et al. 2010, Genzel et al. 2010), and the deviation of these systems from global scaling relations between star-formation rate and stellar mass (Daddi et al. 2007), all suggest that they constitute very unusual events. It remains an open challenge to relate SMGs to other ULIRGs at the same epochs (e.g., the 24μm-selected objects of Yan et al. 2007), as well plausible descendants among the lower-redshift massive-galaxy population.

7 CONCLUDING REMARKS

Our path has traveled through many different wavelength ranges and observational techniques along the way to characterizing the stars, dust, gas, heavy elements, structure and dynamics of high-redshift galaxies at $2 \leq z \leq 4$. By design, this review has focused primarily on the translation of observed quantities to physical ones, instead of making systematic comparisons with particular theories (although at times, when appropriate, a connection was made). At the same time, the rapid development of observations and their physical interpretation over the previous decade has yielded an important body of data for input into models of galaxy formation (i.e., the diversity of star-formation histories and structures among the highest-mass systems; the connection between stellar mass and star-formation rate; the nature of dust extinction as a function of luminosity; the estimate of star-formation efficiency for LIRGs and ULIRGs;

the mass-metallicity relation as a function of redshift; the compactness of massive, quiescent systems; the high degree of turbulence in the ISM of star-forming galaxies; and so on).

There are some definite limitations in the nature of this review. Indeed, the description of physical properties was often still couched in terms of how the results applied to a specific galaxy sample, assembled using a specific selection technique from among the ones described in Section 2. In order for measurements of galaxy properties to have true discriminating power among galaxy formation models, it is crucial to use samples that are complete with respect to a well-defined property, such as rest-frame optical or near-IR luminosity, stellar mass, dynamical mass, or star-formation rate. The majority of the samples described in this review slice the underlying high-redshift galaxy population in particular ways that add an extra layer of complexity if a comparison with a simulated galaxy population is desired. We advocate the design of future surveys with the type of physical completeness described above in mind. The NEWFIRM Medium-Band Survey (van Dokkum et al. 2009) represents an important step in this direction, but an even deeper survey would be desirable, with both rest-UV and optical spectroscopic follow-up.

Furthermore, we point out that many of the results reported here were (by necessity) based on small samples – these include mid-IR spectra of the most luminous sources, measurements of molecular gas content and dynamics, individual emission and absorption-line metallicity measurements at $z \geq 2$, high-resolution rest-frame optical morphological measurements, and AO-assisted emission-line maps. While these results highlight truly compelling questions, they also await confirmation from samples an order of magnitude larger for a robust comparison

with models.

Also, by necessity, some of the most intriguing results regarding gas, dust, and structural properties are limited to the luminous extreme of the galaxy population. With the steep luminosity functions described in Section 3.1, galaxies with $L \leq 10^{12} L_{\odot}$ comprise the bulk ($\sim 75\%$) of the luminosity and star-formation rate density of the Universe at $z \sim 2$. Even galaxies with $L \leq 10^{11} L_{\odot}$ may contribute $\sim 30 - 35\%$ of the bolometric luminosity density at this redshift (Reddy et al. 2008). We must find ways of extending our physical studies towards fainter luminosities – either by using gravitationally-lensed objects, or the next generation of instruments and telescopes. These faint objects are important, and perhaps more analogous to the galaxies playing a crucial role in the reionization process at $z \geq 6$.

We close by highlighting two important observational challenges, and looking towards the future. First, the direct measurement of gas inflow (accretion) and outflow (star-formation and AGN feedback) received only passing reference during the course of this review. The ubiquity of galaxy-scale outflows among $z \geq 2$ UV-selected galaxies has long been known on the basis of rest-frame UV and optical spectra (Adelberger et al. 2005, 2003, Pettini et al. 2001, Shapley et al. 2003, Steidel et al. 2010, 2004), yet obtaining robust constraints on the physical properties associated with these outflows (e.g., mass outflow rates) remains a challenge (but see, e.g., Steidel et al. 2010). At the same time, there is no obvious connection between these observations and the extremely popular theoretical models of cold gas accretion (e.g., Dekel et al. 2009, Kereš et al. 2009, 2005). An open challenge is to observe a "smoking gun" of gas accretion in high-redshift galaxies. Second, the study of galaxy environments at $z \geq 2$ is a field in its infancy.

While overdensities of LAEs have been identified near luminous radio galaxies (Venemans et al. 2007), and a small number of apparent protoclusters have been discovered serendipitously during the course of high-redshift galaxy spectroscopic surveys (Steidel et al. 1998, 2005), the study of the dependence of galaxy properties on environment at $z \geq 2$ remains largely untapped. Environmental studies will require extensive spectroscopy of mass-complete samples in both overdense and "field" environments, and will have potentially fundamental implications for understanding the origin of local galaxy environmental trends. Finally, we look forward to the truly exciting insights that will be made possible by upcoming facilities, including sensitive multi-object near-IR spectrographs on $8 - 10$-meter class telescopes, ALMA, JWST, and the extremely large ground-based telescopes of the next decade.

Acknowledgments

I would like to thank Katherine Kornei and Gwen Rudie for careful readings of the manuscript, and Naveen Reddy for many stimulating discussions and helpful comments. I would also like to thank the numerous authors who so generously shared their figures for this review, and note that figures previously appearing in *The Astrophysical Journal* have been reproduced by permission of the AAS. Very importantly, my thanks go to Sandy Faber, for giving me the opportunity to review the field of high-redshift galaxy properties, and for her patience and constructive feedback as editor. Finally, I would like to thank my collaborators for useful dialogs over the past decade and more, which have shaped my understanding of this rapidly developing field. AES is a Packard Fellow; financial support from the Packard Foundation is gratefully acknowledged.

References

1. Abazajian KN, Adelman-McCarthy JK, Agüeros MA, Allam SS, Allende Prieto C, et al. 2009. *Ap. J. Suppl.* 182:543–558

2. Abraham RG, Glazebrook K, McCarthy PJ, Crampton D, Murowinski R, et al. 2004. *Astron. J.* 127:2455–2483

3. Abraham RG, van den Bergh S, Nair P. 2003. *Ap. J.* 588:218–229

4. Adelberger KL, Shapley AE, Steidel CC, Pettini M, Erb DK, Reddy NA. 2005. *Ap. J.* 629:636–653

5. Adelberger KL, Steidel CC. 2000. *Ap. J.* 544:218–241

6. Adelberger KL, Steidel CC, Shapley AE, Hunt MP, Erb DK, et al. 2004. *Ap. J.* 607:226–240

7. Adelberger KL, Steidel CC, Shapley AE, Pettini M. 2003. *Ap. J.* 584:45–75

8. Alexander DM, Bauer FE, Chapman SC, Smail I, Blain AW, et al. 2005. *Ap. J.* 632:736–750

9. Asplund M, Grevesse N, Sauval AJ, Allende Prieto C, Kiselman D. 2004. *Astron. Astrophys.* 417:751–768

10. Baker AJ, Lutz D, Genzel R, Tacconi LJ, Lehnert MD. 2001. *Astron. Astrophys.* 372:L37–L40

11. Baldry IK, Glazebrook K, Brinkmann J, Ivezić Ž, Lupton RH, et al. 2004. *Ap. J.* 600:681–694

12. Baldry IK, Glazebrook K, Driver SP. 2008. *MNRAS* 388:945–959

13. Bastian N, Covey KR, Meyer MR. 2010. *Annu. Rev. Astron. Astrophys.* 48:339–389

14. Bell EF, Wolf C, Meisenheimer K, Rix H, Borch A, et al. 2004. *Ap. J.* 608:752–767

15. Blanton MR, Hogg DW, Bahcall NA, Brinkmann J, Britton M, et al. 2003. *Ap. J.* 592:819–838

16. Blanton MR, Moustakas J. 2009. *Annu. Rev. Astron. Astrophys.* 47:159–210

17. Blitz L, Rosolowsky E. 2006. *Ap. J.* 650:933–944

18. Borys C, Smail I, Chapman SC, Blain AW, Alexander DM, Ivison RJ. 2005. *Ap. J.* 635:853–863

19. Bouché N, Cresci G, Davies R, Eisenhauer F, Förster Schreiber NM, et al. 2007. *Ap. J.* 671:303–309

20. Bournaud F, Elmegreen BG. 2009. *Ap. J. Lett.* 694:L158–L161

21. Bouwens RJ, Illingworth GD, Franx M, Chary R, Meurer GR, et al. 2009. *Ap. J.* 705:936–961

22. Bouwens RJ, Illingworth GD, Franx M, Ford H. 2007. *Ap. J.* 670:928–958

23. Bouwens RJ, Illingworth GD, Oesch PA, Stiavelli M, van Dokkum P, et al. 2010. *Ap. J. Lett.* 709:L133–L137

24. Boylan-Kolchin M, Springel V, White SDM, Jenkins A, Lemson G. 2009. *MNRAS* 398:1150–1164

25. Brammer GB, Whitaker KE, van Dokkum PG, Marchesini D, Labbé I, et al. 2009. *Ap. J. Lett.* 706:L173–L177

26. Brinchmann J, Charlot S, White SDM, Tremonti C, Kauffmann G, et al. 2004. *MNRAS* 351:1151–1179

27. Bruzual G, Charlot S. 2003. *MNRAS* 344:1000–1028

28. Buitrago F, Trujillo I, Conselice CJ, Bouwens RJ, Dickinson M, Yan H. 2008. *Ap. J. Lett.* 687:L61–L64

29. Calzetti D. 2001. *Publ. Astron. Soc. Pac.* 113:1449–1485

30. Calzetti D, Armus L, Bohlin RC, Kinney AL, Koornneef J, Storchi-Bergmann T. 2000. *Ap. J.* 533:682–695

31. Cameron E, Carollo CM, Oesch PA, Bouwens RJ, Illingworth GD, et al. 2010. *ArXiv e-prints, (astro-ph/1007.2422)*

32. Cappellari M, di Serego Alighieri S, Cimatti A, Daddi E, Renzini A, et al. 2009. *Ap. J. Lett.* 704:L34–L39

33. Caputi KI, Lagache G, Yan L, Dole H, Bavouzet N, et al. 2007. *Ap. J.* 660:97–116

34. Cardelli JA, Clayton GC, Mathis JS. 1989. *Ap. J.* 345:245–256

35. Casey CM, Chapman SC, Beswick RJ, Biggs AD, Blain AW, et al. 2009. *MNRAS* 399:121–128

36. Cassata P, Cimatti A, Kurk J, Rodighiero G, Pozzetti L, et al. 2008. *Astron. Astrophys.* 483:L39–L42

37. Cenarro AJ, Trujillo I. 2009. *Ap. J. Lett.* 696:L43–L47

38. Ceverino D, Dekel A, Bournaud F. 2010. *MNRAS* 404:2151–2169

39. Chabrier G. 2003. *Publ. Astron. Soc. Pac.* 115:763–795

40. Chapman SC, Blain AW, Ivison RJ, Smail IR. 2003. *Nature* 422:695–698

41. Chapman SC, Blain AW, Smail I, Ivison RJ. 2005. *Ap. J.* 622:772–796

42. Chapman SC, Ivison RJ, Roseboom IG, Auld R, Bock J, et al. 2010. *MNRAS* 409:L13–L18

43. Chapman SC, Smail I, Blain AW, Ivison RJ. 2004. *Ap. J.* 614:671–678

44. Charlot S, Fall SM. 2000. *Ap. J.* 539:718–731

45. Chary R, Elbaz D. 2001. *Ap. J.* 556:562–581

46. Cimatti A, Cassata P, Pozzetti L, Kurk J, Mignoli M, et al. 2008. *Astron. Astrophys.* 482:21–42

47. Cirasuolo M, McLure RJ, Dunlop JS, Almaini O, Foucaud S, Simpson C. 2010. *MNRAS* 401:1166–1176

48. Cirasuolo M, McLure RJ, Dunlop JS, Almaini O, Foucaud S, et al. 2007. *MNRAS* 380:585–595

49. Cole S, Norberg P, Baugh CM, Frenk CS, Bland-Hawthorn J, et al. 2001. *MNRAS* 326:255–273

50. Colless M, Dalton G, Maddox S, Sutherland W, Norberg P, et al. 2001. *MNRAS* 328:1039–1063

51. Condon JJ. 1992. *Annu. Rev. Astron. Astrophys.* 30:575–611

52. Conroy C, Gunn JE, White M. 2009. *Ap. J.* 699:486–506

53. Conroy C, Shapley AE, Tinker JL, Santos MR, Lemson G. 2008. *Ap. J.* 679:1192–1203

54. Conselice CJ, Chapman SC, Windhorst RA. 2003. *Ap. J. Lett.* 596:L5–L8

55. Coppin K, Halpern M, Scott D, Borys C, Dunlop J, et al. 2008. *MNRAS* 384:1597–1610

56. Cowie LL, Hu EM. 1998. *Astron. J.* 115:1319–1328

57. Cowie LL, Hu EM, Songaila A. 1995. *Astron. J.* 110:1576–+

58. Cresci G, Hicks EKS, Genzel R, Schreiber NMF, Davies R, et al. 2009. *Ap. J.* 697:115–132

59. Cresci G, Mannucci F, Maiolino R, Marconi A, Gnerucci A, Magrini L. 2010. *Nature* 467:811–813

60. Daddi E, Bournaud F, Walter F, Dannerbauer H, Carilli CL, et al. 2010. *Ap. J.* 713:686–707

61. Daddi E, Cimatti A, Renzini A, Fontana A, Mignoli M, et al. 2004. *Ap. J.* 617:746–764

62. Daddi E, Dickinson M, Morrison G, Chary R, Cimatti A, et al. 2007. *Ap. J.* 670:156–172

63. Daddi E, Renzini A, Pirzkal N, Cimatti A, Malhotra S, et al. 2005. *Ap. J.* 626:680–697

64. Dale DA, Helou G. 2002. *Ap. J.* 576:159–168

65. Damjanov I, McCarthy PJ, Abraham RG, Glazebrook K, Yan H, et al. 2009. *Ap. J.* 695:101–115

66. Dannerbauer H, Daddi E, Riechers DA, Walter F, Carilli CL, et al. 2009. *Ap. J. Lett.* 698:L178–L182

67. Davé R. 2008. *MNRAS* 385:147–160

68. Davé R, Finlator K, Oppenheimer BD, Fardal M, Katz N, et al. 2010. *MNRAS* 404:1355–1368

69. Davis M, Guhathakurta P, Konidaris NP, Newman JA, Ashby MLN, et al. 2007. *Ap. J. Lett.* 660:L1–L6

70. Dekel A, Birnboim Y, Engel G, Freundlich J, Goerdt T, et al. 2009. *Nature* 457:451–454

71. Dekel A, Sari R, Ceverino D. 2009. *Ap. J.* 703:785–801

72. Dessauges-Zavadsky M, D'Odorico S, Schaerer D, Modigliani A, Tapken C, Vernet J. 2010. *Astron. Astrophys.* 510:A26+

73. Dey A, Soifer BT, Desai V, Brand K, Le Floc'h E, et al. 2008. *Ap. J.* 677:943–956

74. Dickinson M. 2000. In *Astronomy, physics and chemistry of* H_3^+, vol. 358 of *Royal Society of London Philosophical Transactions Series A*

75. Dickinson M, Papovich C, Ferguson HC, Budavári T. 2003. *Ap. J.* 587:25–40

76. Drory N, Salvato M, Gabasch A, Bender R, Hopp U, et al. 2005. *Ap. J. Lett.* 619:L131–L134

77. Elbaz D, Cesarsky CJ, Chanial P, Aussel H, Franceschini A, et al. 2002. *Astron. Astrophys.* 384:848–865

78. Elbaz D, Daddi E, Le Borgne D, Dickinson M, Alexander DM, et al. 2007. *Astron. Astrophys.* 468:33–48

79. Elmegreen BG, Bournaud F, Elmegreen DM. 2008. *Ap. J.* 688:67–77

80. Elmegreen BG, Elmegreen DM. 2005. *Ap. J.* 627:632–646

81. Elmegreen BG, Elmegreen DM, Fernandez MX, Lemonias JJ. 2009. *Ap. J.* 692:12–31

82. Elsner F, Feulner G, Hopp U. 2008. *Astron. Astrophys.* 477:503–512

83. Engel H, Tacconi LJ, Davies RI, Neri R, Smail I, et al. 2010. *Ap. J.* 724:233–243

84. Erb DK. 2008. *Ap. J.* 674:151–156

85. Erb DK, Shapley AE, Pettini M, Steidel CC, Reddy NA, Adelberger KL. 2006a. *Ap. J.* 644:813–828

86. Erb DK, Shapley AE, Steidel CC, Pettini M, Adelberger KL, et al. 2003. *Ap. J.* 591:101–118

87. Erb DK, Steidel CC, Shapley AE, Pettini M, Adelberger KL. 2004. *Ap. J.* 612:122–130

88. Erb DK, Steidel CC, Shapley AE, Pettini M, Reddy NA, Adelberger KL. 2006b. *Ap. J.* 647:128–139

89. Erb DK, Steidel CC, Shapley AE, Pettini M, Reddy NA, Adelberger KL. 2006c. *Ap. J.* 646:107–132

90. Fan L, Lapi A, De Zotti G, Danese L. 2008. *Ap. J. Lett.* 689:L101–L104

91. Finlator K, Davé R. 2008. *MNRAS* 385:2181–2204

92. Fioc M, Rocca-Volmerange B. 1997. *Astron. Astrophys.* 326:950–962

93. Fontana A, Pozzetti L, Donnarumma I, Renzini A, Cimatti A, et al. 2004. *Astron. Astrophys.* 424:23–42

94. Fontana A, Salimbeni S, Grazian A, Giallongo E, Pentericci L, et al. 2006. *Astron. Astrophys.* 459:745–757

95. Förster Schreiber NM, Genzel R, Bouché N, Cresci G, Davies R, et al. 2009. *Ap. J.* 706:1364–1428

96. Förster Schreiber NM, Shapley AE, Erb DK, Genzel R, Steidel CC, et al. 2011. *Ap. J.* 731:65–+

97. Förster Schreiber NM, van Dokkum PG, Franx M, Labbé I, Rudnick G, et al. 2004. *Ap. J.* 616:40–62

98. Franx M, Labbé I, Rudnick G, van Dokkum PG, Daddi E, et al. 2003. *Ap. J. Lett.* 587:L79–L82

99. Franx M, van Dokkum PG, Schreiber NMF, Wuyts S, Labbé I, Toft S. 2008. *Ap. J.* 688:770–788

100. Gabasch A, Bender R, Seitz S, Hopp U, Saglia RP, et al. 2004. *Astron. Astrophys.* 421:41–58

101. Gawiser E, Francke H, Lai K, Schawinski K, Gronwall C, et al. 2007. *Ap. J.* 671:278–284

102. Genel S, Genzel R, Bouché N, Sternberg A, Naab T, et al. 2008. *Ap. J.* 688:789–793

103. Genzel R, Baker AJ, Tacconi LJ, Lutz D, Cox P, et al. 2003. *Ap. J.* 584:633–642

104. Genzel R, Burkert A, Bouché N, Cresci G, Förster Schreiber NM, et al. 2008. *Ap. J.* 687:59–77

105. Genzel R, Newman S, Jones T, Förster Schreiber NM, Shapiro K, et al. 2011. *Ap. J.* 733:101–+

106. Genzel R, Tacconi LJ, Gracia-Carpio J, Sternberg A, Cooper MC, et al. 2010. *MNRAS* 407:2091–2108

107. Giavalisco M, Steidel CC, Macchetto FD. 1996. *Ap. J.* 470:189–+

108. Graves GJ, Faber SM. 2010. *Ap. J.* 717:803–824

109. Greve TR, Bertoldi F, Smail I, Neri R, Chapman SC, et al. 2005. *MNRAS* 359:1165–1183

110. Gronwall C, Ciardullo R, Hickey T, Gawiser E, Feldmeier JJ, et al. 2007. *Ap. J.* 667:79–91

111. Hainline KN, Shapley AE, Kornei KA, Pettini M, Buckley-Geer E, et al. 2009. *Ap. J.* 701:52–65

112. Halliday C, Daddi E, Cimatti A, Kurk J, Renzini A, et al. 2008. *Astron. Astrophys.* 479:417–425

113. Harris AI, Baker AJ, Zonak SG, Sharon CE, Genzel R, et al. 2010. *Ap. J.* 723:1139–1149

114. Hayashi M, Motohara K, Shimasaku K, Onodera M, Uchimoto YK, et al. 2009. *Ap. J.* 691:140–151

115. Hayes M, Schaerer D, Östlin G, Mas-Hesse JM, Atek H, Kunth D. 2011. *Ap. J.* 730:8–+

116. Hopkins AM. 2004. *Ap. J.* 615:209–221

117. Hopkins AM, Beacom JF. 2006. *Ap. J.* 651:142–154

118. Hopkins PF, Bundy K, Hernquist L, Wuyts S, Cox TJ. 2010. *MNRAS* 401:1099–1117

119. Hopkins PF, Bundy K, Murray N, Quataert E, Lauer TR, Ma C. 2009. *MNRAS* 398:898–910

120. Ivison RJ, Papadopoulos PP, Smail I, Greve TR, Thomson AP, et al. 2011. *MNRAS* 412:1913–1925

121. Jones TA, Swinbank AM, Ellis RS, Richard J, Stark DP. 2010. *MNRAS* 404:1247–1262

122. Kajisawa M, Ichikawa T, Tanaka I, Konishi M, Yamada T, et al. 2009. *Ap. J.* 702:1393–1412

123. Kajisawa M, Ichikawa T, Yamada T, Uchimoto YK, Yoshikawa T, et al. 2010. *Ap. J.* 723:129–145

124. Kauffmann G, Heckman TM, White SDM, Charlot S, Tremonti C, et al. 2003a. *MNRAS* 341:33–53

125. Kauffmann G, Heckman TM, White SDM, Charlot S, Tremonti C, et al. 2003b. *MNRAS* 341:54–69

126. Kennicutt Jr. RC. 1998. *Annu. Rev. Astron. Astrophys.* 36:189–232

127. Kereš D, Katz N, Fardal M, Davé R, Weinberg DH. 2009. *MNRAS* 395:160–179

128. Kereš D, Katz N, Weinberg DH, Davé R. 2005. *MNRAS* 363:2–28

129. Kewley LJ, Dopita MA. 2002. *Ap. J. Suppl.* 142:35–52

130. Kewley LJ, Ellison SL. 2008. *Ap. J.* 681:1183–1204

131. Komatsu E, Smith KM, Dunkley J, Bennett CL, Gold B, et al. 2011. *Ap. J. Suppl.* 192:18–+

132. Kornei KA, Shapley AE, Erb DK, Steidel CC, Reddy NA, et al. 2010. *Ap. J.* 711:693–710

133. Kovács A, Chapman SC, Dowell CD, Blain AW, Ivison RJ, et al. 2006. *Ap. J.* 650:592–603

134. Kriek M, Labbé I, Conroy C, Whitaker KE, van Dokkum PG, et al. 2010. *Ap. J. Lett.* 722:L64–L69

135. Kriek M, van der Wel A, van Dokkum PG, Franx M, Illingworth GD. 2008a. *Ap. J.* 682:896–906

136. Kriek M, van Dokkum PG, Franx M, Illingworth GD, Coppi P, et al. 2007. *Ap. J.* 669:776–790

137. Kriek M, van Dokkum PG, Franx M, Illingworth GD, Magee DK. 2009. *Ap. J. Lett.* 705:L71–L75

138. Kriek M, van Dokkum PG, Franx M, Illingworth GD, Marchesini D, et al. 2008b. *Ap. J.* 677:219–237

139. Law DR, Steidel CC, Erb DK, Larkin JE, Pettini M, et al. 2009. *Ap. J.* 697:2057–2082

140. Law DR, Steidel CC, Erb DK, Pettini M, Reddy NA, et al. 2007. *Ap. J.* 656:1–26

141. Le Fèvre O, Vettolani G, Garilli B, Tresse L, Bottini D, et al. 2005. *Astron. Astrophys.* 439:845–862

142. Le Floc'h E, Papovich C, Dole H, Bell EF, Lagache G, et al. 2005. *Ap. J.* 632:169–190

143. Lehnert MD, Nesvadba NPH, Tiran LL, Matteo PD, van Driel W, et al. 2009. *Ap. J.* 699:1660–1678

144. Leitherer C, Schaerer D, Goldader JD, González Delgado RM, Robert C, et al. 1999. *Ap. J. Suppl.* 123:3–40

145. Lilly SJ, Le Fevre O, Hammer F, Crampton D. 1996. *Ap. J. Lett.* 460:L1+

146. Lotz JM, Madau P, Giavalisco M, Primack J, Ferguson HC. 2006. *Ap. J.* 636:592–609

147. Lotz JM, Primack J, Madau P. 2004. *Astron. J.* 128:163–182

148. Lowenthal JD, Koo DC, Guzman R, Gallego J, Phillips AC, et al. 1997. *Ap. J.* 481:673–+

149. Madau P, Ferguson HC, Dickinson ME, Giavalisco M, Steidel CC, Fruchter A. 1996. *MNRAS* 283:1388–1404

150. Magdis GE, Elbaz D, Daddi E, Morrison GE, Dickinson M, et al. 2010a. *Ap. J.* 714:1740–1745

151. Magdis GE, Elbaz D, Hwang HS, Amblard A, Arumugam V, et al. 2010b. *MNRAS* 409:22–28

152. Maiolino R, Nagao T, Grazian A, Cocchia F, Marconi A, et al. 2008. *Astron. Astrophys.* 488:463–479

153. Mannucci F, Cresci G, Maiolino R, Marconi A, Gnerucci A. 2010. *MNRAS* 408:2115–2127

154. Mannucci F, Cresci G, Maiolino R, Marconi A, Pastorini G, et al. 2009. *MNRAS* 398:1915–1931

155. Maraston C. 2005. *MNRAS* 362:799–825

156. Maraston C, Daddi E, Renzini A, Cimatti A, Dickinson M, et al. 2006. *Ap. J.* 652:85–96

157. Maraston C, Pforr J, Renzini A, Daddi E, Dickinson M, et al. 2010. *MNRAS* 407:830–845

158. Marchesini D, van Dokkum P, Quadri R, Rudnick G, Franx M, et al. 2007. *Ap. J.* 656:42–65

159. Marchesini D, van Dokkum PG, Förster Schreiber NM, Franx M, Labbé I, Wuyts S. 2009. *Ap. J.* 701:1765–1796

160. Menéndez-Delmestre K, Blain AW, Smail I, Alexander DM, Chapman SC, et al. 2009. *Ap. J.* 699:667–685

161. Meurer GR, Heckman TM, Calzetti D. 1999. *Ap. J.* 521:64–80

162. Michałowski M, Hjorth J, Watson D. 2010. *Astron. Astrophys.* 514:A67+

163. Muzzin A, Marchesini D, van Dokkum PG, Labbé I, Kriek M, Franx M. 2009. *Ap. J.* 701:1839–1864

164. Naab T, Johansson PH, Ostriker JP. 2009. *Ap. J. Lett.* 699:L178–L182

165. Nagao T, Maiolino R, Marconi A. 2006. *Astron. Astrophys.* 459:85–101

166. Neri R, Genzel R, Ivison RJ, Bertoldi F, Blain AW, et al. 2003. *Ap. J. Lett.* 597:L113–L116

167. Nilsson KK, Östlin G, Møller P, Möller-Nilsson O, Tapken C, et al. 2011. *Astron. Astrophys.* 529:A9+

168. Noeske KG, Weiner BJ, Faber SM, Papovich C, Koo DC, et al. 2007. *Ap. J. Lett.* 660:L43–L46

169. Nordon R, Lutz D, Shao L, Magnelli B, Berta S, et al. 2010. *Astron. Astrophys.* 518:L24+

170. Oesch PA, Bouwens RJ, Illingworth GD, Carollo CM, Franx M, et al. 2010. *Ap. J. Lett.* 709:L16–L20

171. Omont A, Petitjean P, Guilloteau S, McMahon RG, Solomon PM, Pécontal E. 1996. *Nature* 382:428–431

172. Ouchi M, Shimasaku K, Akiyama M, Simpson C, Saito T, et al. 2008. *Ap. J. Suppl.* 176:301–330

173. Ouchi M, Shimasaku K, Okamura S, Furusawa H, Kashikawa N, et al. 2004. *Ap. J.* 611:660–684

174. Overzier RA, Heckman TM, Schiminovich D, Basu-Zych A, Gonçalves T, et al. 2010. *Ap. J.* 710:979–991

175. Paltani S, Le Fèvre O, Ilbert O, Arnouts S, Bardelli S, et al. 2007. *Astron. Astrophys.* 463:873–882

176. Pannella M, Carilli CL, Daddi E, McCracken HJ, Owen FN, et al. 2009. *Ap. J. Lett.* 698:L116–L120

177. Papovich C, Dickinson M, Ferguson HC. 2001. *Ap. J.* 559:620–653

178. Papovich C, Dickinson M, Giavalisco M, Conselice CJ, Ferguson HC. 2005. *Ap. J.* 631:101–120

179. Papovich C, Finkelstein SL, Ferguson HC, Lotz JM, Giavalisco M. 2011. *MNRAS* 412:1123–1136

180. Papovich C, Moustakas LA, Dickinson M, Le Floc'h E, Rieke GH, et al. 2006. *Ap. J.* 640:92–113

181. Pérez-González PG, Rieke GH, Egami E, Alonso-Herrero A, Dole H, et al. 2005. *Ap. J.* 630:82–107

182. Pérez-González PG, Rieke GH, Villar V, Barro G, Blaylock M, et al. 2008. *Ap. J.* 675:234–261

183. Pettini M, Ellison SL, Steidel CC, Shapley AE, Bowen DV. 2000. *Ap. J.* 532:65–76

184. Pettini M, Pagel BEJ. 2004. *MNRAS* 348:L59–L63

185. Pettini M, Rix SA, Steidel CC, Adelberger KL, Hunt MP, Shapley AE. 2002. *Ap. J.* 569:742–757

186. Pettini M, Shapley AE, Steidel CC, Cuby J, Dickinson M, et al. 2001. *Ap. J.* 554:981–1000

187. Pope A, Chary R, Alexander DM, Armus L, Dickinson M, et al. 2008. *Ap. J.* 675:1171–1193

188. Pozzetti L, Bolzonella M, Lamareille F, Zamorani G, Franzetti P, et al. 2007. *Astron. Astrophys.* 474:443–459

189. Prevot ML, Lequeux J, Prevot L, Maurice E, Rocca-Volmerange B. 1984. *Astron. Astrophys.* 132:389–392

190. Quider AM, Pettini M, Shapley AE, Steidel CC. 2009. *MNRAS* 398:1263–1278

191. Quider AM, Shapley AE, Pettini M, Steidel CC, Stark DP. 2010. *MNRAS* 402:1467–1479

192. Ranalli P, Comastri A, Setti G. 2003. *Astron. Astrophys.* 399:39–50

193. Ravindranath S, Giavalisco M, Ferguson HC, Conselice C, Katz N, et al. 2006. *Ap. J.* 652:963–980

194. Reddy NA, Erb DK, Pettini M, Steidel CC, Shapley AE. 2010. *Ap. J.* 712:1070–1091

195. Reddy NA, Erb DK, Steidel CC, Shapley AE, Adelberger KL, Pettini M. 2005. *Ap. J.* 633:748–767

196. Reddy NA, Steidel CC. 2004. *Ap. J. Lett.* 603:L13–L16

197. Reddy NA, Steidel CC. 2009. *Ap. J.* 692:778–803

198. Reddy NA, Steidel CC, Fadda D, Yan L, Pettini M, et al. 2006. *Ap. J.* 644:792–812

199. Reddy NA, Steidel CC, Pettini M, Adelberger KL, Shapley AE, et al. 2008. *Ap. J. Suppl.* 175:48–85

200. Rhoads JE, Malhotra S, Dey A, Stern D, Spinrad H, Jannuzi BT. 2000. *Ap. J. Lett.* 545:L85–L88

201. Rieke GH, Alonso-Herrero A, Weiner BJ, Pérez-González PG, Blaylock M, et al. 2009. *Ap. J.* 692:556–573

202. Rix SA, Pettini M, Leitherer C, Bresolin F, Kudritzki R, Steidel CC. 2004. *Ap. J.* 615:98–117

203. Rodighiero G, Vaccari M, Franceschini A, Tresse L, Le Fevre O, et al. 2010. *Astron. Astrophys.* 515:A8+

204. Sajina A, Yan L, Armus L, Choi P, Fadda D, et al. 2007. *Ap. J.* 664:713–737

205. Salpeter EE. 1955. *Ap. J.* 121:161–+

206. Sawicki M. 2001. *Astron. J.* 121:2405–2412

207. Sawicki M, Thompson D. 2006. *Ap. J.* 642:653–672

208. Sawicki M, Yee HKC. 1998. *Astron. J.* 115:1329–1339

209. Schechter P. 1976. *Ap. J.* 203:297–306

210. Shapiro KL, Genzel R, Quataert E, Förster Schreiber NM, Davies R, et al. 2009. *Ap. J.* 701:955–963

211. Shapley AE, Erb DK, Pettini M, Steidel CC, Adelberger KL. 2004. *Ap. J.* 612:108–121

212. Shapley AE, Steidel CC, Adelberger KL, Dickinson M, Giavalisco M, Pettini M. 2001. *Ap. J.* 562:95–123

213. Shapley AE, Steidel CC, Erb DK, Reddy NA, Adelberger KL, et al. 2005. *Ap. J.* 626:698–722

214. Shapley AE, Steidel CC, Pettini M, Adelberger KL. 2003. *Ap. J.* 588:65–89

215. Shen S, Mo HJ, White SDM, Blanton MR, Kauffmann G, et al. 2003. *MNRAS* 343:978–994

216. Siana B, Smail I, Swinbank AM, Richard J, Teplitz HI, et al. 2009. *Ap. J.* 698:1273–1281

217. Siana B, Teplitz HI, Chary R, Colbert J, Frayer DT. 2008. *Ap. J.* 689:59–67

218. Smail I, Ivison RJ, Blain AW. 1997. *Ap. J. Lett.* 490:L5+

219. Smail I, Swinbank AM, Richard J, Ebeling H, Kneib J, et al. 2007. *Ap. J. Lett.* 654:L33–L36

220. Somerville RS, Hopkins PF, Cox TJ, Robertson BE, Hernquist L. 2008. *MNRAS* 391:481–506

221. Spergel DN, Verde L, Peiris HV, Komatsu E, Nolta MR, et al. 2003. *Ap. J. Suppl.* 148:175–194

222. Springel V, White SDM, Jenkins A, Frenk CS, Yoshida N, et al. 2005. *Nature* 435:629–636

223. Steidel CC, Adelberger KL, Dickinson M, Giavalisco M, Pettini M, Kellogg M. 1998. *Ap. J.* 492:428–+

224. Steidel CC, Adelberger KL, Giavalisco M, Dickinson M, Pettini M. 1999. *Ap. J.* 519:1–17

225. Steidel CC, Adelberger KL, Shapley AE, Erb DK, Reddy NA, Pettini M. 2005. *Ap. J.* 626:44–50

226. Steidel CC, Adelberger KL, Shapley AE, Pettini M, Dickinson M, Giavalisco M. 2003. *Ap. J.* 592:728–754

227. Steidel CC, Erb DK, Shapley AE, Pettini M, Reddy N, et al. 2010. *Ap. J.* 717:289–322

228. Steidel CC, Giavalisco M, Pettini M, Dickinson M, Adelberger KL. 1996. *Ap. J. Lett.* 462:L17

229. Steidel CC, Shapley AE, Pettini M, Adelberger KL, Erb DK, et al. 2004. *Ap. J.* 604:534–550

230. Stolte A, Grebel EK, Brandner W, Figer DF. 2002. *Astron. Astrophys.* 394:459–478

231. Strateva I, Ivezić Ž, Knapp GR, Narayanan VK, Strauss MA, et al. 2001. *Astron. J.* 122:1861–1874

232. Swinbank AM, Chapman SC, Smail I, Lindner C, Borys C, et al. 2006. *MNRAS* 371:465–476

233. Swinbank AM, Smail I, Chapman SC, Blain AW, Ivison RJ, Keel WC. 2004. *Ap. J.* 617:64–80

234. Swinbank AM, Smail I, Chapman SC, Borys C, Alexander DM, et al. 2010. *MNRAS* 405:234–244

235. Tacconi LJ, Genzel R, Neri R, Cox P, Cooper MC, et al. 2010. *Nature* 463:781–784

236. Tacconi LJ, Genzel R, Smail I, Neri R, Chapman SC, et al. 2008. *Ap. J.* 680:246–262

237. Tacconi LJ, Neri R, Chapman SC, Genzel R, Smail I, et al. 2006. *Ap. J.* 640:228–240

238. Taylor EN, Franx M, Glazebrook K, Brinchmann J, van der Wel A, van Dokkum PG. 2010. *Ap. J.* 720:723–741

239. Thomas D, Maraston C, Bender R, Mendes de Oliveira C. 2005. *Ap. J.* 621:673–694

240. Tinsley BM. 1968. *Ap. J.* 151:547–+

241. Toft S, Franx M, van Dokkum P, Förster Schreiber NM, Labbe I, et al. 2009. *Ap. J.* 705:255–260

242. Toft S, van Dokkum P, Franx M, Labbe I, Förster Schreiber NM, et al. 2007. *Ap. J.* 671:285–302

243. Toft S, van Dokkum P, Franx M, Thompson RI, Illingworth GD, et al. 2005. *Ap. J. Lett.* 624:L9–L12

244. Tremonti CA, Heckman TM, Kauffmann G, Brinchmann J, Charlot S, et al. 2004. *Ap. J.* 613:898–913

245. Treu T, Auger MW, Koopmans LVE, Gavazzi R, Marshall PJ, Bolton AS. 2010. *Ap. J.* 709:1195–1202

246. Trujillo I, Conselice CJ, Bundy K, Cooper MC, Eisenhardt P, Ellis RS. 2007. *MNRAS* 382:109–120

247. van der Burg RFJ, Hildebrandt H, Erben T. 2010. *Astron. Astrophys.* 523:A74+

248. van der Wel A, Holden BP, Zirm AW, Franx M, Rettura A, et al. 2008. *Ap. J.* 688:48–58

249. van Dokkum PG. 2008. *Ap. J.* 674:29–50

250. van Dokkum PG, Conroy C. 2010. *Nature* 468:940–942

251. van Dokkum PG, Förster Schreiber NM, Franx M, Daddi E, Illingworth GD, et al. 2003. *Ap. J. Lett.* 587:L83–L87

252. van Dokkum PG, Franx M, Kriek M, Holden B, Illingworth GD, et al. 2008. *Ap. J. Lett.* 677:L5–L8

253. van Dokkum PG, Kriek M, Franx M. 2009. *Nature* 460:717–719

254. van Dokkum PG, Labbé I, Marchesini D, Quadri R, Brammer G, et al. 2009. *Publ. Astron. Soc. Pac.* 121:2–8

255. van Dokkum PG, Whitaker KE, Brammer G, Franx M, Kriek M, et al. 2010. *Ap. J.* 709:1018–1041

256. Venemans BP, Röttgering HJA, Miley GK, van Breugel WJM, de Breuck C, et al. 2007. *Astron. Astrophys.* 461:823–845

257. Wilkins SM, Trentham N, Hopkins AM. 2008. *MNRAS* 385:687–694

258. Williams RJ, Quadri RF, Franx M, van Dokkum P, Labbé I. 2009. *Ap. J.* 691:1879–1895

259. Williams RJ, Quadri RF, Franx M, van Dokkum P, Toft S, et al. 2010. *Ap. J.* 713:738–750

260. Wyder TK, Treyer MA, Milliard B, Schiminovich D, Arnouts S, et al. 2005. *Ap. J. Lett.* 619:L15–L18

261. Yan L, Sajina A, Fadda D, Choi P, Armus L, et al. 2007. *Ap. J.* 658:778–793

262. Yan L, Tacconi LJ, Fiolet N, Sajina A, Omont A, et al. 2010. *Ap. J.* 714:100–114

263. Yoshikawa T, Akiyama M, Kajisawa M, Alexander DM, Ohta K, et al. 2010. *Ap. J.* 718:112–132

264. Young JS, Scoville NZ. 1991. *Annu. Rev. Astron. Astrophys.* 29:581–625

265. Yun MS, Reddy NA, Condon JJ. 2001. *Ap. J.* 554:803–822

266. Zirm AW, van der Wel A, Franx M, Labbé I, Trujillo I, et al. 2007. *Ap. J.* 656:66–72

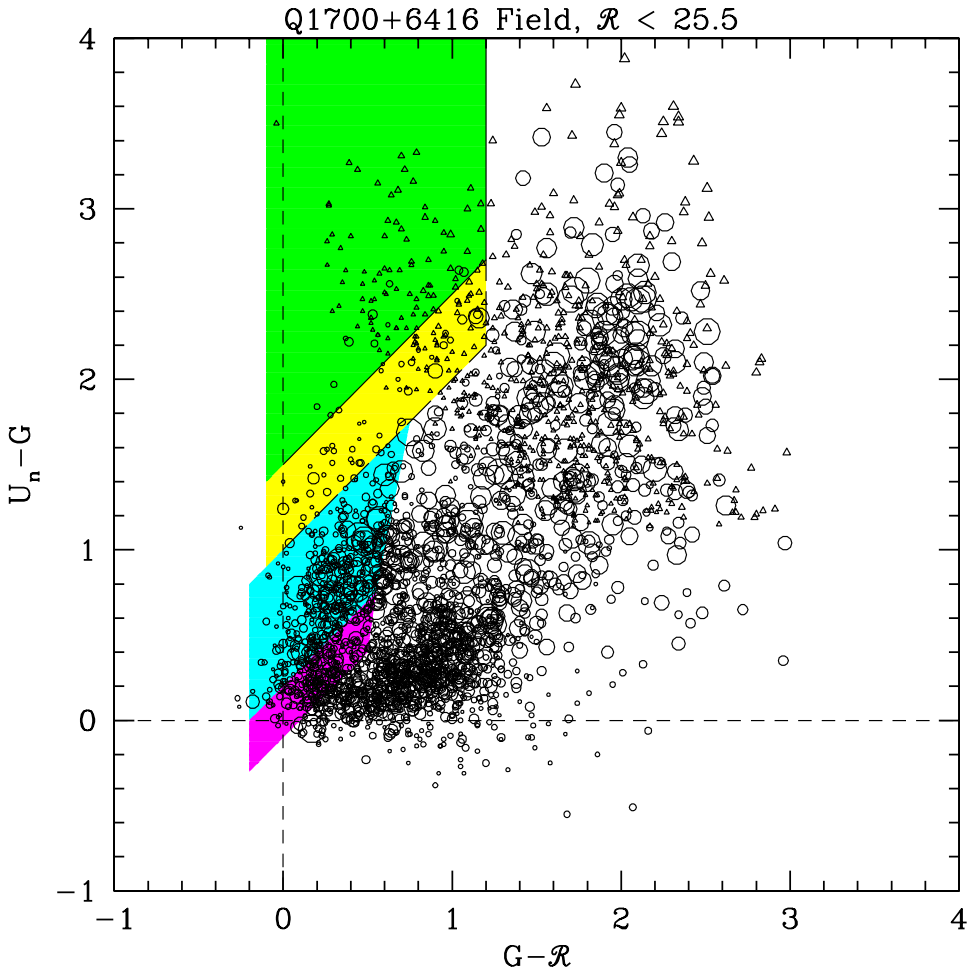

Figure 1: (From Steidel et al. 2004) Two-color ($U_n - G$ vs. $G - \mathcal{R}$) diagram from one of the UV-selected survey fields, demonstrating the UV-selection technique described in Section 2.2. The green and yellow shaded regions are the $z \sim 3$ LBG color selection windows, while the cyan and magenta regions are used to select galaxies at $z \sim 2.0 - 2.5$ and $z \sim 1.5 - 2.0$, respectively.

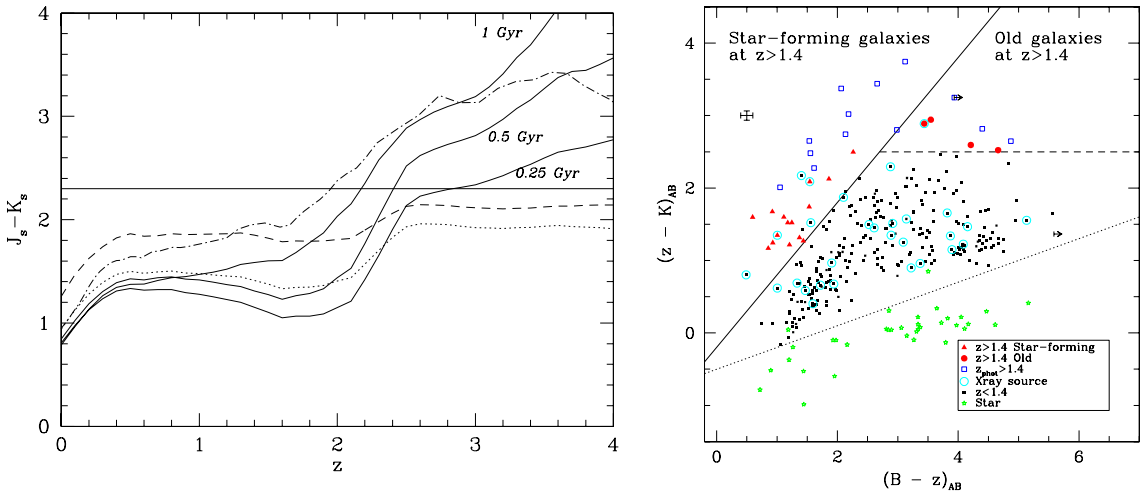

Figure 2: **Left:** (From Franx et al. 2003) $J_s - K_s$ (Vega) color as a function of redshift for several different galaxy spectral types, illustrating the DRG selection technique. Solid curves indicate single-age stellar populations with ages of 0.25, 0.5, and 1 Gyr. $J_s - K_s$ colors exceed a value of 2.3 at $z > 2$ as a result of either the Balmer or 4000 Å break moving into the J_s band. Dotted and dashed curves indicate models with continuous star formation with ages and reddenings of 1 Gyr, $E(V - B) = 0.15$, and 100 Myr, $E(B - V) = 0.5$, respectively. The dash-dotted curve indicates the color evolution of a single-burst population that formed at $z = 5$, and it also satisfies the color criterion above $z = 2$. **Right:** (From Daddi et al. 2004) Two-color ($z - K$ vs. $B - z$) diagram for galaxies in the GOODS field, illustrating the BzK selection technique. Solid triangles represent star-forming galaxies at $z > 1.4$, solid circles represent passive galaxies at $z > 1.4$, empty squares are objects with no measured spectroscopic redshift but with photometric redshift $z_{phot} > 1.4$. X-ray sources are circled, solid squares are objects at $z < 1.4$, and star symbols indicate Galactic objects. The solid and dashed lines indicate the regions of BzK color space used to identify star-forming and passive galaxies at $1.4 \leq z \leq 2.5$.

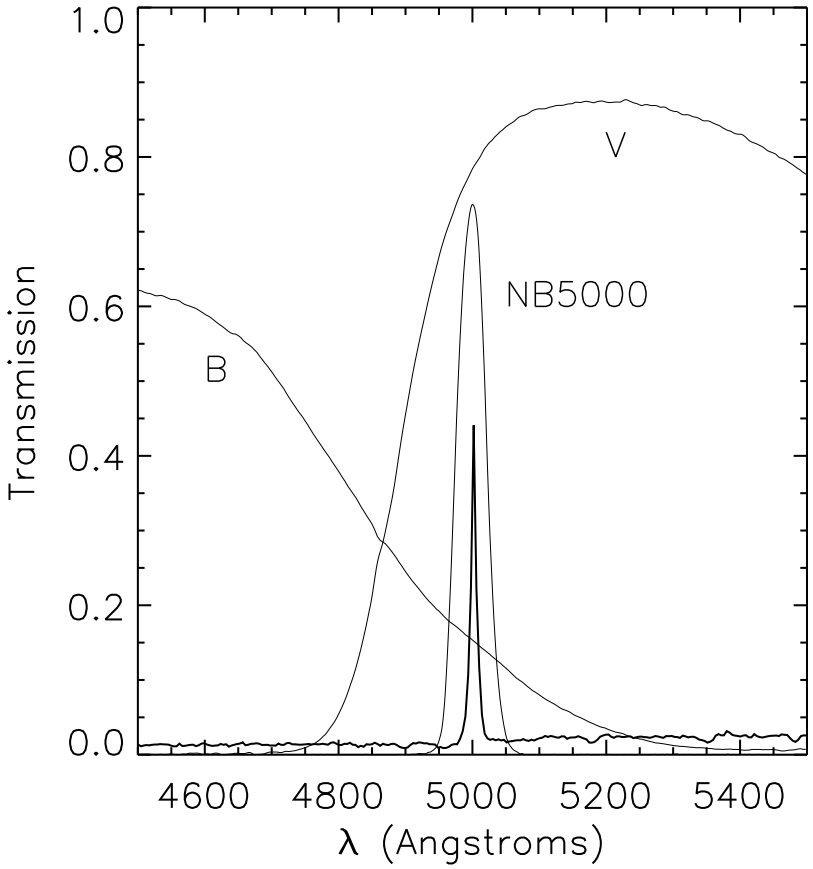

Figure 3: (From Gronwall et al. 2007) Filter bandpasses used for narrowband selection of LAEs at $z = 3.1$, where a spectrum of a typical $z = 3.1$ Lyα-emitting galaxy (overlaid for comparison) would be detected as having a red broadband minus narrowband color. This technique preferentially selects objects with bright line emission (and, often, faint continua).

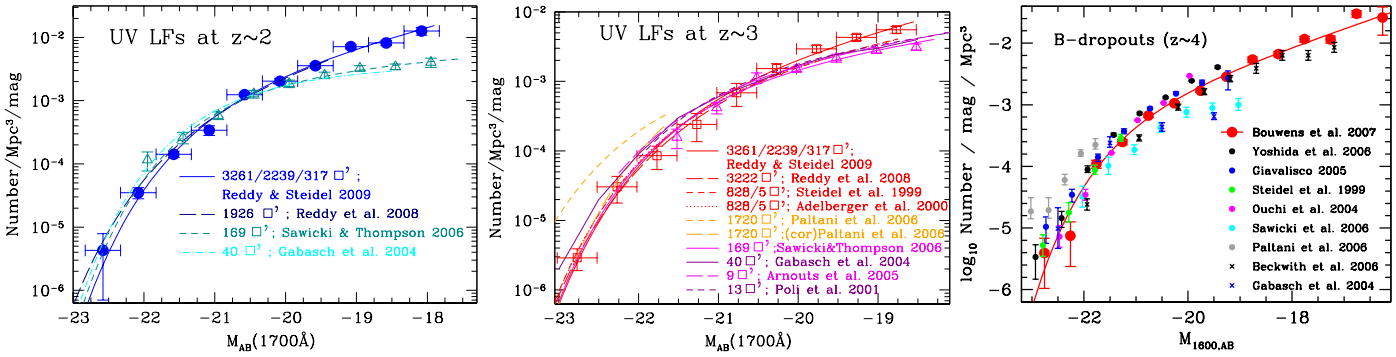

Figure 4: Multiple determinations of the $z \sim 2$, $z \sim 3$, and $z \sim 4$ rest-frame UV luminosity functions. **Left:** $z \sim 2$: (From Reddy & Steidel 2009) Points from Reddy & Steidel (2009) are shown as solid blue circles, while the results from other groups are indicated as in the legend, including survey areas. **Middle:** $z \sim 3$: (From Reddy & Steidel 2009) Points from Reddy & Steidel (2009) are shown as empty squares while the results from other groups are as indicated in the legend, including survey area. **Right:** $z \sim 4$: (From Bouwens et al. 2007) Points from Bouwens et al. (2007) are indicated as red circles. Results from other groups are as indicated in the legend.

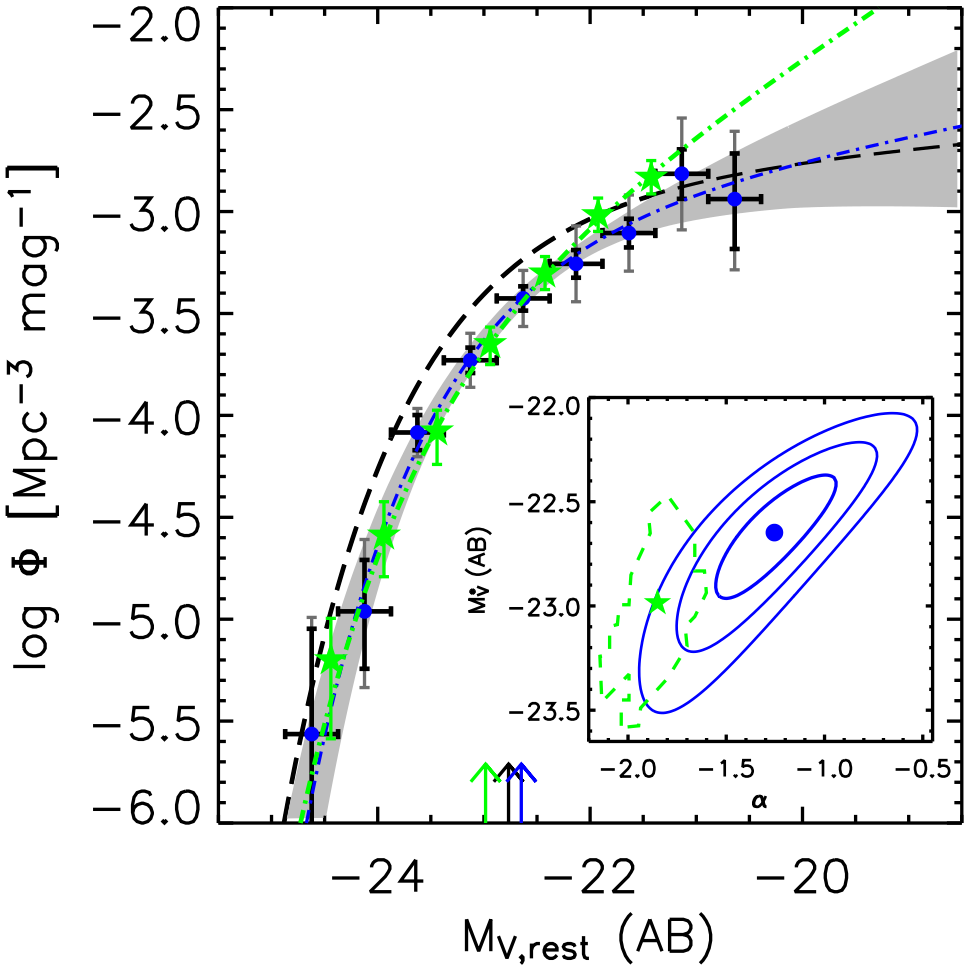

Figure 5: (From Marchesini et al. 2007) Rest-frame Optical Luminosity Functions. Comparison of rest-frame V-band luminosity functions at $z \sim 3$. Total rest-frame V-band luminosity function of K-selected galaxies at $2.7 \leq z \leq 3.3$ (black dashed line). Also shown are the V-band luminosity function of "blue" ($J-K \leq 2.3$) K-selected galaxies (blue circles), and the $z \sim 3$ LBG V-band luminosity function from Shapley et al. (2001) (green stars). Black error bars on the blue points represent Poisson uncertainties, whereas gray error bars also include field-to-field variations. The gray shaded area represents the 1σ uncertainties of the luminosity function of the blue, K-selected galaxies. The inset shows the best-fit value and 1, 2, and 3σ confidence intervals on α and M^* for the blue, K-selected galaxies (blue, solid curve), and LBGs (green, dashed curve).

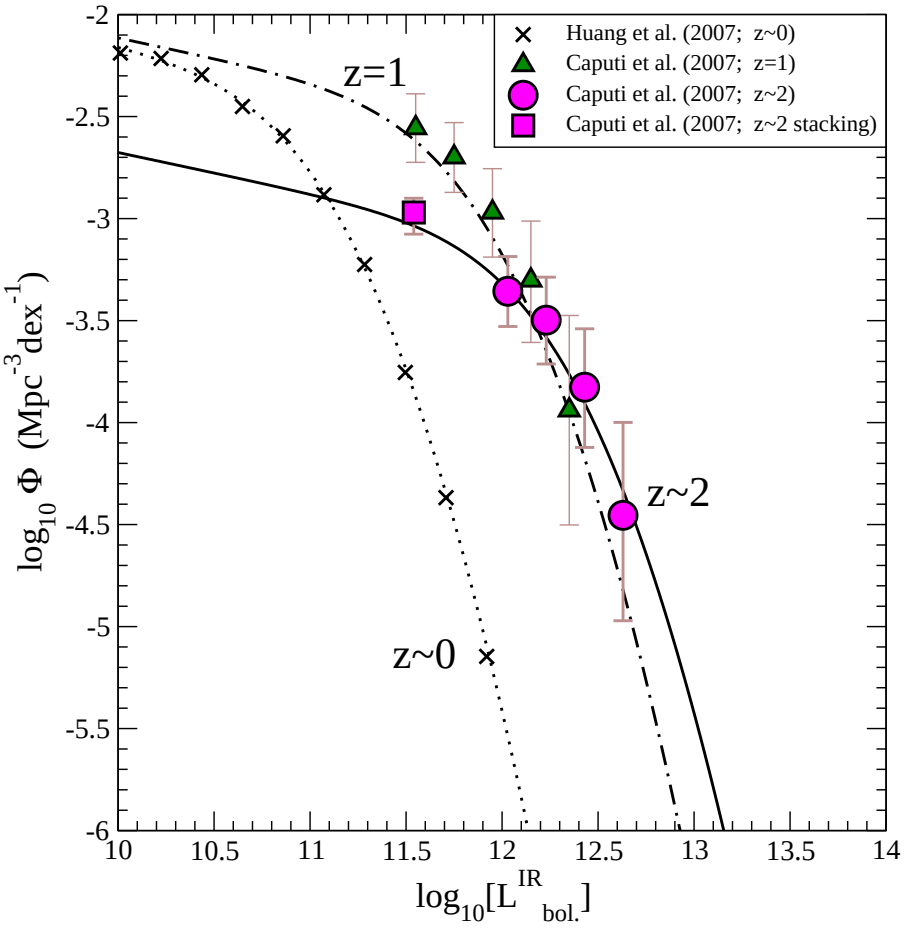

Figure 6: (From Caputi et al. 2007) IR Luminosity Functions. Bolometric IR luminosity functions for star-forming galaxies at $z \sim 2$ (individual detections: circles; stacked result for fainter galaxies: square) and $z \sim 1$ (triangles) in the GOODS fields. The local IR luminosity function is shown for comparison (crosses).

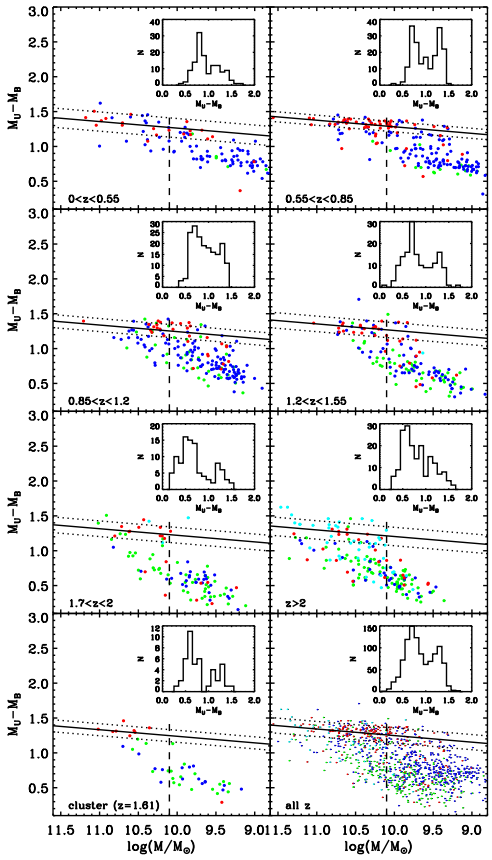

Figure 7: (From Cassata et al. 2008) Rest-frame $U - B$ color versus stellar mass in six bins of redshift, from $z \sim 0$ to $z \sim 2$. The bottom left panel indicates the color-magnitude diagram in a protocluster identified at $z = 1.61$, whereas the bottom right panel shows the color-magnitude diagram for all galaxies, regardless of redshift. In each panel, the diagonal continuous line indicates a fit to the red sequence. The dashed line indicates $\log(M/M_{\odot}) = 10.1$, the stellar mass completeness limit for galaxies on the red sequence. Color-coded symbols indicate galaxies in different morphological classes: red, blue, green, and cyan symbols respectively represent early-types, spirals, irregulars, and undetected objects. In each panel, the inset shows the one-dimensional distribution in $U - B$ color. A clear bimodality in the $U - B$ color distribution is observed to $z \sim 2$.

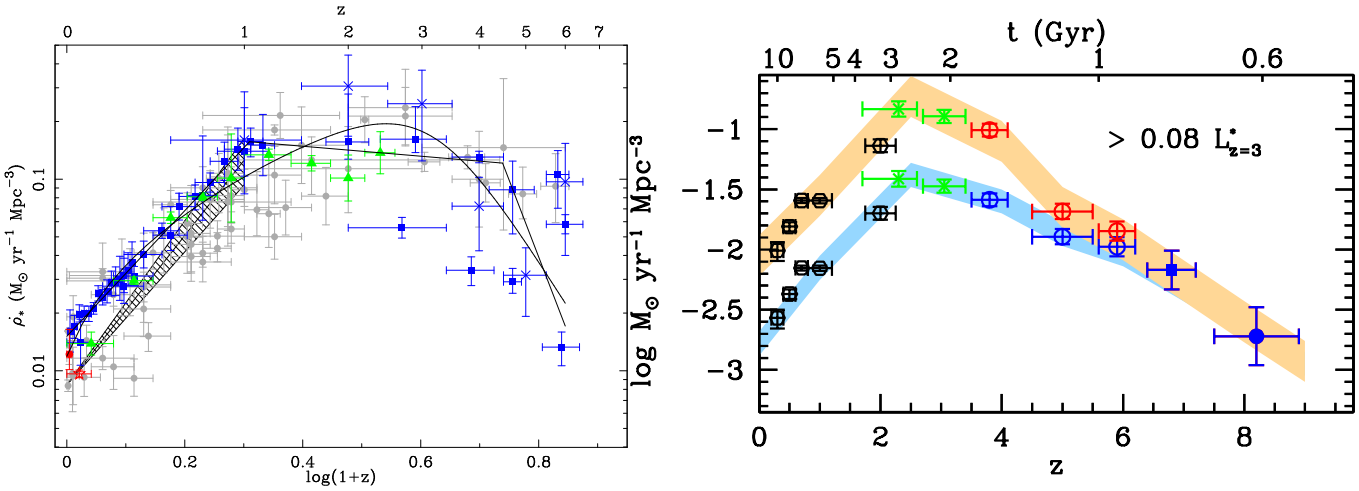

Figure 8: Star-formation History of the Universe. **Left:** (From Hopkins & Beacom 2006) Evolution of the star-formation rate density with redshift. Shown here is the multiwavelength compilation from Hopkins (2004) (gray points) and Hopkins & Beacom (2006) (all other symbols), and references therein. All data points have been scaled to a common IMF and dust correction. The hatched region is the FIR star-formation history from Le Floc'h et al. (2005). The solid lines represent best-fitting parametric forms to the data compilation from Hopkins & Beacom (2006). **Right:** (From Bouwens et al. 2010) Evolution of the star-formation rate density, based on rest-frame UV luminosity functions. At each redshift, the luminosity function is integrated down to $M_{UV} = -18.3$ AB mag, which is $0.08L^*$ at $z = 3$. The lower set of points (blue region) shows the star-formation rate density determination inferred directly from UV light with no dust correction applied. The upper set of points (orange region) shows the inferred star-formation rate density using dust corrections inferred from the measurement of UV continuum slopes.

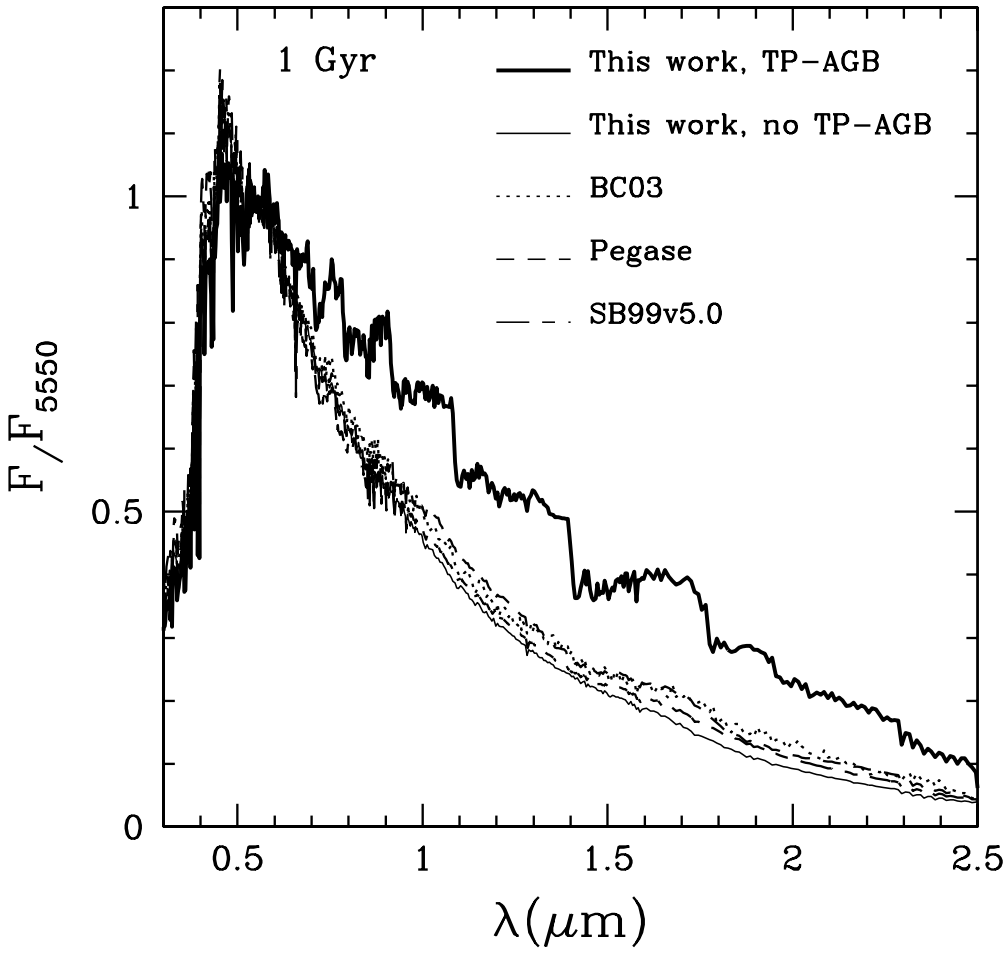

Figure 9: (From Maraston 2005) The effects of TP-AGB Stars on Stellar Population Synthesis Models. Shown here is a comparison of a 1 Gyr, solar metallicity stellar population model from Maraston (2005) both with (solid, thick line) and without (solid, thin line) the contributions of TP-AGB stars. Also shown are other models from the literature, including those from Bruzual & Charlot (2003), PEGASE, and Starburst99, as indicated in the legend. Differences in the treatment of the TP-AGB phase among stellar population synthesis codes lead to significant discrepancies in the predicted rest-frame near-IR spectra and luminosities of simple stellar populations with ages between 0.5 and 2.0 Gyr.

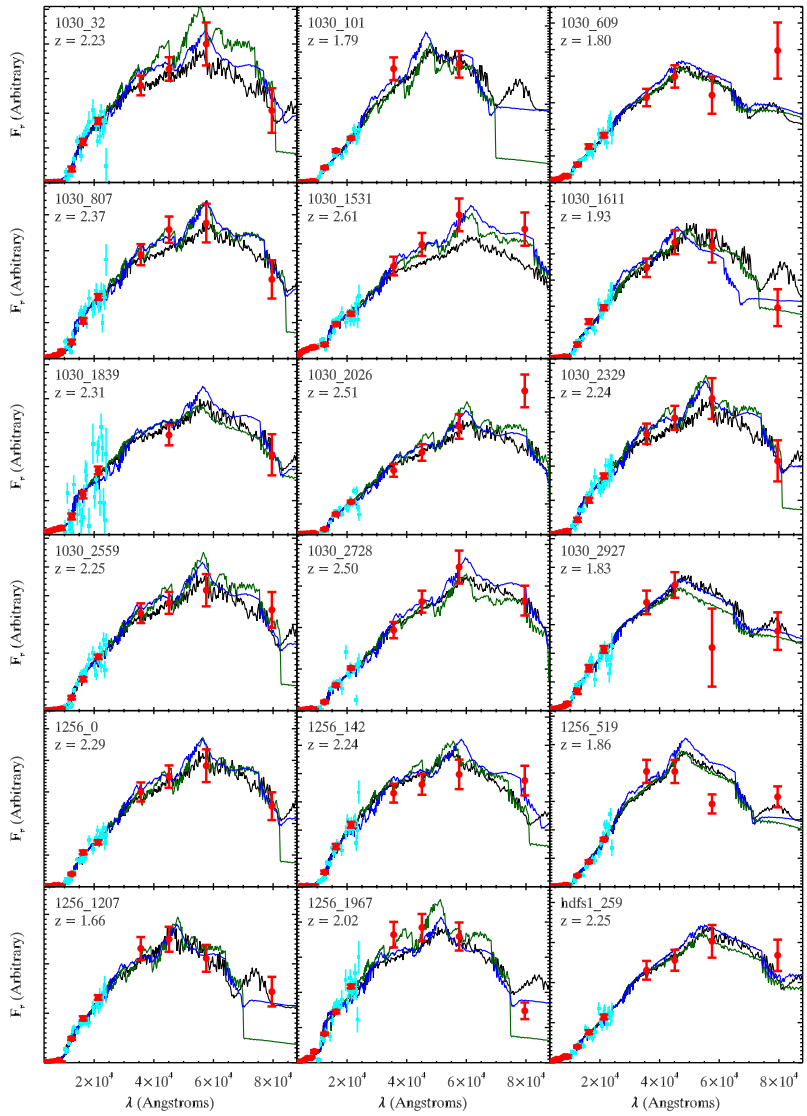

Figure 10: (From Muzzin et al. 2009) Sample population synthesis fits to optical through mid-IR SEDs, and using different stellar population synthesis codes. Shown here are well-sampled multiwavelength SEDs including broad-band optical and near-IR ($UBVRIz'JHK$) and *Spitzer*/IRAC photometry (red circles), as well as GNIRS near-IR spectroscopy (cyan points) for a sample of spectroscopically-confirmed galaxies at $z \sim 2$. Also shown are a comparison of Bruzual & Charlot (2003) (black curve), updated Charlot & Bruzual (blue curve), and Maraston (2005) (green curve) models.

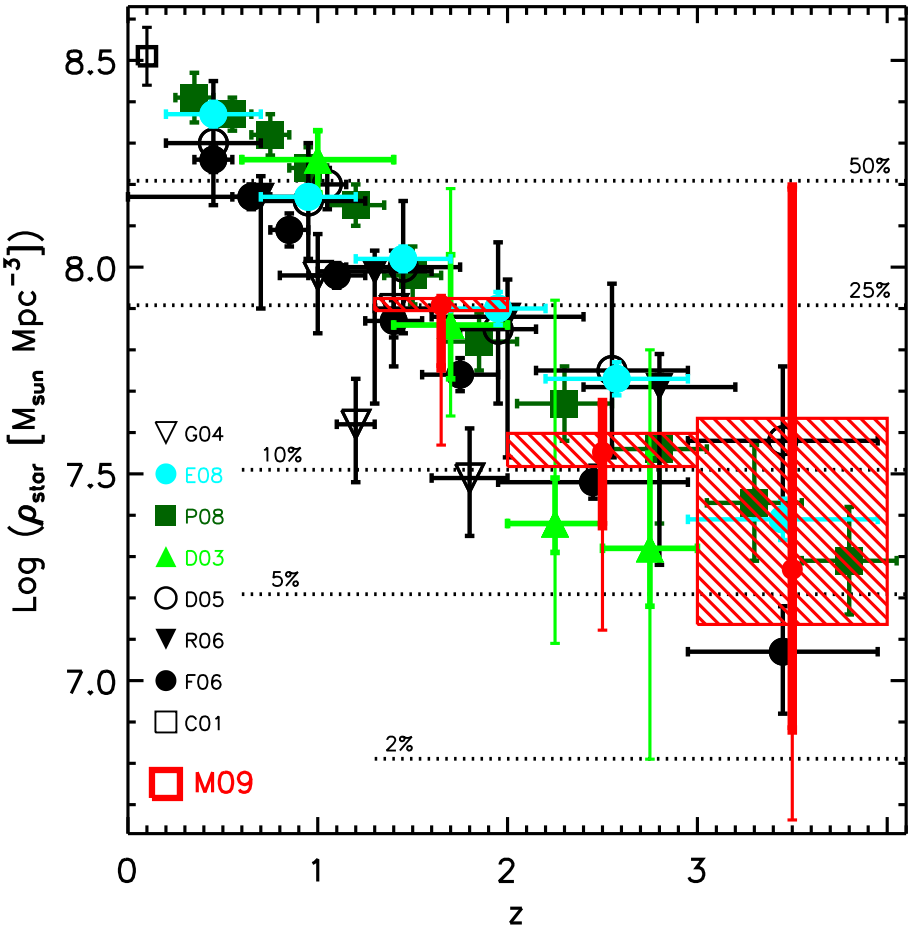

Figure 11: (From Marchesini et al. 2009) The results from various surveys on the evolution of the global stellar mass density. Mass-density estimates were obtained by integrating stellar mass functions over the mass range, $10^8 \leq M_{star}/M_{\odot} < 10^{13}$. Red symbols represent the total stellar mass densities estimated from Marchesini et al. (2009) (i.e., "M09"), where shaded boxes do not include the systematic uncertainties, and error bars do. Other estimates of stellar mass densities come from the literature, with references as in Marchesini et al. (2009). Horizontal dotted lines represent 50%, 25%, 10%, 5%, and 2% of the total stellar mass density at $z = 0.1$.

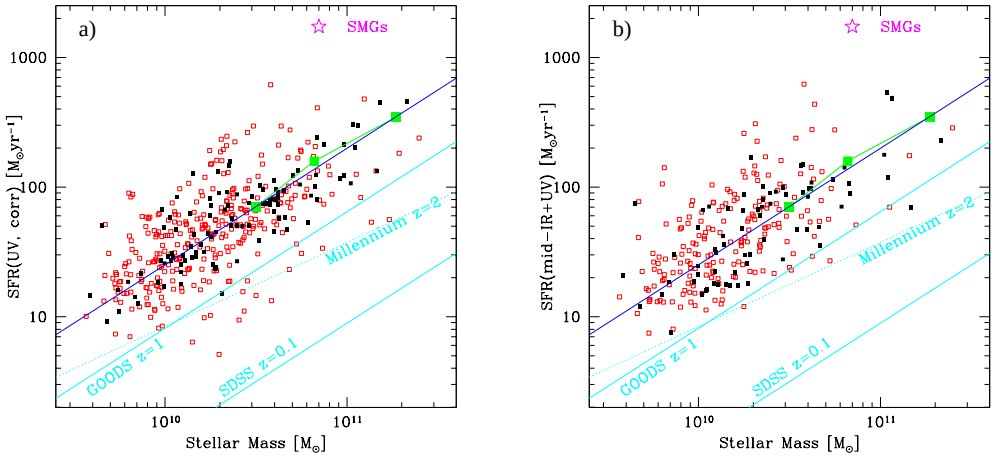

Figure 12: (From Daddi et al. 2007) The relationship between SFR and stellar mass for $z \sim 2$ star-forming galaxies in the GOODS fields. Only galaxies with 24μm detections are included. **Left:** Star-formation rates are derived from UV luminosities, corrected for dust extinction. **Right:** Star-formation rates are derived from the sum of mid-IR and UV-uncorrected luminosities. In both panels, filled and empty squares are objects with and without spectroscopic redshifts, respectively. The large green squares are the result of the average $SFR - M_{star}$ relation in GOODS-N based on radio stacking of $K < 20.5$ galaxies in three bins of stellar mass. The blue solid line is the functional form: $SFR = 200(M_{star}/10^{11} M_{\odot})^{0.9} (M_{\odot}\ \mathrm{yr}^{-1})$. The cyan solid lines are the $z = 1$ and $z = 0.1$ correlations from Elbaz et al. (2007). The cyan dashed line is a prediction for $z = 2$ from the Millennium simulation and semi-analytic models. The magenta star indicates the location of typical SMGs in this diagram. According to Daddi et al. (2007), star-forming galaxies at $z \sim 2$ appear to follow a strong correlation between star-formation rate and stellar mass. This trend is offset towards higher star-formation rates at fixed stellar mass, relative to the correlations observed among star-forming galaxies at lower redshift. The theoretical model shown here for $z \sim 2$ galaxies tends to underpredict the active rates of star formation for a given stellar mass.

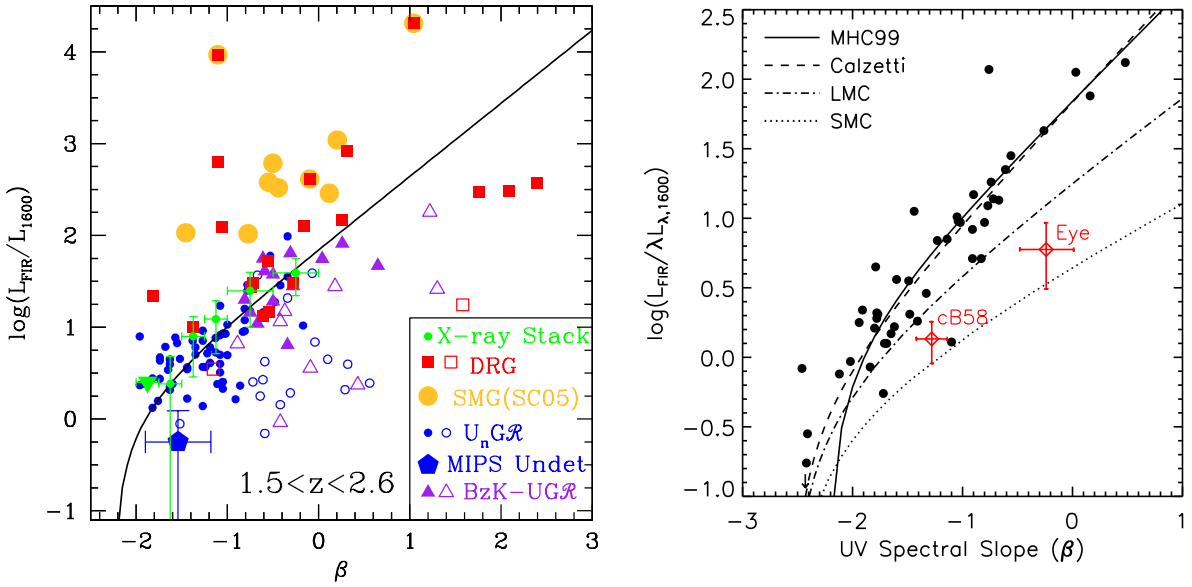

Figure 13: Dust Extinction in High-redshift Galaxies. **Left:** (From Reddy et al. 2006) Dust absorption, parameterized by F_{FIR}/F_{1600} vs. rest-frame UV spectral slope, β, for galaxies at $1.5 < z < 2.6$. Filled and open symbols, respectively, indicate galaxies with inferred stellar population ages of > 100 and < 100 Myr, for UV-selected galaxies (blue), BzK galaxies (purple), and DRGs (red). Filled yellow circles indicate SMGs. The large blue pentagon shows the results for UV-selected galaxies undetected at 24μm, using 24μm stacking results. The green filled circles represent the results from X-ray stacking analysis. The solid line indicates the Meurer, Heckman & Calzetti (1999) relation found for local UV-selected starburst galaxies. **Right:** (From Siana et al. 2009) Similar quantities, but for local starbursts (filled black circles), and two $z \sim 3$ gravitationally-lensed objects, cB58 and The Cosmic Eye (empty red diamonds). Also shown are the Meurer, Heckman & Calzetti (1999) relation (solid curve), and the predicted relation between $L_{FIR}/\lambda L_{\lambda,1600}$ and β for different reddening curves (Calzetti, LMC, and SMC).

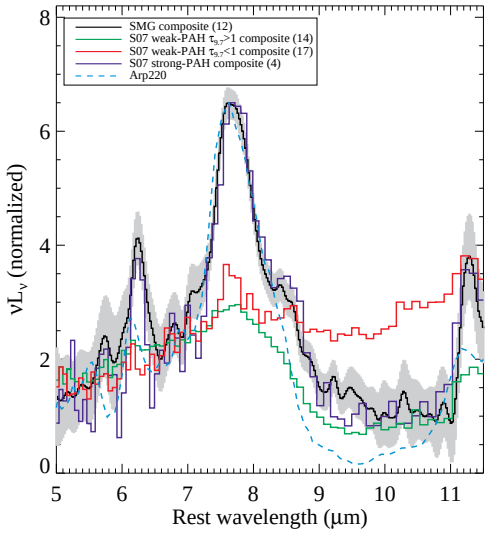

Figure 14: (From Pope et al. 2008) Mid-IR Spectrum of ULIRGs at high redshift. The composite *Spitzer*/IRS spectrum of 12 SMGs from Pope et al. (2008) is shown as the solid black line. The purple, red, and green solid histograms are composites from the sample of *Spitzer* 24μm-selected ULIRGs from Sajina et al. (2007), with purple indicating the composite of 4 strong-PAH sources, green indicating the composite of 14 weak-PAH, power-law-dominated sources with significant 9.7-μm silicate absorption ($\tau_{9.7} > 1$), and red indicating the composite of 17 weak-PAH, power-law-dominated sources with weaker 9.7-μm silicate absorption ($\tau_{9.7} < 1$). The light-blue dashed curve is the mid-IR spectrum of the local ULIRG, Arp 220. All curves have been normalized at $\sim 7\mu$m. The numbers in the legend indicate the number of sources in each composite spectrum. The prominence of PAH emission in the SMG composite indicates that star formation is the main energy source powering the mid-IR spectrum. On the other hand, the 24μm-selected ULIRGs indicate a range of spectral types, the majority of which appear to be dominated by AGN emission.

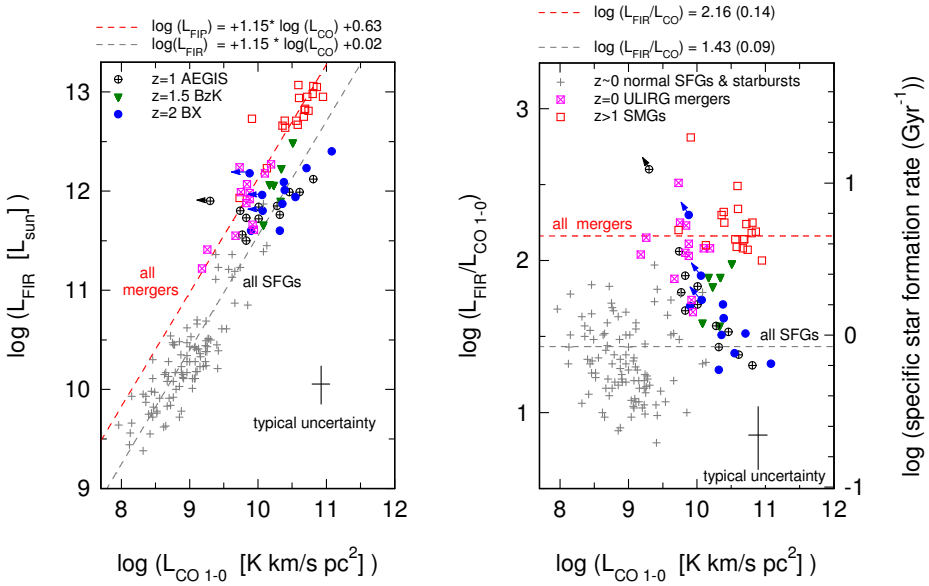

Figure 15: (Adapted from Genzel et al. 2010) Relationship between FIR luminosity and CO(1-0) luminosity in star-forming galaxies at low and high redshift. Gray crosses indicate isolated star-forming galaxies at $z \sim 0$. Magenta crossed squares are merging ULIRG galaxies at $z \sim 0$. Black crossed circles are $z \sim 1$ star-forming galaxies from the AEGIS field (Davis et al. 2007). Filled blue circles are $z \sim 2$ UV-selected "BX" galaxies (Steidel et al. 2004). Filled green triangles are $z \sim 1.5$ BzK galaxies (Daddi et al. 2010). Red empty squares are $z \sim 1-3.5$ SMGs (SMG references in Genzel et al. 2010). In cases where upper-J CO transitions were observed (i.e., most $z \geq 1$ systems), empirically-calibrated correction factors were applied to infer the CO(1-0) luminosity plotted on the horizontal axis. **Left:** L_{FIR} plotted vs. $L_{CO,1-0}$. Dashed gray and red lines indicate, respectively, the fits to the data for non-mergers (i.e. isolated star-forming galaxies at $z \sim 0$, $z \sim 1$ star-forming galaxies, and UV-selected and BzK galaxies at higher redshift) and mergers (i.e. $z \sim 0$ merging and interacting galaxies, and SMGs at higher redshift). **Right:** $L_{FIR}/L_{CO,1-0}$ vs. $L_{CO,1-0}$. The left-hand vertical axis, $L_{FIR}/L_{CO,1-0}$, can be re-expressed in terms of the specific star-formation rate (in units of Gyr^{-1}), shown as the right-hand vertical axis.

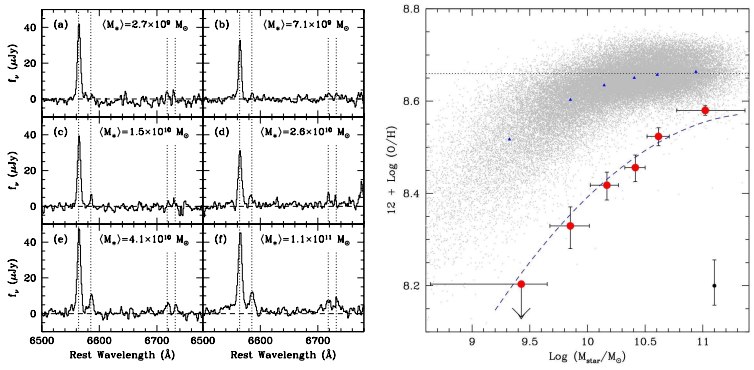

Figure 16: (From Erb et al. 2006a) The $M_{star} - Z$ relation at $z \sim 2$. **Left:** Relationship between [NII]/Hα and stellar mass. Shown here are composite Keck/NIRSPEC spectra of the Hα and [NII] region for the 87 galaxies in the sample of Erb et al. (2006a), grouped into six roughly equal bins of increasing stellar mass. In each panel, the mean stellar mass in the bin is indicated, and the Hα, [NII], and [SII] lines are marked by dotted lines (left to right, respectively). As stellar mass increases, the ratio between [NII] and Hα increases as well. **Right:** The corresponding relationship between 12+log(O/H) and stellar mass, based on the empirical trend shown in the left-hand panel. Large gray circles represent the averages in each $z \sim 2$ stellar mass bin, with metallicity estimated from the observed [NII]/Hα using the $N2$ calibration of Pettini & Pagel (2004). Vertical error bars show the uncertainty in the [NII]/Hα ratio, while the additional error bar in the lower right corner shows the additional uncertainty in the $N2$ calibration itself. The dashed line is the best-fit mass-metallicity relation of Tremonti et al. (2004), shifted downwards by 0.56 dex. In order to compare with the metallicities of $\sim 53,000$ SDSS galaxies in Tremonti et al. (2004), the $N2$ calibration was applied to the low-redshift sample, shown as small gray dots. The filled triangles indicate the mean metallicity of the SDSS galaxies in the same mass bins used for the $z \sim 2$ sample. While the SDSS sample clearly shows the saturation of the $N2$ indicator, the more reliable, lower-metallicity bins indicate that $z \sim 2$ galaxies are ~ 0.3 dex lower in metalllicity at a given stellar mass.

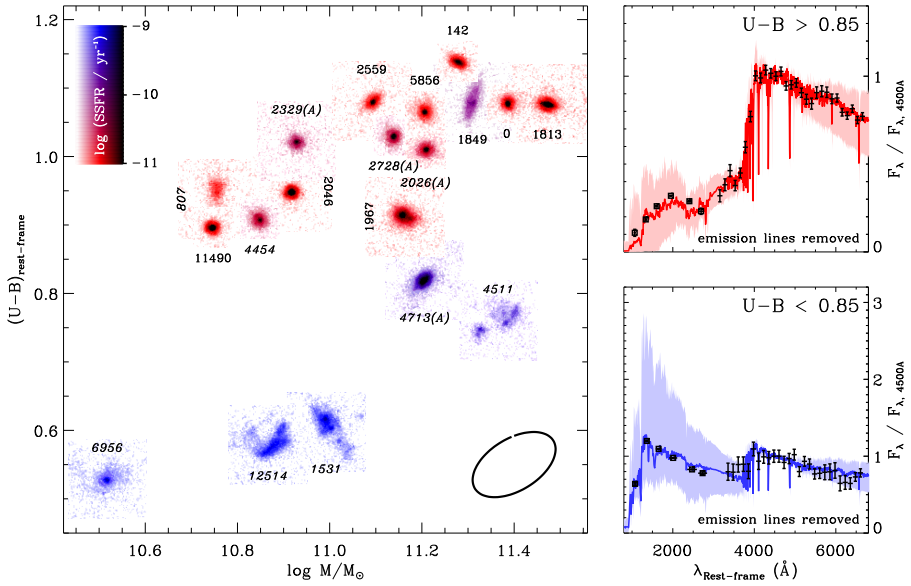

Figure 17: (From Kriek et al. 2009) Morphologies and SEDs of massive galaxies. **Left:** $U - B$ color vs. stellar mass, for a massive galaxy sample at $z \sim 2.3$ from Kriek et al. (2009) with rest-frame optical spectroscopy. The actual NIC2 image of each galaxy is used as a symbol, in order to indicate the trends between morphology and stellar population parameters. Color coding reflects the specific star-formation rate of the galaxies. Emission-line galaxies are indicated with italic ID numbers, and AGNs are indicated additionally with "(A)." Large, irregular galaxies reside mainly in the "blue cloud", while compact, quiescent galaxies lie on a red sequence. The ellipse represents the average 1σ confidence interval. **Right:** Stacked SEDs for blue (bottom panel) and red (top panel) galaxies in the $2 \leq z \leq 3$ spectroscopic sample of Kriek et al. (2008b), based on rest-frame UV photometry and rest-frame optical spectra.

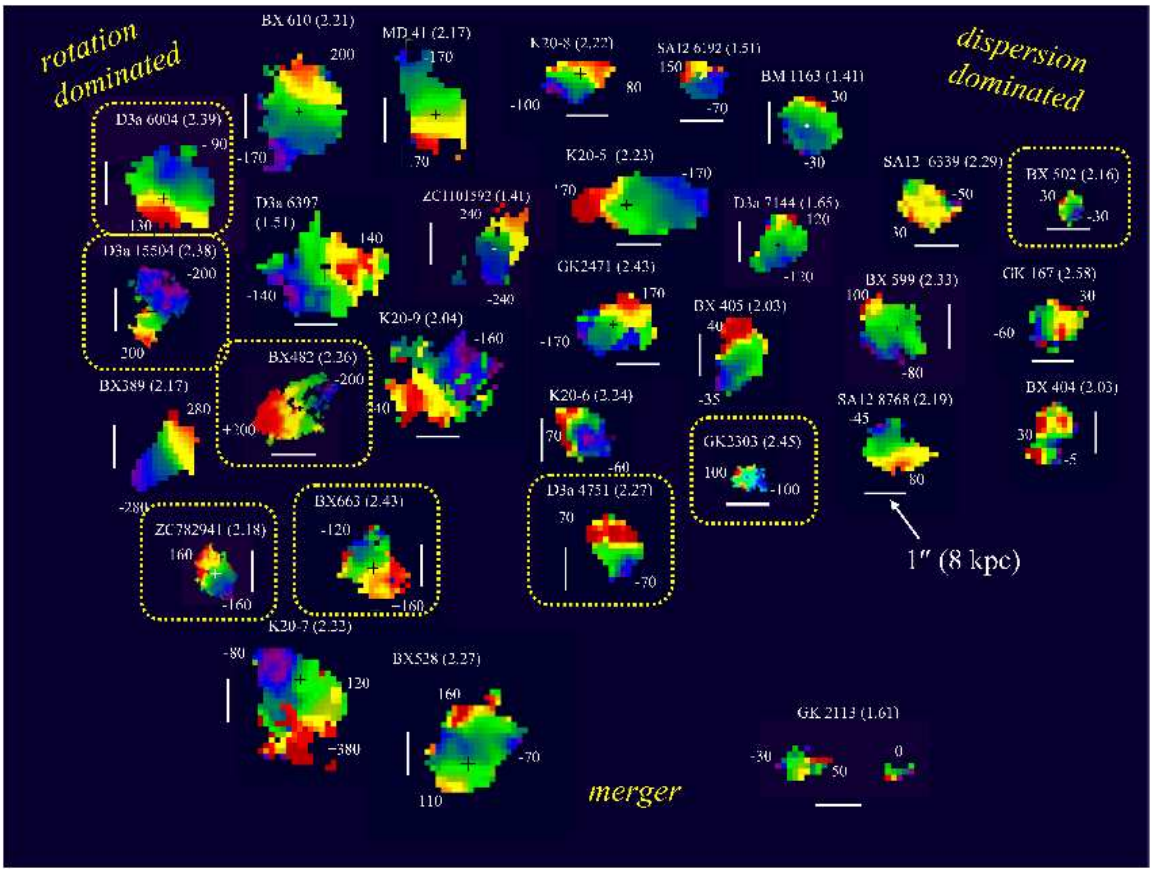

Figure 18: (From Förster Schreiber et al. 2009) Velocity fields from the SINS Hα sample, obtained using SINFONI on the VLT. Shown here are velocity fields for 30 of the 62 galaxies in the SINS Hα survey. Color coding is such that blue to red colors correspond to the range of blueshifted to redshifted line emission with respect to the systemic velocity. The minimum and maximum relative velocities are labeled for each galaxy (in km s^{-1}). All sources are shown on the same angular scale. The white bars correspond to 1", or ~ 8 kpc at $z = 2$. The galaxies are approximately sorted from left to right according to whether their kinematics are rotation-dominated or dispersion-dominated, and from top to bottom according to whether they are disk-like or merger-like as quantified by kinemetry analysis (Shapiro et al. 2009). Galaxies observed with AO are indicated by the yellow dashed lines.

Acronyms/Definitions

1. LBG: "Lyman Break Galaxy." Star-forming $z \geq 3$ galaxy selected on the basis of its rest-frame UV colors, which are indicative of a Lyman Break – i.e. significant absorption at wavelengths below 912 Å.

2. UV selection: More general use of rest-frame UV photometry to select star-forming galaxies not only at $z \geq 3$ using the Lyman Break, but also at $1.4 \leq z \leq 2.5$ using different rest-frame UV color criteria.

3. DRG: "Distant Red Galaxy." Galaxy selected on the basis of a red observed-frame $J - K$ color, which corresponds to a Balmer or 4000 Å break, or significant dust extinction, for objects at $z \sim 2 - 4$. The majority of DRGs are actively forming stars, but typically with higher M/L and stellar masses than UV-selected galaxies and sBzK galaxies.

4. sBzK: "Star-forming BzK Galaxy." Galaxy selected on the basis of its $B - z$ and $z - K$ colors to lie at $1.4 \leq z \leq 2.5$ and be actively star-forming. The sBzK criteria are tuned to find galaxies with Balmer breaks, ongoing star formation, and a wide range of dust extinction properties.

5. pBzK: "Passive BzK Galaxy." Galaxy selected on the basis of its $B - z$ and $z - K$ colors to lie at $1.4 \leq z \leq 2.5$ and be devoid of star formation. The pBzK criteria are tuned to find galaxies with prominent 4000 Å breaks and a lack of current star formation.

6. SMG: "Submillimeter Galaxy." Galaxy selected on the basis of its powerful luminosity in the submillimeter range of the spectrum. SCUBA 850 μm selection has commonly been used to find such systems. The prolific IR luminosity is due to reprocessed emission from dust (powered either by

stars, an active nucleus, or both).

7. LAE: "Lyα Emitter." Galaxy selected on the basis of having strong emission in the Lyα feature at rest-frame 1216 Å. As a result of the selection based on line strength, LAEs tend to be significantly fainter in the rest-frame UV continuum than other star-forming sources at the same redshift.

8. LIRG: "Luminous Infrared Galaxy." Galaxy characterized by $10^{11} L_{\odot} < L_{IR} \leq 10^{12} L_{\odot}$. Such systems, along with ULIRGs, are much more common at $z \sim 2$ than in the local Universe.

9. ULIRG: "Ultra-luminous Infrared Galaxy." Galaxy characterized by $L_{IR} > 10^{12} L_{\odot}$. Such systems, along with LIRGs, are much more common at $z \sim 2$ than in the local Universe.